PARTICLE VELOCITIES IN CONCENTRATED SUSPENSIONS UNDERGOING SHEAR

Bir Kapoor and Andreas Acrivos
The Levich Institute
City College of CUNY
140th Street & Convent Avenue
New York, New York 10031

ABSTRACT

A theory is described for modeling the flow of concentrated suspensions. This theory has been successfully tested by measuring the particle velocities in such suspensions flowing under gravity along an inclined plate.

INTRODUCTION

Consider the flow of a concentrated sediment which forms along an inclined plate underneath a monodisperse suspension of spherical particles of radius a which sediment under the action of gravity. Such a flow has important implications in the efficient operation of supersettlers, i.e. settling tanks with inclined walls, where the production of clear fluid is much larger than if the walls were vertical [1]. A schematic of such a supersettler is shown in Fig. 1.

This problem was studied theoretically by Nir and Acrivos [2] who modeled the sediment as an effective continuum Newtonian fluid with concentration dependent physical properties. But whereas in the earlier analysis [2] it was assumed that the downward flux of particles due to gravity was counter balanced by a shear-induced particle flux due only to gradients in the particle concentration, the theory has now been extended to include shear-induced particle diffusion due to gradients in the shear stress as well as the effects of a slip velocity along the surface of the plate.

In addition, a series of experiments were performed to test the theoretical predictions.

THEORY

Since under ordinary conditions, the concentrated sediment is very thin and the flow is laminar, the basic equations of continuity of momentum and of particle flux reduce, in the conventional lubrication approximation, to [2]:

149

$$\rho(\phi)\left\{u\frac{\partial u}{\partial x} + v\frac{\partial u}{\partial y}\right\} = g(\phi - \phi_s)\Delta\rho\sin\theta + \frac{\partial}{\partial y}\left[\mu(\phi)\frac{\partial u}{\partial y}\right] \tag{1}$$

$$\frac{\partial u}{\partial x} + \frac{\partial v}{\partial y} = 0 \tag{2}$$

$$u\frac{\partial\phi}{\partial x} + v\frac{\partial\phi}{\partial y} - \frac{\partial}{\partial y}\{\phi f(\phi)u_t\cos\theta\}$$

$$= a^2\frac{\partial}{\partial y}\left\{\beta(\phi)\frac{\partial u}{\partial y}\frac{\partial\phi}{\partial y} + \frac{\alpha(\phi)}{\mu(\phi)}\left[\frac{\partial}{\partial y}\mu(\phi)\frac{\partial u}{\partial y}\right]\right\} \tag{3}$$

where, as shown in Fig. 2, x and y are the longitudinal and transverse coordinates, u and v are the corresponding bulk velocity components, $\rho(\phi)$ is the bulk density, $\mu(\phi)$ the effective viscosity, ϕ the local particle concentration, ϕ_s the particle concentration in the ambient suspension, $\Delta\rho$ the difference between the particle density and that of the fluid, u_t the Stokes settling velocity of an isolated sphere, $f(\phi)$ the hindrance function, a the particle radius, and $\beta(\phi)$ and $\alpha(\phi)$ the dimensionless coefficients of shear-induced diffusion due respectively, to gradients in the particle concentration and in the shear stress [3]. Here, the particle Reynolds number has been taken to be vanishingly small. In addition, the inertia term in the momentum equation is generally negligible relative to the buoyancy and viscous forces [2], hence eq. (1) reduces to:

$$\frac{\partial}{\partial y}\left[\mu(\phi)\frac{\partial u}{\partial y}\right] + g(\phi - \phi_s)\Delta\rho\sin\theta = 0 \tag{4}$$

The appropriate boundary conditions are that, at $y = 0$, i.e. along the surface of the plate:

$$a^2\left\{\beta(\phi)\frac{\partial u}{\partial y}\frac{\partial\phi}{\partial y} + \frac{\alpha(\phi)}{\mu(\phi)}\frac{\partial}{\partial y}(\mu(\phi)\frac{\partial u}{\partial y})\right\} + \phi f(\phi)u_t\cos\theta = 0 \tag{5}$$

which refers to the zero particle flux condition into the plate, together with the requirement that $v = 0$ and the slip condition

$$u = a\zeta(\phi)\frac{\partial u}{\partial y} \qquad at \ y = 0 \tag{6}$$

where $\zeta(\phi)$ is the slip coefficient evaluable at ϕ_0, the a priori unknown particle concentration at the wall.

The conditions along $y = \delta$, the interface between the concentrated sediment and the ambient suspension are that, [2], $\partial u/\partial y = 0$ and that the particle concentration suffers a jump from ϕ_s to ϕ_δ according to:

$$\left[\left(-u\frac{d\delta}{dx}+v\right)\phi-\phi f(\phi)u_t\cos\theta+a^2\frac{\alpha(\phi)}{\mu(\phi)}g(\phi-\phi_s)\Delta\rho\sin\theta\right]_{y=\delta,\phi=\phi_s}$$

$$=\left[-u\frac{d\delta}{dx}+v-f(\phi_s)u_t\cos\theta\right]_{y=\delta}\phi_s \qquad (7)$$

Finally we require that ϕ should remain regular as $y\to\delta(x)$ from below, or, more generally, that

$$\lim_{y\to\delta}\left(\frac{\partial u}{\partial y}\frac{\partial^2\phi}{\partial y^2}\right)=0 \qquad (8)$$

It is easy to show that, given the effective properties $\mu(\phi),f(\phi),\alpha(\phi),\beta(\phi)$ and $\zeta(\phi)$, the system of equations (2) − (4) subject to the boundary conditions (5) − (8) contains only two dimensionless parameters, specifically ϕ_s and θ, the values of which completely determine the flow phenomenon in question, at least according to the present model.

If the slip velocity is set equal to zero, i.e. for $\zeta(\phi)=0$, the above system admits a similarity solution [2] in which $\delta=\delta_0(\phi_s,\theta)a^{2/3}x^{1/3}$. On the other hand, in the presence of slip, similarity ceases to apply except near the leading edge, $x\to0$, where δ is found to be proportional to $x^{1/2}$. In the general case, the partial differential equations must be solved numerically.

Such numerical solutions were constructed [4] for the following choice of effective parameters:

$$\alpha(\phi)=0.6\phi^2$$

$$\beta(\phi)=\frac{1}{3}\phi^2\left[1+\frac{1}{2}exp(9\phi)\right]$$

$$\mu(\phi)=\mu(o)\lceil1+\frac{1.5\phi}{1-(\phi/\phi_m)}\rceil^2 \quad with \quad \phi_m=0.58$$

$$f(\phi)=\frac{1-\phi}{\mu(\phi)}\mu(0)$$

$$\zeta(\phi)=\frac{1}{6}\frac{\mu(\phi)}{\mu(0)}$$

The expressions for α,β,μ and f are identical to those used previously [3,5,6] while $\zeta(\phi)$ was obtained by adapting an effective medium theory [7] together with experimental determination [4] of the numerical coefficient $\frac{1}{6}$.

EXPERIMENTS

The experiments were performed in a continuously operated inclined set-tler shown schematically in Fig. 3. The particles were Diakon CA603 spheres, of mean diameter $90\mu m$, and the fluid consisted of a mixture of turpentine

151

(63% by volume) and tetraline (37% by volume) the refractive index of which almost perfectly matched that of the particles.

The local thickness of the sediment layer, $\delta(x)$, was easy to measure experimentally by means of a cathetometer or by employing a video imaging technique. On the other hand, the determination of the particle velocity profile presented a much more difficult undertaking which was eventually overcome through the use of a Dantec Laser Doppler Anemometer. The details of the experimental set-up and of the measuring techniques are available elsewhere [4].

## COMPARISON OF THEORY AND EXPERIMENTS

Shown in Figs. 4 and 5 are typical profiles for the sediment thickness $\delta(x)$ and of the particle velocity within the flowing sediment. In view of the fact that the theoretical predictions did not entail the use of any adjustable parameters, the agreement between theory and experiment should be viewed as excellent.

ACKNOWLEDGEMENT

REFERENCES

1. Acrivos, A. and Herbolzheimer, E. "Enhanced Sedimentation in Settling Tanks with Inclined Walls", J. Fluid Mech. 91, 401 (1979).

2. Nir, A. and Acrivos, A. "Sedimentation and Sediment Flow on Inclined Surfaces", J. Fluid Mech. 212, 139 (1990).

3. Leighton, D. and Acrivos, A. "The Shear-Induced Migration of Particles in Concentrated Suspensions", J. Fluid Mech. 181, 415 (1987).

4. Kapoor, Bir, Ph.D. Dissertation, City College of the City University of New York, 1993 (in preparation).

5. Leighton, D.T. and Acrivos, A. "Viscous Resuspension", Chem. Eng. Sci. 41, 1377 (1986).

6. Schaflinger, U., Acrivos, A. and Zhang, K. "Viscous Resuspension of a Sediment Within a Laminar and Stratified Flow", Int. J. Multiphase Flow 67, 6088 (1990).

7. Acrivos, A. and Chang, E. "A Model for Estimating Transport Quantities in Two-Phase Materials", Phys. Fluids 29, 3 (1986).
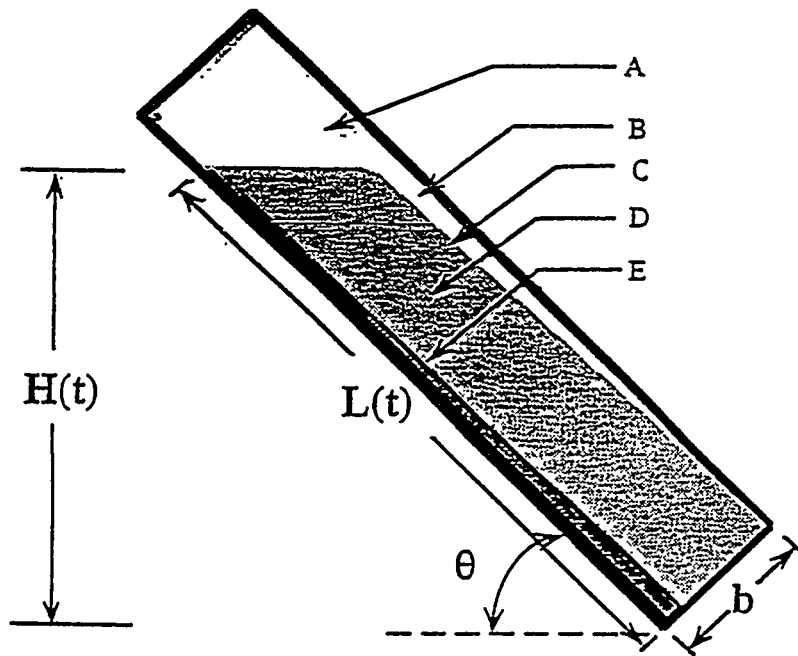
A: Clear fluid reservoir

B: Clear fluid layer

C: Suspension-clear fluid interface

D: Suspension

E: Sediment layer

Figure 1   A sketch of an inclined settler.
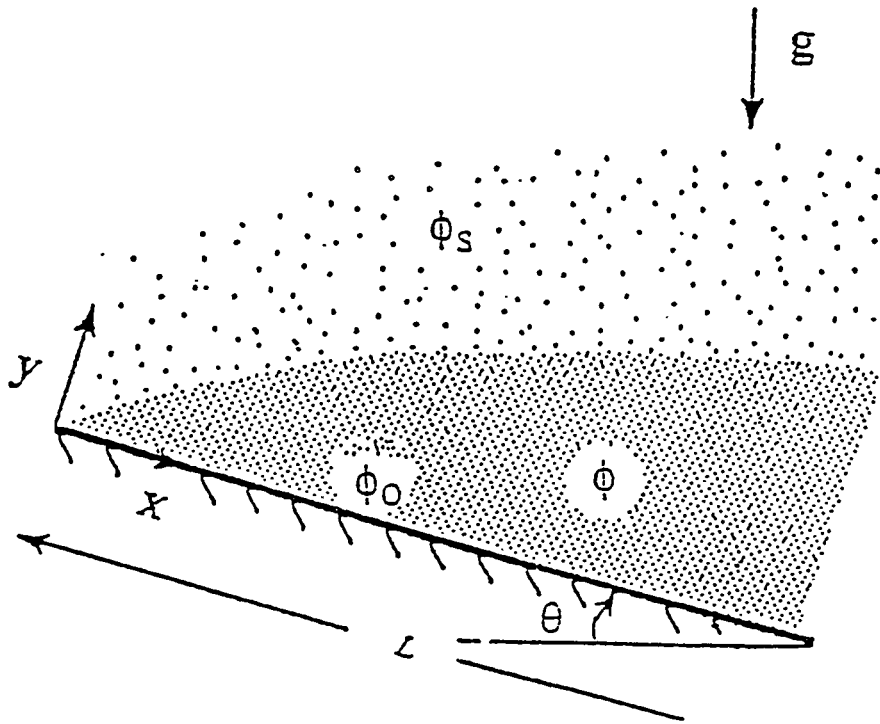
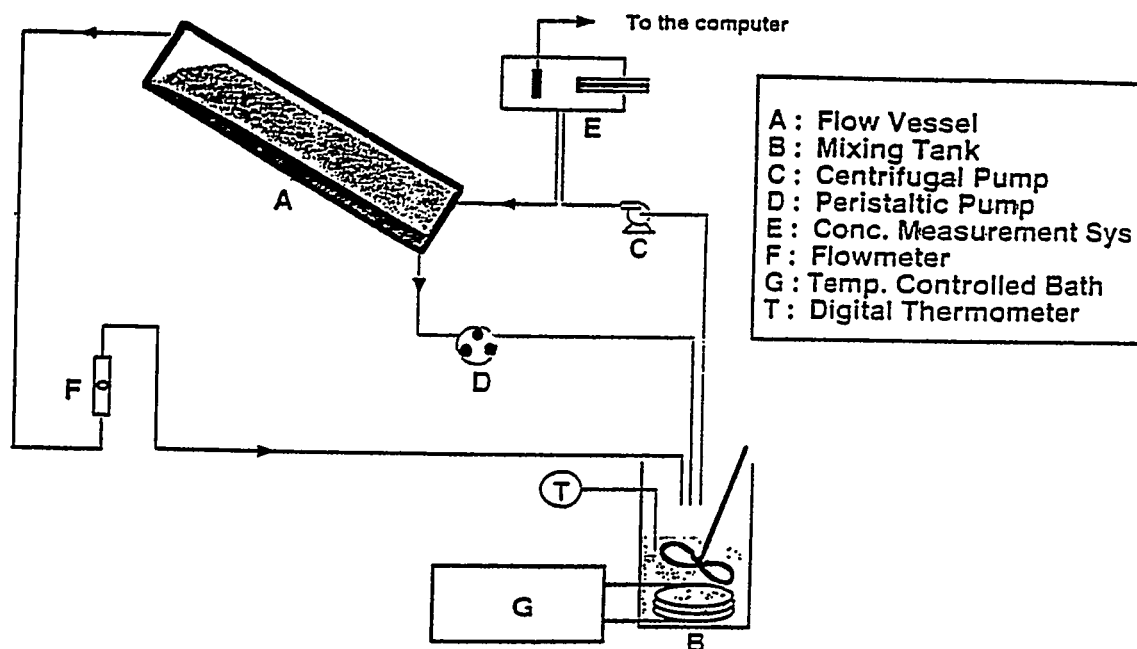Figure 2   Sketch of the sediment flow on an inclined plate.

To the computer

A : Flow Vessel
B : Mixing Tank
C : Centrifugal Pump
D : Peristaltic Pump
E : Conc. Measurement Sys
F : Flowmeter
G : Temp. Controlled Bath
T : Digital Thermometer
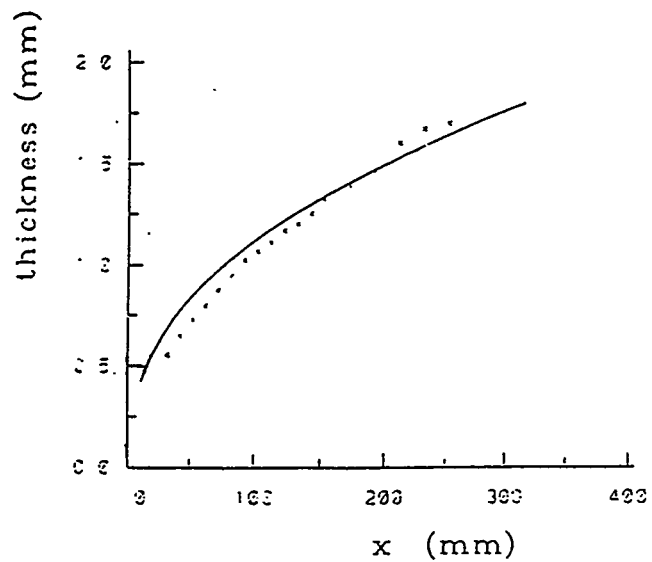
Figure 3   Sketch of the experimental setup [4].

Figure 4   Sediment layer thickness profile for $\phi_S = 6.5\%$,
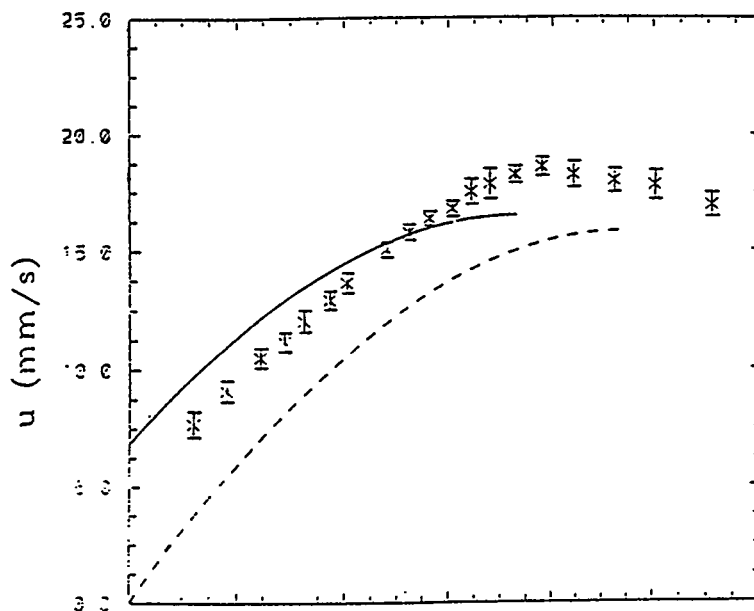$\theta = 35^o$ and a = 0.045 mm - theory; x-experimental
points.

Figure 5   Velocity profile within the sediment layer at
x = 324 mm and for $\phi_S = 6.5\%$ and $\theta = 35^o$ - theory
with partial slip; — theory with no slip; I -experi-
mental points.

Coupling Effects in Multiphase Free Shear Flows

T.R. Troutt, C.T. Crowe, and J.N. Chung
Washington State University

ABSTRACT

The primary goal of this research program is to examine the effects of two-way multiphase coupling on the development of organized vortex structures in free shear flows and the resultant multiphase dispersion. Previous research studies have determined that one-way coupled particle dispersion in free shear flows is strongly dependent on the vortex structures present in these flows and their interactions as well as the ratio of the particle aerodynamic response time to the time scale of the dominant vortex structures. Current research efforts are directed towards exploring the effects that two-way momentum, mass and energy coupling have on the multiphase dispersion processes previously uncovered. These efforts involve analytical, numerical and experimental investigations. Recent analytical and numerical results indicate that momentum coupling effects can significantly alter the global stability and potentially the large scale features of the multiphase flow field. These multiphase coupling effects may have significant importance with regard to predicting the performance of many energy conversion systems.

INTRODUCTION

Multiphase mixing in turbulent flows is a key element in many practical energy conversion, chemical mixing and pollutant dispersal problems. Numerous important technological and environmental processes could be better addressed with improvements in understanding in this area. Progress in developing understanding of this field, however, has traditionally been difficult because of the complexities involved with the turbulent flows employed to provide the mixing mechanisms. To address this problem from a new perspective several years ago this research group initiated an ongoing investigation concerning the potential connections between organized turbulent vortex structures and the particle dispersion process.

Organized vortex structures in single phase free shear flows have been studied extensively in the recent past Ho and Huerre[1] because of their apparent importance in the global flow development. However, the relationship between organized vortex structures and the particle dispersion process was largely unknown. A simple physical concept which identified the Stokes number, a time scale ratio between the particle aerodynamic response time and the characteristic organized vortex motion time, as a controlling parameter for the particulate dispersion process was used to initially guide this new approach Crowe, Gore and Troutt[2], Chung and Troutt[3], Crowe, Chung and Troutt[4]. The Stokes number can in fact be shown to be the controlling parameter in the particle motion equation for situations where the particle material density is much greater than the local fluid density and the particle Reynolds number is small Chung and Troutt[3].

To emphasize the role organized vortex motions play in the particle dispersion process this research program has focused on free shear flows such as mixing layers, jets and wakes since the organized vortex structures in these single phase flows are probably the most clearly characterized and understood Ho and Huerre[1]. Although these flows do exhibit instantaneous, three dimensional, small scale structures, their primary global development is closely tied to the large scale, quasi two-dimensional structures Browand and Troutt[5].

The overall results from these analytical, experimental and numerical research efforts concerning particle dispersion in free shear flows have yielded several interesting insights into the dispersion process and its connection to the organized vortex development. These findings can be summarized as follows:

a) The qualitative and quantitative character of the particle dispersion patterns in mixing layers, jets and wakes are strongly dependent on Stokes number and can be instantaneously highly anisotropic and nonhomogeneous Crow, Chung and Troutt[4]; Chung and Troutt[3]; Tang et al.[7].

b) For mixing layers a stretching and folding operation associated with vortex structure development and pairing appears to be a dominant intermediate Stokes number particle dispersion mechanism Wen[8].

c) For wakes where vortex pairings rarely occur, the dispersion process focuses intermediate Stokes numbers particles into extremely thin sheet-like regions near the boundaries of the vortex structures Tang[7].

The previous results have addressed primarily flows for which the effects of the particles on the flow were neglected, one-way coupling. Of considerable scientific and technological interest is the more complex situation where two-way coupling effects between the particles and the flow exist. This situation has been initially addressed quite recently by our group using stability analysis involving momentum two-way coupling effects Yang et al.[9], and Yang et al.[10]. The present research program addresses the two-way coupling situation involving mass, momentum and energy coupling between the flow and particles or droplets. This type of coupling is of high technological interest and has the potential for greatly affecting the resultant flows.

Analytic Procedure for Implementing Coupling Effects

One objective of the present research is to extend the existing modeling effort to include compressibility effects and energy coupling. This development can be viewed as a logical precursor to including heat release due to chemical reaction and the analysis of multiphase combustion in large scale turbulent structures. The technique is an extension of that reported by Ghoniem et al.[11] for compressible reacting flows using the discrete vortex method together with transport elements.

The velocity field in the model is decomposed into three parts; the field corresponding to the basic potential flow, the velocity induced by the vortices in the field and the field produced by the mass release from the droplets. Including compressibility effects leads to a change in the strength of the mass sources and also affects the circulation of the discrete vortices.

The continuity equation for the gas phase of a droplet-laden flow with void fraction near unity is

$$\nabla \cdot \vec{u} = \frac{S_m}{\rho} - \frac{1}{\rho}\frac{D_\rho}{Dt}$$

where S_m is the mass source per unit volume due to droplet evaporation or condensation. For low Mach numbers, one can make the assumption that the pressure level is constant so, for an ideal gas, the continuity equation becomes

158

continuity equation becomes

$$\nabla \cdot \vec{u} = \frac{S_m}{\rho} + \frac{1}{T}\frac{DT}{Dt}$$

where T is the local temperature. The right side of this equation represents the strength of the mass source term associated with each droplet. The last term represents the local expansion of the flow due to local heating or cooling.

The momentum equation for the gas phase of a dispersed phase flow at high Reynolds number and void fraction near unity is

$$\frac{D\vec{u}}{Dt} = \frac{-1}{\rho}\nabla p + \frac{1}{\rho}[(\frac{f\rho'_d}{\tau_A} + S_m)(\vec{v} - \vec{u})]$$

where f is the ratio of the drag coefficient to Stokes drag, τ_A is the aerodynamic response time of the droplet, ρ'_d is the bulk density of the droplets and $\vec{v}$ is the velocity of the droplet phase. It is assumed that the viscosity is important only in the immediate neighborhood of the droplets. The last term in the above equation is due to momentum coupling and is calculated from the droplet trajectories. For convenience this term is simplified to $\vec{C}$ so the equation can be rewritten more simply as

$$\frac{D\vec{u}}{Dt} = -\frac{1}{\rho}\nabla p + \frac{1}{\rho}\vec{C}$$

Taking the curl of the momentum equation and limiting the solution to two-dimensional flows yields

$$\frac{D\vec{\omega}}{Dt} - \frac{\vec{\omega}}{\rho}\frac{D\rho}{Dt} = \frac{1}{\rho}\nabla\rho \times \left(\frac{\nabla p}{\rho} - \frac{\vec{C}}{\rho}\right) + \frac{1}{\rho}\nabla \times \vec{C}$$

In the discrete vortex approach the flow field is subdivided into material elements with circulation Γ. Since the mass of a material element is constant, the derivative of the density can be related to the area change of the element (in planar flow) by

$$\frac{1}{\rho}\frac{D\rho}{Dt} = -\frac{1}{A}\frac{DA}{Dt}$$

Substituting this expression into the vorticity equation and using the momentum equation leads to

$$\frac{D(\omega A)}{Dt} = -\frac{A}{\rho}\nabla\rho \times \frac{D\vec{u}}{Dt} + \frac{A}{\rho}\nabla \times \vec{C}$$

The product of the vorticity and the area is the circulation of the vortex. If low Mach number is assumed the density variation is associated with the temperature change only and the expression for the change in circulation of each discrete vortex is

$$\frac{D\Gamma}{Dt} = \frac{(A\rho)_0}{\rho}\frac{\nabla T}{T} \times \frac{D\vec{u}}{Dt} + \frac{A}{\rho}\nabla \times \vec{C}$$

where $(A\rho)_0$ is the initial cross-sectional area times the density of the material element. This product, which is proportional to the mass of the element, remains constant. The first term on the right side is the effect of density change on the vortex strength and the last term is that due to multiphase coupling. The coupling term is to be evaluated in the same manner used previously for the mass and momentum coupling. That is, the droplet trajectories provide locations and properties of the droplets in the field. The

159

properties are area-averaged to nodal points on a grid and the coupling term is evaluated and distributed to each vortex in the cell. To calculate the change in circulation, the temperature and density fields are needed. These are obtained from the transport-element method introduced by Ghoniem et al.[11]

Numerical Results

Numerical simulation results for momentum coupling effects in a temporally developing free shear layer have been recently computed over a range of particle concentration levels. For base flow comparison purposes Figure 1 presents the time development of the flow structures for a one-way coupling situation.

The time evolution of the vortex structures in the free shear layer for a two-way momentum coupled situation at a particle mass concentration ratio of 0.3 is shown in Figure 2. Although the flow develops in a qualitative similar fashion the vortex pairing process shows little change and the lateral flow dispersion process is only slightly inhibited. At higher particle concentration levels the flow development is slowed significantly. A comparison between flow vortex structure development at similar times for the non-coupled and momentum coupled flow at a concentration level of 3.0 is shown in Figure 3.
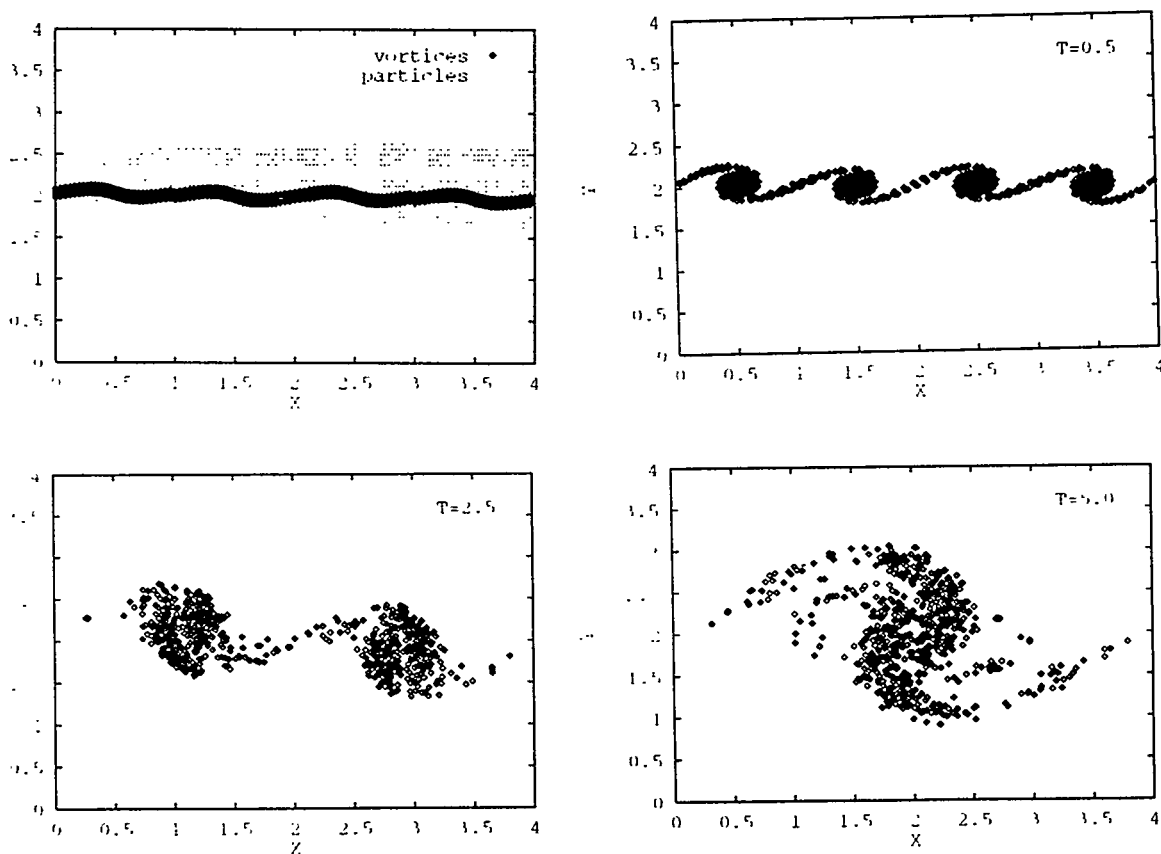

Figure 1. Time development of flow structures one-way coupling

A quantitative evaluation of the effect of momentum coupling on rate of growth of the free shear layer is presented in Figure 4. This figure compares the momentum thickness of the shear layer as a function of time for three different particle concentration levels. The significant change in the development of the free shear layer at the high concentration level is quite apparent.
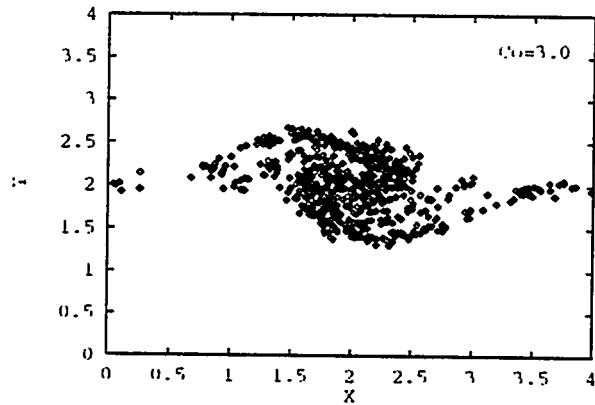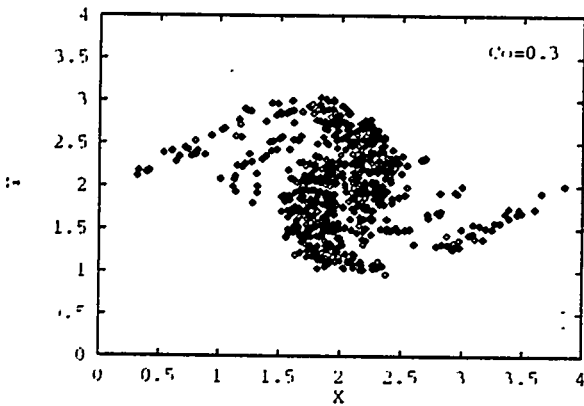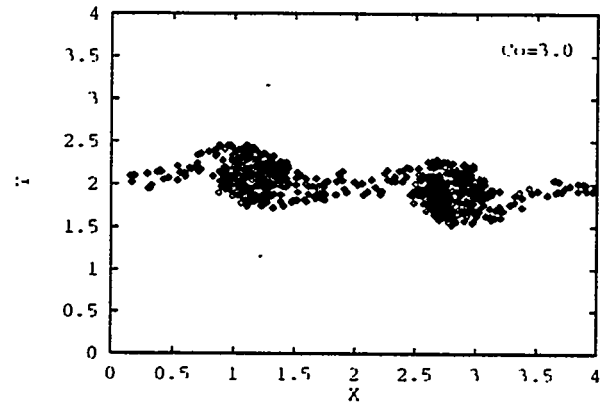
160
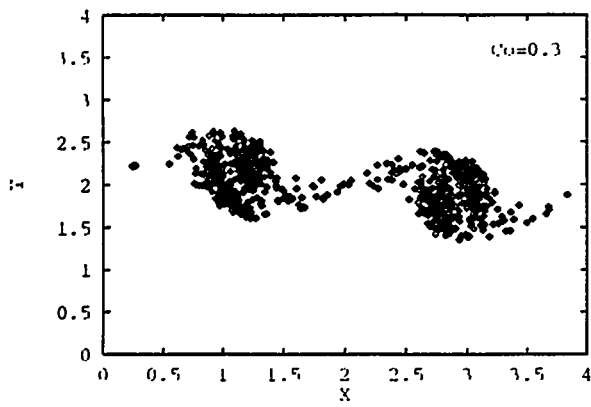
Figure 2. Time development of flow structures two-way momentum coupling, particle mass concentration = 0.3

Figure 3. Time development of flow structures two-way momentum coupling, particle mass concentration = 3.0

Figure 4. Development of momentum thickness for different mass particle concentration levels.

Experimental Research Program

Currently experiments concerning vaporizing droplet dispersion are being carried out in a recently installed heated wind tunnel. The flow configuration involves a heated two-dimensional plane wake into

161

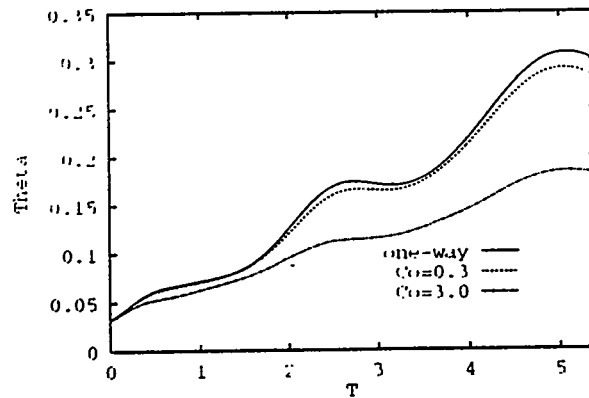which lower temperature liquid H_2O droplets are injected. the temperature of the air stream is adjustable between $T=100°C$ to $400°C$. the vaporizing droplets then release both mass and energy into the wake flow creating the potential for significant two-way coupling effects between the droplets and the wake flow.

Two major experimental techniques are being pursued in conjunction with this research. Global multiphase flow information will be obtained by employing laser light sheet visualization techniques with digital particle image position and velocity analysis. Local point multiphase flow information involving droplet size and velocity will be obtained using phase doppler anemometry techniques. Both of these major experimental techniques are presently being carried out in this laboratory.

Figure 5 displays the results from a laser light sheet visualization of solid particles in a plane wake flow. After acquisition the image is then digitized and the spherical particles identified through shape analysis. Instantaneous particle locations and velocities using multiple light pulse control, can then be determined from the results. The results for particle concentration contours and velocities obtained from the image are also shown. Similar techniques are now being pursued for vaporizing droplets in the heated plane wake environment.

a) particle dispersion pattern

b) particle concentration contours

c) particle velocity vectors

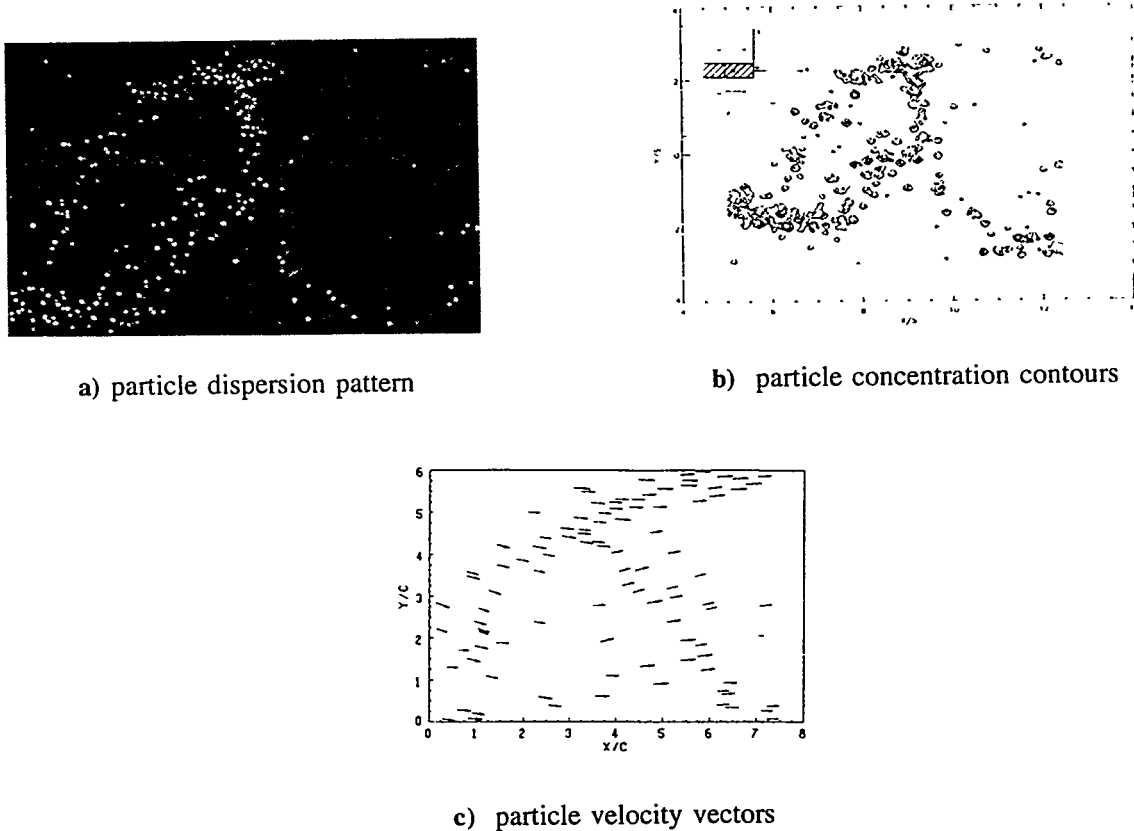**Figure 5.** Experimental results for particle dispersion in a plane wake flow St=O(1)

SUMMARY

An analytical, experimental and numerical investigation of the effects of two-way momentum, mass and energy coupling in multiphase free shear flows is underway. Stability results indicate that two-way momentum coupling effects decrease the amplification rate of disturbances in plane mixing layers and

162

change the instability mode from absolute to convective in plane wakes. The magnitude of these effects increase with particle concentration levels in a nearly linear fashion.

Numerical results for a temporally developing free shear layer demonstrate that two-way momentum coupling effects slow the development of vortex structures and their subsequent pairing interactions. This slowdown effect in the vortex interactions causes decreases in the momentum thickness development of the free shear layer.

Experimental efforts using laser visualization techniques and phase doppler velocity and droplet sizing techniques are presently evaluating two-way coupling effects for comparison to the numerical results.

ACKNOWLEDGEMENTS

REFERENCES

1. Ho, C.M. and Huerre, P., 1984. Perturbed Free Shear Layers, *Ann. Rev. Fluid Mech.*, **16**, 365-424.
2. Crowe, C.T., Gore, R.A. and Troutt, T.R., 1985, Particle Dispersion by Coherent Structures in Free Shear Flows, Particle Science and Technology, Vol. 3, pp. 149-158, 1985.
3. Chung, J.N. and Troutt, T.R., 1988, Simulation of Particle Dispersion in an Axisymmetric Jet, *J. Fluid Mech.*, **86**, 199.
4. Crowe, C.T., Chung, J.N. and Troutt, T.R., 1989, Dispersion in Turbulent Shear Flows, *Progress in Energy and Combustion Sci.*, **14**, 171.
5. Browand, F.K. and Troutt, T.R., 1985, The Turbulent Mixing Layer: Geometry of Large Vortices, *J. Fluid Mech.*,**158**, 487.
6. Crowe, C.T., Chung, J.N. and Troutt, T.R., Particle Dispersion by Organized Turbulent Structures, 1992, Chp 18, Particulate and Two-Phase Flow Edit. M.C. Roco Butterworth-Heinemann Series in Chemical Engineering.
7. Tang, L., Wen, F., Yang, Y., Crowe, C.T., Chung, J.N, and Troutt, T.R., 1992, Self-organizing particle Dispersion Mechanism in a Plane Wake," *Phys. Fluids A*, **4**, 10, 2244.
8. Wen, F., Kamalu, N., Chung, J.N., Crowe, C.T. and Troutt, T.R., 1992, "Particle Dispersion in Plane Mixing Layers," ASME, *J. of Fluids Engin.*, **114**, 657-666.
9. Yang, Y., Chung, J.N., Troutt, T.R. and Crowe, C.T., 1990, "The Influence of Particles on the Spatial Stability of Two-Phase Mixing Layers," *Phys. Fluids A*, **2**(10), 1839-1845.
10. Yang, Y., Chung, J.N., Troutt, T.R. and Crowe, C.T., 1993, "The Effects of Particles on the Stability of a Two-Phase Wake Flow, *Int. J. Multiphase Flow*," **19**, 1, 137-149.
11. Ghoniem, A.F., Heidarinejad, G. and Krishnan, A., 1987, Turbulence-Combustion Interactions in a Reacting Shear Layer, Paper AIAA-87-1718, 23rd AIAA/SAE/ASME/ASEE Joint Propulsion Meeting, La Jolla, CA.

WAVELENGTH SELECTION IN TRAVELING-WAVE CONVECTION IN A FLUID MIXTURE

C.M. Surko, K.D. Eaton, G.W. Baxter*, and K. Iwata

Department of Physics and Institute for Nonlinear Science
University of California, San Diego
La Jolla, California 92037

ABSTRACT

The mechanisms by which a one-dimensional pattern of traveling waves changes wavelength (i.e. the Eckhaus instability) is studied in a binary fluid mixture. Propagating wavelength modulations develop when the Rayleigh number of the system is decreased below a wavelength-dependent threshold, commonly referred to as the Eckhaus boundary. These wavelength modulations increase in amplitude and narrow in spatial extent until they trigger the creation or annihilation of convection roll pairs and thereby change the average wavelength of the system. We find qualitatively different dynamics for wavelength-increasing events and wavelength-decreasing events; these differences are due to the strong wavelength dependence of the group velocity.

INTRODUCTION

Nonequilibrium systems form an important part of our physical world. An important class of nonequilibrium systems is those in which traveling waves play a central role. The work discussed here has relevance to systems such as lasers, ocean waves, atmospheric flows, and certain kinds of crystal growth. A fundamental question in pattern selection and dynamics concerns the mechanism by which a periodic pattern changes wavelength in response to changes in control parameter. In the Eckhaus instability, a wavelength instability results when the control parameter is lowered below a wavelength-dependent threshold. The case in which the underlying pattern is stationary has received considerable experimental and theoretical attention [1,2,3]. In contrast, wavelength instabilities in pattern forming systems in which the underlying state consists of traveling waves have only recently been studied. The first experimental studies of the Eckhaus instability for traveling waves were done by Janiaud et al [4]. They studied wavelength instabilities on wave trains which resulted from the oscillatory instability in a convecting gas. While their results were interesting, experimental constraints limited their work to a small aspect-ratio system.

Furthermore, the fact that the wavelength modulation in their experiment is a tertiary instability made detailed theoretical analysis of their system difficult. Recently the Eckhaus instability for traveling waves has been investigated in the binary fluid system by both our group and by complementary experiments elsewhere [5,6].

Binary fluid mixtures of ethanol and water provide a model system in which to study nonequilibrium pattern-forming systems, since the underlying fluid equations are well understood and the control parameters of the system can be precisely controlled. The binary fluid system has been the subject of extensive study in recent years and consequently much is known about the nonequilibrium behavior of this system.

Binary fluid convection is closely related to convection in a pure fluid. In pure fluid convection, by heating from below, a temperature difference is imposed across a horizontal fluid layer, causing the fluid to expand and rise under the buoyant force. The Rayleigh number, R, is proportional to the imposed temperature difference and is the main control parameter in convection experiments. Due to the stabilizing effects of heat diffusion and viscosity, the onset of convection occurs only after a minimum temperature difference is imposed across the fluid layer at a critical Rayleigh number, R_c. (In this paper we use the reduced Rayleigh number $r \equiv R/R_c$.) In binary fluid mixtures, two additional parameters are required to describe the system. The Lewis number, $L \equiv D/k$, is the ratio of diffusivity of concentration to the thermal diffusivity and thus characterizes the relative time scales on which concentration and heat diffuse. The "separation ratio", Ψ, is a measure of the concentration-driven density changes due to the Soret effect which couples the temperature gradient to concentration gradients [7]. For $\Psi < 0$, the lighter component diffuses toward the colder region and a linear concentration gradient develops which stabilizes the fluid layer against convection. Consequently, the Rayleigh number at which the onset of convection occurs in the mixture is greater than that in a pure fluid with the same fluid properties.

When the Rayleigh number is increased above threshold, the linear concentration gradient is destroyed by the onset of convection; the fluid is well-mixed in the interior of the rolls and the concentration gradients occur only in boundary layers at the top and bottom of the fluid layer [8,9,10]. Concentration from these horizontal boundary layers is fed asymmetrically into the vertical upflow and downflow regions at the roll boundaries, producing a lateral modulation in concentration. In ethanol-water mixtures $L << 1$; and for $\Psi < 0$, the convection patterns are generally found to propagate laterally as traveling waves. It is the small phase shift between the lateral concentration and temperature fields which is predicted to cause the translation of the convection rolls.
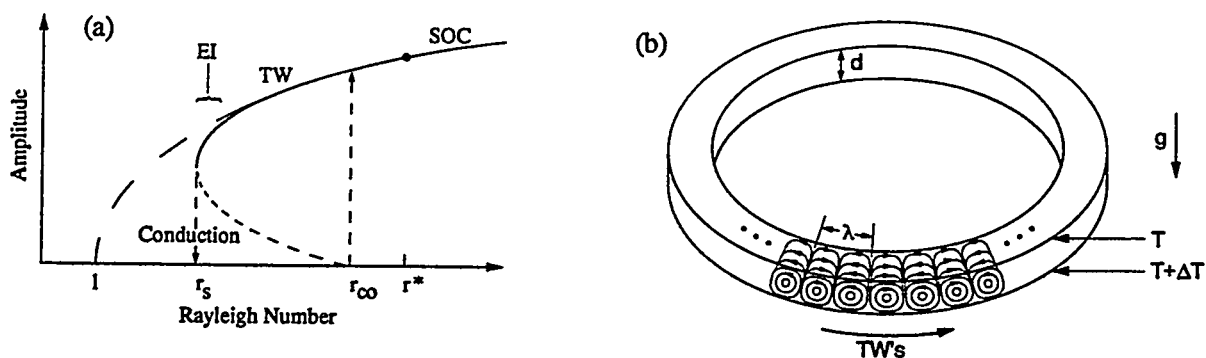
Figure 1. Shown in (a) is a schematic of the bifurcation diagram for pure and binary fluid convection: pure fluid (long dashed line), binary fluid mixture at $\Psi = -0.25$ (solid line), and unstable branch in the binary fluid (short dashed line). The bifurcation is supercritical in the pure fluid and subcritical in the mixture. The Eckhaus instability is encountered in the small range of Rayleigh numbers indicated as "EI". Shown in (b) is a schematic of the experimental geometry.

In this paper, we report results for a fluid mixture at $\Psi = -0.25$. The bifurcation diagram for this value of Ψ is shown schematically in Fig. 1(a). For this value of Ψ, the bifurcation is subcritical. Convection begins at $r = r_{co}$ as a Hopf bifurcation. The convective amplitude grows via a long transient to a state of slow-moving traveling waves (TW) with a period of approximately 1/30 the period of the Hopf bifurcation. As r is decreased, this nonlinear state remains stable until the Eckhaus instability (EI) is reached. The instability is encountered in a small region of Rayleigh numbers near the saddle-node bifurcation. If the initial wave number corresponds to the minimum of the Eckhaus boundary, the saddle-node bifurcation point is encountered at $r = r_s$, where the amplitude of the pattern becomes unstable. As the Rayleigh number is decreased, the convective amplitude decreases, and the phase velocity increases monotonically. If r is increased, the phase velocity decreases and goes to zero at a point denoted by r^*, resulting in a state of stationary overturning convection (SOC)[11] .

DESCRIPTION OF THE EXPERIMENT

The experiments are conducted in a large aspect ratio annular channel of rectangular cross-section which is depicted schematically in Fig. 1(b). The cell is constructed of plastic sidewalls sandwiched between a mirror-polished rhodium-plated copper bottom plate and a sapphire top plate which provides optical access from above. The height of the cell is $d = 0.309 \pm 0.002$ cm and the width and mean circumference are, in units of d, 1.288 and 67.09 respectively. The convection rolls align radially and propagate azimuthally, thus the annular geometry provides periodic boundary conditions in the direction of roll (TW) propagation. The top plate temperature is maintained at $25.000 \pm 0.001°C$, and the bottom plate temperature is varied from $29.6°C$ to $32.0°C$ with similar regulation. The working fluid is a water-ethanol mixture which is 8% ethanol by weight. At the onset of convection, the mean fluid temperature is $27.53°C$ and the fluid parameters are $\Psi = -0.25$, $Pr = 9.16$, and $L = 0.008$ [12]. The fluid is visualized from above using the shadowgraph technique. The image of the convection pattern is recorded by a 720 element annular CCD array.

The Eckhaus boundary is experimentally determined by starting the system in a state of uniform wavelength and slowly decreasing the Rayleigh number until the wavelength of the pattern becomes unstable. By starting with different initial numbers of rolls in the cell, we can determine the points at which each possible wavelength becomes unstable and thus map the Eckhaus boundary which is shown in Fig. 2(a) . This stability boundary is approximately parabolic and has a minimum at a wave number which we denote by k_0. For experimentally realizable initial wave numbers, k_i, the range of Rayleigh numbers at which the Eckhaus instability is encountered is in a small region near the saddle node bifurcation, as is shown in Figs. 1(a) and 2(a). One of the most striking features of our results is that the dynamics of wave number changing events are qualitatively dependent on the value of the local wave number relative to k_0.

The technique of complex demodulation [13] is used to follow the dynamics of the Eckhaus instability. In this technique, small changes to the phase and amplitude of a slowly-varying sinusoidal signal can be computed. From this information, we can calculate the space-time evolution of the frequency, wave number and amplitude of an unstable state. By mapping the wave number of the pattern to a gray scale, the spatio-temporal dynamics can be easily visualized, as is shown for the data in Fig. 3.

In the state shown in Fig. 3(a) , which has an initial wave number $k_i > k_0$, a sinusoidal modulation in the wave number grows in from zero amplitude. The wavelength of this modulation is the longest wavelength which can fit into the annular cell. The evolution of this state, and all experimentally observed states with $k_i > k_0$ proceeds in this manner (i.e., that the instabilities grow from an initial modulation wave number $q \cong 0$), which is identical to the Eckhaus behavior seen in pure fluid convection. However, in contrast to the behavior of the stationary wavelength modulation in the pure fluid system, the wavelength modulation in the binary fluid system propagates. The speed of the modulation is approximately twice the phase velocity of the underlying traveling waves and in the same direction as the phase velocity. The initially sinusoidal

modulation grows in amplitude and narrows in spatial extent, until a roll pair is destroyed in the highly compressed region of the modulation, as shown in Fig. 3(b). Our experiments indicate that this is the generic mechanism by which wave number changes occur for cases where $k_i > k_o$.

Figure 2. In panel (a), the experimentally determined Eckhaus stability boundary is shown. The wave number is measured in units of d, the cell height. In (b), the dispersion relation is shown. Units of ω are 10^{-2} rad/s.
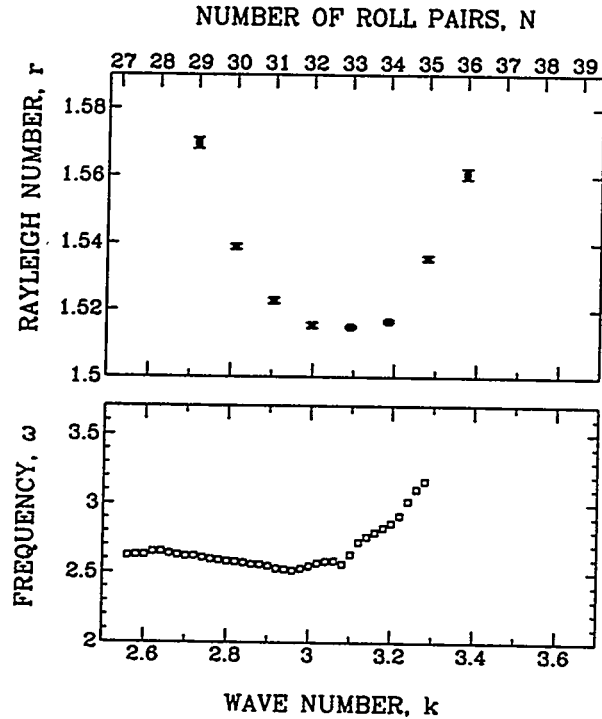
When the initial wave number $k_i < k_o$, the evolution of the system is qualitatively different, as can be seen in Fig. 3(c). In this case, the modulation does not grow from long wavelength, but instead a region of localized dilation develops. This region becomes increasingly dilated and, in contrast to the case where $k_i > k_o$, propagates in a direction opposite the phase velocity with a very slow speed (approximately 1/10th the phase speed). When the amplitude of the wave number modulation grows sufficiently, a new roll pair is created. This newly created roll pair has a local wave number which is greater than k_o, and the resulting wave number modulation propagates away from the point where the new roll pair was created.

Caption for Figure 3 (figure appears on next page)
Figure 3. (a), (b) Evolution of the local wave number in space and time for $k_i > k_o$ at r=1.543, for two time intervals in the same data set. The local wave number is mapped to a gray scale, and the solid lines indicate the motion of a roll boundary, (i.e., the phase velocity of the rolls). The annihilation of one roll pair occurs at t=19.6 x 10^3 s. (c), (d) Evolution of the local wave number for values of initial wave numbers $k_i < k_o$ at r = 1.521, for two time intervals in the same data set. Roll pairs are created at several times, and a roll pair is lost at t = 19.6 x 10^3 s.

167
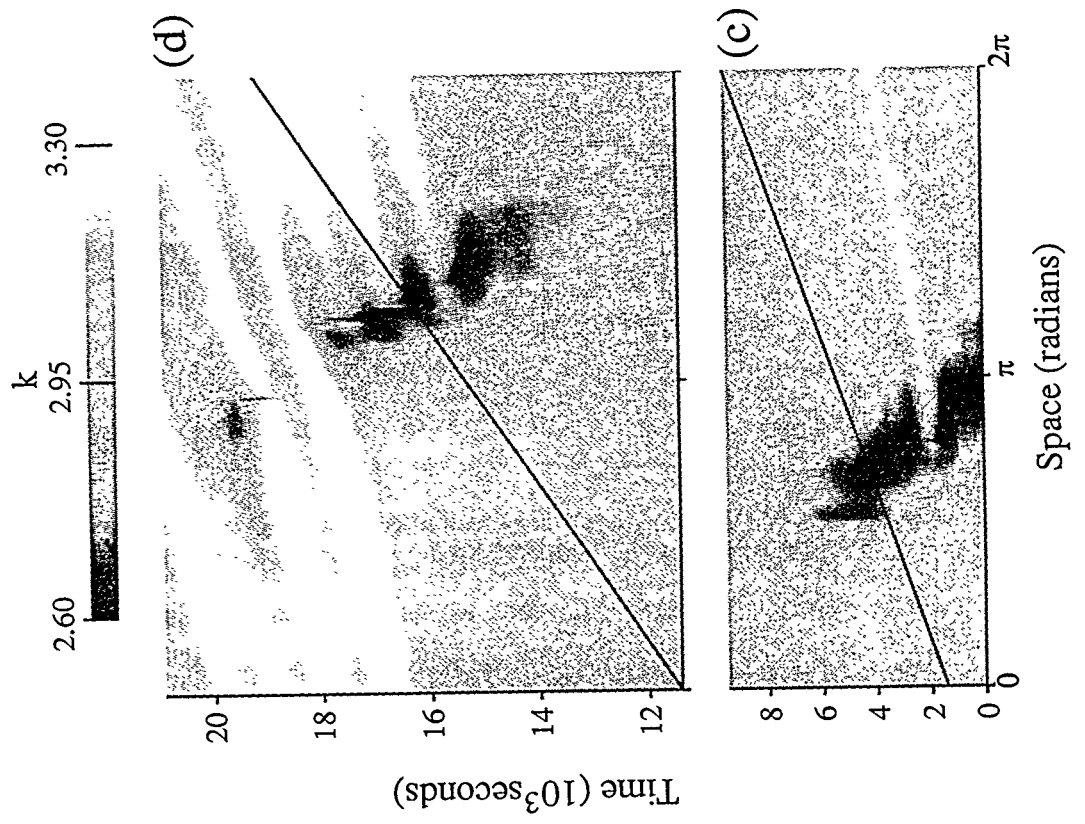
The dynamics of wave number changes can be quite complicated, as can be seen in Fig. 3(d). In this case, the creation event produces a localized region of increased wave number which propagates out of the dilated region. This pulse does not reach the dilated region again until it propagates around the entire length of the cell. For this reason, the dilation continues to be a source for the creation of new roll pairs until they propagate back to the dilation. Thus the dynamics of this wave number-unstable state is dependent on the aspect ratio of the system and the growth rate of the instability. The fact that the wave number compression pulse is advected out of the dilated region gives rise to complicated dynamics. This is evident in the state shown in Fig. 3(d), in which the system over corrects the wave number when the Eckhaus instability is encountered. Instead of increasing the overall wave number by adding one roll pair and bringing the state back into the Eckhaus stable regime, the system over corrects by adding three roll pairs, as the compression pulse propagates out of the dilated region. In an infinite system, we conclude that it is likely that this mechanism will not successfully readjust the wave number, and thus, in such a system, the Eckhaus unstable states with $k_i < k_0$ could not be stabilized by this mechanism. In the infinite case, the dilated region is likely to continue to create a series of wave number compression pulses.

The dispersion relation which characterizes the system can be determined experimentally by computing the wave number and frequency at each space-time point and calculating $\omega(k)$ by averaging the value of ω within small bins in k [5]. A dispersion relation calculated in this manner for the data shown in Fig. 3(c) is shown in Fig. 2(b). The group velocities predicted by the dispersion relation are consistent with the observed modulation group velocities. The qualitatively different behavior for $k > k_0$ and $k < k_0$ can be attributed to the nature of the dispersion relation, which has different characteristic slopes for $k > k_0$ and $k < k_0$.
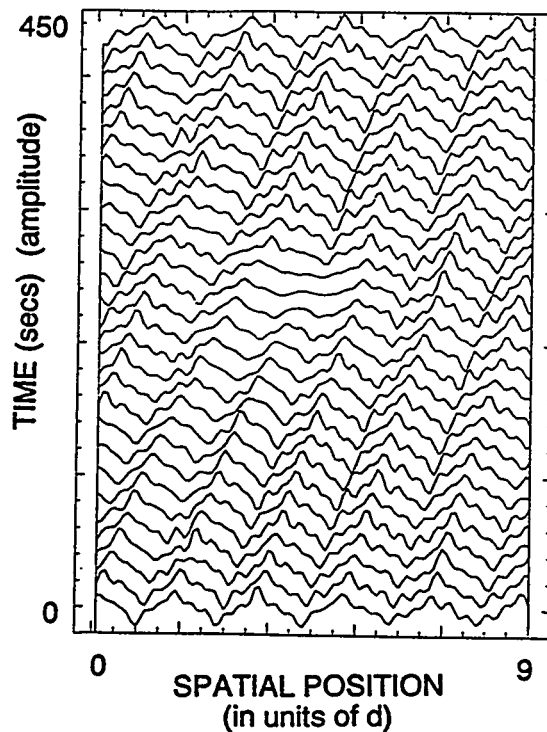

Figure 4. The shadowgraph signal (which is related to the convective amplitude) is shown during an annihilation event. This figure illustrates the rapid time scales on which the annihilation takes place.

It is also interesting to note that the time scale on which creation and annihilation events occur is quite short, as can be seen in Fig. 4, which shows the shadowgraph amplitude when a roll pair is annihilated. For the data shown, this is of the order of one half of the period of the traveling waves. This indicates that diffusion of concentration plays at most a minor role in the annihilation of a roll pair. The creation of a roll pair (e.g., Fig. 3(c) near time 2,000 sec) occurs on a similar time scale. We note in passing that there is information about the concentration field [14] in the shadowgraph signals (e.g., Fig. 4) regarding the concentration field. We have not yet studied this in detail. In contrast to the experimental results of Janiaud et al, we do not see a standing wave near an annihilation event.

SUMMARY AND CONCLUDING REMARKS

In this paper we have presented an overview of our experimental results on wavelength selection and wavelength changing events in traveling-wave convection in a binary fluid mixture. We have found that the wave number changes via propagating wave number modulations. The behavior of wave number selection is qualitatively different depending on the relationship of the initial wave number relative to the most stable wave number, k_0. For initial wave numbers $k_i > k_0$, the wave number modulation grows from zero amplitude at the largest wavelength that can fit into the system. This modulation is propagates at a group velocity that is consistent with the measured dispersion relation. The wave number modulation increases in amplitude and narrows in spatial extent and eventually triggers the annihilation of a roll pair. For initial wave numbers, $k_i < k_0$, the evolution is markedly different. A localized dilated region grows in amplitude and propagates slowly at a speed consistent with the measured dispersion relation in a direction opposite the phase velocity. This region eventually becomes so dilated that a new roll pair is created.

There are numerous open questions raised by our work. Powell and Bernoff have investigated the properties of traveling waves near a saddle-node bifurcation [15]. In an extension of this work, M.C. Cross has developed an amplitude equation analysis based on an expansion about saddle-node solutions [16]. This analysis makes several predictions which can be tested experimentally such as predictions for the growth rate of the instability and the group velocity. The non-linear evolution of the wave number modulation deserves further study and there are speculations that it may exhibit the amplitude-width scaling of a Korteweg - de Vries soliton [4]. The fact that dilations do not grow from $q = 0$ when $k_i < k_0$ but are spatially localized is presently unexplained theoretically and deserves further study. Finally, as we have noted above, another area yet to be explored is the relationship of the wave number modulations to modulations of the underlying concentration field [14].

ACKNOWLEDGMENTS

REFERENCES

*Present address Pennsylvania State University, The Behrend College; Erie, PA.

1. M. LOWE and J. GOLLUB, "Pattern Selection Near the Onset of Convection: The Eckhaus Instability," Phys. Rev. Lett. 55, 2575 (1985).

2. M. DOMINGUEZ-LERMA, D. CANNELL, and G. AHLERS, "Eckhaus Boundary and Wave Number Selection in Rotating Taylor-Couette Flow," Phys. Rev A 34, 4956 (1986).

3. L. KRAMER and W. ZIMMERMANN, "On the Eckhaus Instability for Spatially Periodic Patterns," Physica D 16, 221 (1985).

4. B. JANIAUD, A. PUMIR, D. BENSIMON, V. CROQUETTE, H. RICHTER, and L. KRAMER, "The Eckhaus Instability for Traveling Waves," *Physica D* 55, 269 (1992).

5. G.W. BAXTER, K.D. EATON, and C.M. SURKO, "Eckhaus instability for traveling waves," *Phys. Rev. A* 46, 1735 (1992).

6. P. KOLODNER, "Extended States of Nonlinear Traveling-Wave Convection: I. The Eckhaus Instability," *Phys. Rev. A* 46, 6431 (1992) and "Observations of the Eckhaus Instability in One-Dimensional Traveling-Wave Convection," Phys. Rev. A 46, 1739 (1992).

7. D. HURLE and E. JAKEMAN, " Soret-Driven Thermosolutal Convection," J. Fluid Mech. 47, 667 (1971).

8. W. BARTEN, M. LÜCKE, and M. KAMPS, "Structure and Dynamics of Nonlinear Convective States in Binary Fluid Mixtures," in *Nonlinear Evolution of Spatiotemporal Structures in Dissipative Continuous Systems* , Plenum Press, New York (1990).

9. W. BARTEN, M. LÜCKE, W. HORT, and M. KAMPS, "Fully Developed Traveling-Wave Convection in Binary Fluid Mixtures," *Phys. Rev. Lett.* 63, 376 (1989).

10. D. BENSIMON, A. PUMIR, and B.I. SHRAIMAN, "Nonlinear Theory of Traveling Wave Convection in Binary Mixtures," *J. Phys. (Paris)* 50, 3089 (1989).

11. D.R. OHLSEN, S.Y. YAMAMOTO, C.M. SURKO, and P. KOLODNER, "Transition from Traveling-Wave to Stationary Convection in Fluid Mixtures," *Phys. Rev. Lett.* 65, 1431 (1990).

12. P. KOLODNER, H. WILLIAMS, and C. MOE, "Optical Measurement of the Soret Coefficient of Ethanol/Water Solutions," *J. Chem. Phys.* 88, 6512 (1988).

13. P. BLOOMFIELD, "Fourier Analysis of Time Series: An Introduction," (Wiley, New York, 1976), pp. 118-150.

14. K.D. EATON, D.R. OHLSEN, S.Y. YAMAMOTO, C.M. SURKO, W. BARTEN, M. LÜCKE, M. KAMPS, and P. KOLODNER, "Concentration Field in Traveling-Wave and Stationary Convection in Fluid Mixtures," *Phys. Rev. A* 43, 7105 (1991).

15. J. POWELL and A. BERNOFF, "Saddle-Node Bifurcation of Slowly-Varying Nonlinear Traveling Waves," unpublished.

16. M. CROSS, unpublished.

RADIATIVE TRANSFER THROUGH ARRAYS OF DISCRETE SURFACES

James R. Welty and Joseph R. Zaworski

M. Kevin Drost

Oregon State University
Corvallis, OR 97331

Battelle Pacific Northwest Laboratory
Richland, WA 99352

ABSTRACT

Radiant transport involving arrays of discrete surfaces constitutes one of the major unresolved problems in the field of radiation heat transfer. This paper discusses the requirements for experimental validation of a general Monte Carlo solution to this class of problems. This work is a collaborative effort between Oregon State University, where the experimental portion is being accomplished, and the Pacific Northwest Laboratory, which is responsible for the Monte Carlo simulation.

The design and calibration of a simple, compact, and flexible instrument for direct measurement of bidirectional reflectance are presented in some detail. The capability to measure full bidirectional reflectance, as provided by this instrument, is essential to an accurate portrayal of surface properties in a Monte Carlo simulation. Measured data for a common flat white paint are presented and clearly demonstrate the need for accurate and complete surface property information.

INTRODUCTION

Arrays of fixed, discrete absorbing and reflecting surfaces are encountered in a variety of circumstances of practical interest. Examples include ceramic fabrics, fiberglass insulation, and the absorbing section of a central solar receiver.

A consideration of ceramic fabrics, for example, concerns a material which is fabricated from yarn that is composed of small ceramic fibers. If radiant interaction with these small fibers is considered, Mie scattering is encountered. When yarn is evaluated, the dimensions are sufficiently large that photon/surface interactions can be modeled at the geometric limit.

Individual fibers can have many cross-sectional shapes and a wide range of surface coatings. These fibers can then be formed into yarns with various dimensions. In turn, the yarns can be woven into fabrics with a range of yarn spacings and orientations. This range of variability in construction, in addition to the range of properties that individual fibers may have, indicates the wide range of optical properties that can be built into these materials.

The example of ceramic fabrics illustrates the broad spectrum of characteristics that may be encountered in surface arrays. When the array elements are very small in physical size, are closely packed, and are completely random in orientation, they may be treated as a continuous absorbing/scattering medium and modeled using techniques similar to those employed for gases and aerosols. When the individual array elements become large, and separated by distances which are large relative to the wave length of the thermal radiation, then the resulting radiant transport will be much different, and will vary principally on the array geometry and the properties of the surfaces involved.

An approach for solving these discrete surface problems, using Monte Carlo techniques, is described by Drost and Welty [1] and Drost and Palmer [2]. The Monte Carlo approach has become popular in recent years due to the development of more advanced — principally faster — computer hardware. Using such an approach, full advantage

can be taken of the detailed surface property descriptions of the surfaces involved. One such property, which is fundamental to a complete description of radiant transport in an array, is the bidirectional reflectance. It is the ability to evaluate this property which is the subject of the remainder of this paper.

Bidirectional reflectance is a material surface property that is fundamental to many types of radiative transfer calculations. An indication of the importance of this property is given by the fact that there are literally hundreds of archival publications describing methods for analytically estimating reflectivity, explaining and modeling the effects of variables like surface roughness and polarization, and describing the results of experimental measurement of reflectance properties (see for example, [3,4]). Although analytical methods have been developed for predicting surface properties [5,6], their application is often of limited value for use with materials that have been abraded, oxidized, or had some other action change their surface properties. In these cases, experimental data are required.

Many types of radiative transfer problems are modeled in a such a way that reflectance properties are used only once for each surface. A simple case would be a flat plate with a beam impinging at a particular incident angle with the resulting absorption and reflection being functions of the surface properties. The uncertainty associated with these models includes the uncertainty of the reflectance only once because any given photon hits a surface only once. In more complex cases the situation can be quite different. For example, in the case of parallel plates in which the incident beam reflects many times between the surfaces, or with an array of surfaces through which radiative transfer takes place, each photon may strike a surface many times and the surface properties must be used each time. Monte Carlo models are often used in circumstances such as this, where a photon (or bundle of photons) may go through many surface interactions before it is either completely absorbed or it leaves the region of interest. In this case, the uncertainty associated with reflectance may be compounded several times in the calculation of overall uncertainty.

To the best of our knowledge, there have been no Monte Carlo codes reported that make use of full bidirectional reflectance data. Virtually all codes that model in three dimensions assume at least one, and sometimes two or three axes of symmetry. A common assumption is to assume azimuthal symmetry for the incident beam; i.e. reflectance properties don't change with respect to the azimuth angle of the incident beam, only with respect to the incident beam polar angle. This is a reasonable assumption for many types of surfaces that are smooth either because the surface has been carefully prepared (as in a laboratory), or because of a filling process, such as painting, which naturally results in a smooth surface. However, this assumption of azimuthal symmetry does not seem reasonable for many common engineering materials containing non-random surface features, such as brush-finished stainless steel, extruded aluminum, any material that has been machined, or materials that have been sanded in one direction. For these materials, a full set of bidirectional reflectance data is required to accurately describe the material reflectance properties and it is for this reason that the bidirectional reflectometer described in this paper was developed.

In the sections that follow, a detailed description of the bidirectional reflectometer, its operation, and some example data are presented. The apparatus is described in detail, including its construction, the alignment and calibration procedures, operational procedures, and a discussion of uncertainty.

NOMENCLATURE

The nomenclature used in this discussion follows convention (see for example [7]). The word reflectivity is reserved for describing an optically smooth uncontaminated surface; reflectance is used with measured properties where there are no constraints on surface conditions. Geometric descriptions are based on a reference system that is attached to the surface of interest; the incident beam and the reflected beam directions are defined by two angles each (Figure 1). The bidirectional spectral reflectance is then defined as

$$\rho'' \left(\lambda,\theta_i,\phi_i,\theta_r,\phi_r\right) = \frac{i''_{\lambda,r}\left(\lambda,\theta_i,\phi_i,\theta_r,\phi_r\right)}{i'_{\lambda,i}\left(\lambda,\theta_i,\phi_i\right)\cos\theta_i \, d\omega}$$

where:

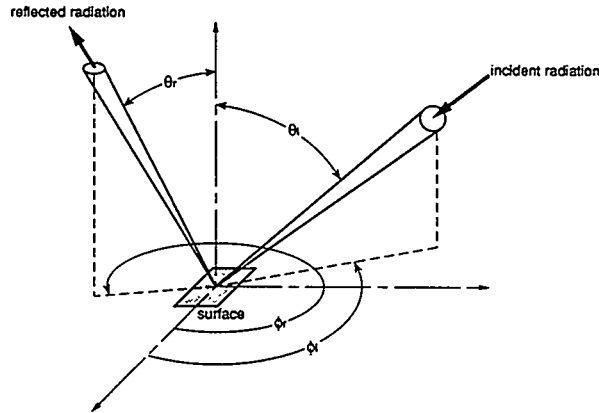|				
ρ	reflectance (BDRF in this definition)		ω	solid angle
λ	spectral quantity (i.e., wavelength)		$'$	directional (superscript)
θ	polar angle as measured from a normal to the surface		$''$	bidirectional (superscript)
ϕ	azimuthal angle as measured from a reference on the surface		i	incident (subscript)
i	intensity		r	reflected (subscript)
			λ	spectral quantity (subscript)

FIGURE 1

Definition of Angles Used in Nomenclature for Bidirectional Reflectance

Examination of this definition reveals that the reflectivity defined in this way can be greater than 1. For this reason, the name bidirectional reflectance function (BDRF) is usually used for this quantity.

In addition to BDRF, the directional-hemispherical spectral reflectivity is also a useful quantity. It can be obtained by multiplying the BDRF by cos θ_r, the area of the sensor, and the solid angle of the reflected beam and then integrating over the entire hemisphere [7]. The result is given by:

$$\rho'_\lambda \left(\lambda, \theta_i, \phi_i\right) = \int \rho''_\lambda \left(\lambda, \theta_i, \phi_i, \theta_r, \phi_r\right) \cos \theta_r \, d\omega_r$$

Approximating the integral with a summation of bidirectional data over the hemisphere will allow comparison with the results from an integrating sphere.

DETAILS OF THE REFLECTOMETER

As implied in the introduction, there have been numerous devices built for measuring BDRF (see for example [8-11]). The design of the reflectometer used in this project evolved from an apparatus similar to the one developed by Hsia [10] to a completely new apparatus based in part on the approach used by De Silva [8]. The features that make this reflectometer particularly useful are (1) resolution of 1/2 degree for each of the four angles (θ_i, ϕ_i, θ_r, ϕ_r), (2) complete hemispheric coverage with the exception of a small cone around the incident beam and a small band at the base of the hemisphere where θ_r approaches 90 degrees, (3) high sensitivity for use with low reflectance materials, (4) the ability to easily use virtually any type of source for the incident beam, and (5) direct reading of the four angles that define incident and reflected directions.

The entire apparatus is shown schematically in Figure 2 and details of the goniometer are shown in Figure 3. The reflectometer can be considered in terms of three major subsystems: the source, the goniometer, and the detection system. In the course of subsequent descriptions, note that the reference coordinate system is located on the sample of interest. The incident beam is fixed and the sample/sensor apparatus rotates around the point at which
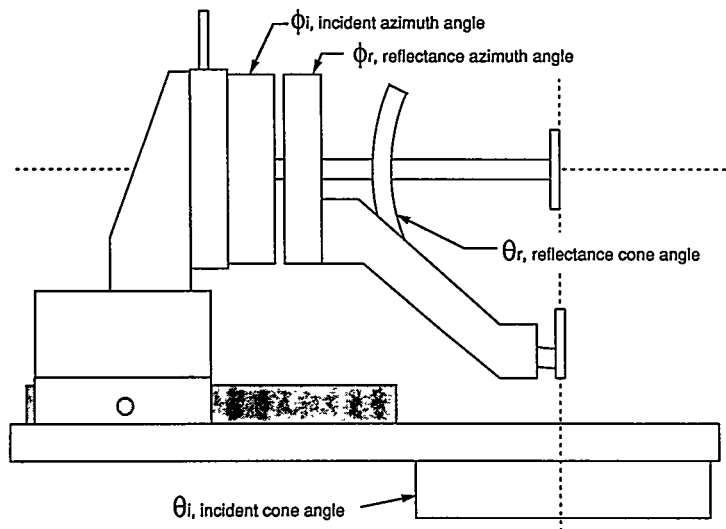
FIGURE 2

A schematic representation of the apparatus
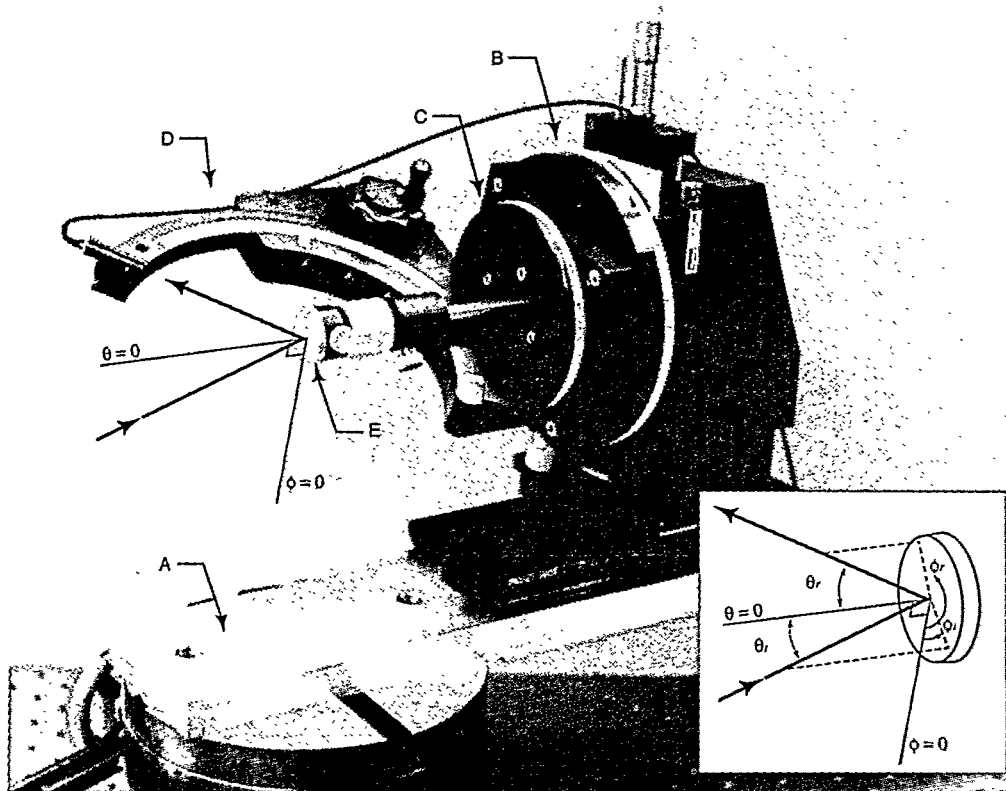(1) goniometer; (2) collimating lens; (3) spatial filter; (4) chopper; (5) HeNe laser

FIGURE 3

A photograph of the goniometer. The source for the incident beam is mounted out of the photograph on the optical rail just showing in the lower left corner of the photograph. The inset is a drawing of the reference frame as it would be positioned on the sample surface (E).

175

the incident beam intersects the front plane of the sample. Figure 1 (the standard notation for BDRF) has been redrawn in the inset of Figure 3 to match the orientation of the sample in the goniometer.

The Source

One of the advantages of this arrangement is that the source is fixed in position; bidirectional measurements over nearly the entire hemisphere are accomplished by moving only the sample and the sensor. This means that virtually any source can be used because there are no size, weight, or orientation constraints as might exist if the source was a moving part of the goniometer system. In fact, a 0.5 mW HeNe laser, a 5 mW HeNe laser and a Quartz-Tungsten Halogen (QTH) source have already been used with this apparatus and a 2 W Argon laser is mounted on the same table and available if needed. The source used for the work reported in this paper was a 5 mW HeNe laser operating at 632.8 nm.

As described in detail in the section on the sensor, two source configurations were evaluated for use with this apparatus: a small-diameter nonuniform beam and a large-diameter uniform beam. In both cases, the beam was collimated and monochromatic. When the source was a laser, the output of the laser was used directly for the narrow band beam. This beam had an output of either 0.5 or 5 mW depending on which laser was used, the wavelength was 632.8 nm, the beam diameter was on the order of 1 mm, and the beam intensity distribution was approximately gaussian. For the large-diameter beam, a spatial filter consisting of a focusing lens, a 0.03 micron pinhole, and appropriate positioning verniers was used to expand the beam. An additional lens was used to recollimate the center portion of the beam to provide a monochromatic, collimated beam of approximately 25 mm in diameter with uniform intensity. Only the higher power laser (5 mW) was used for the wide beam.

The Goniometer

The incident beam is horizontal and impinges directly on a sample mounted in the goniometer apparatus (Figure 3). The entire sample/sensor apparatus sits on a rotation stage (A); changing the orientation of the apparatus with this stage changes the incident beam polar angle, θ_i. Mounted on stage (A) but oriented vertically is another rotation stage (B). The sample (E) is mounted directly to this stage so that rotating (B) changes the azimuth angle for the incident beam, ϕ_i.

This arrangement effectively allows the angles defining the reflected beam direction to remain unchanged as the incident angles are varied; i.e., the sensor rotates with the sample and is therefore maintained in the same position relative to the (sample) coordinate system as both θ_i and ϕ_i are changed.

Coupled directly to rotation stage (B) is rotation stage (C) for changing the sensor azimuth angle, ϕ_r. This stage has a hole through its center to allow the sample post to come directly out from the center of stage (B). Finally, mounted on the sensor azimuth stage (C) is an arc (D) on one end of which the sensor is mounted. This arc can be moved through 90 degrees to change the sensor polar angle, θ_r.

For convenience, to speed alignment, and to be able to accommodate different-thickness samples, stage (A) is mounted on an X-Y positioner, stage (B) is mounted on a vertical positioner, and the sample is held in an adjustable-height post holder.

The Detection System

The detection system consists of a chopper to modulate the incident beam, a photodiode mounted in a baffled sensor housing, a lock-in amplifier, and a computer used both for control of the lock-in amplifier and to record data as they are collected. For purposes of discussion, the system is considered in two parts: the sensor and the amplifier.

Although some researchers have used a 'bare' photodetector [8], this apparatus makes use of a sensor housing to increase the directional sensitivity of the sensor. As described in Nicodemus et al. [12], there are two practical approaches to the geometric relationship between source, sample, and sensor size. First, the incident beam (source) can have a small area, in which case the sample and sensor must have areas large enough to encompass the entire beam at the largest incident polar angle (θ_i) to be used. Alternatively, the sample and sensor can be small, in which case the incident beam must be bigger than the area on the sample from which the sensor receives radiation. Both approaches have been evaluated with this apparatus.
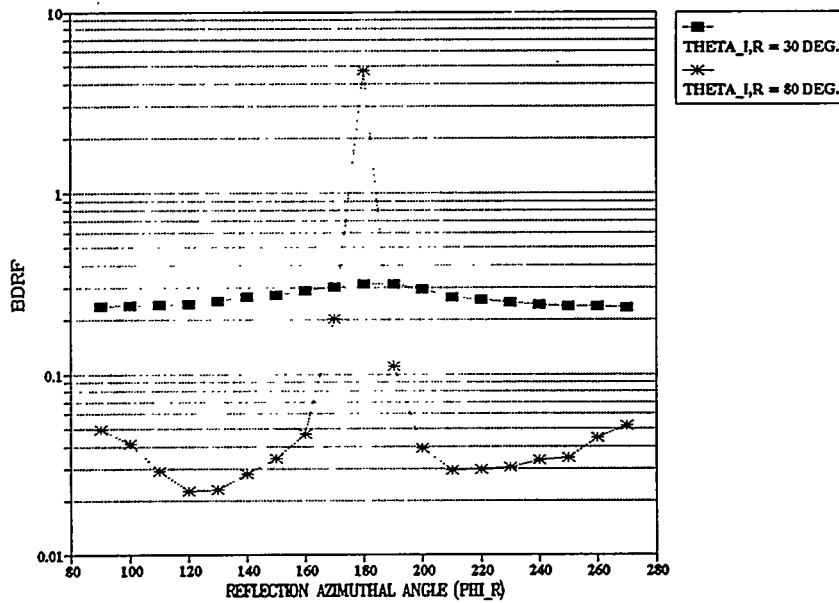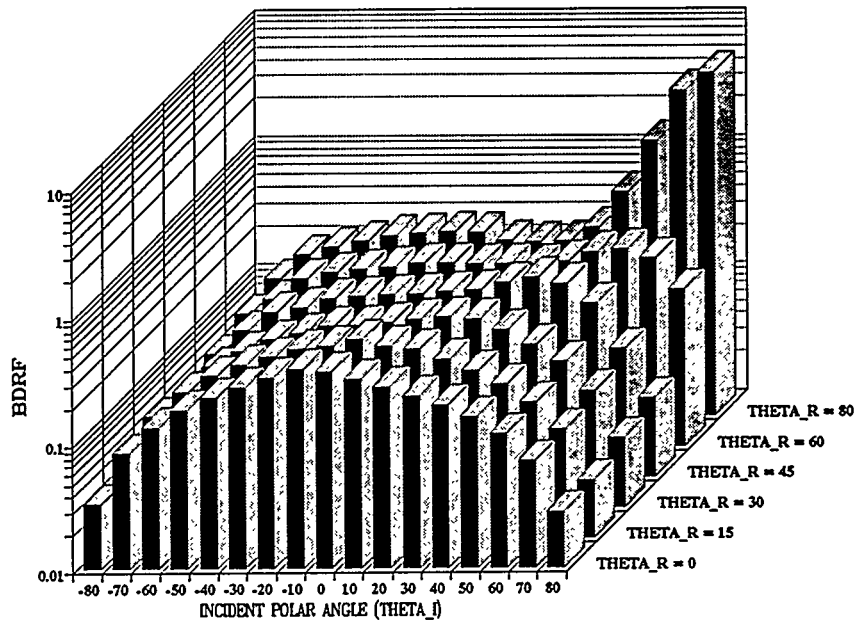
FIGURE 4

Results of BDRF Measurements Taken for Krylon Flat White Paint (No. 1502) on a Smooth Aluminum Substrate. The top plot shows BDRF for cases where the incident and reflected beams are in the same plane (i.e., $\phi_i = \phi_r$, $\phi_r + 180$). The BDRF is plotted as a function of incident polar angle and reflected polar angle. The bottom plot shows out-of-plane BDRF. Here the variation is in reflected azimuthal angle at specular reflection angles of 30 and 80 degrees.

In the case of the first approach, a laser beam of approximately 2 mm diameter was aimed at the sample. The sensor, a 10 mm^2 photodiode, was just large enough to accept the entire beam. Although a larger sensor would be desirable, this was adequate for evaluation of the large area approach.

The second approach, using a sensor with a small acceptance angle, was tested using the same 10 mm^2 photodiode, but with a series of baffles in the sensor housing to restrict the acceptance angle to approximately 1.9 degrees (plus or minus 0.94 degrees), which corresponds to a solid angle of 0.00084 sr.

In both cases, the sensor was mounted on top of the goniometer arm. As can be seen in Figure 3, this arm is below the azimuthal axes of rotation (ϕ_i, ϕ_r) so that when the sensor is mounted on the arm surface, the sensor axis is coincident with the other three goniometer axes and the center of the incident beam. Having the arm offset from the axis of rotation allows the incident beam to reach the sample for all goniometer positions except when the sensor is directly in line with the incident beam.

The output of the sensor, a voltage that would be dc except that it is being modulated by the chopper, is fed directly into the lock-in amplifier. A reference frequency generated by the chopper is also connected to the amplifier. Because the frequency of the signal of interest (the photodiode output) is known precisely, the lock-in is able to act as a filter with a very narrow bandwidth. When coupled with a high gain amplifier, the result is an ability to amplify and extract signals that are below the ambient noise level. In this particular case, even though the output of the photodiode was in the nanovolt range, use of the lock-in amplifier allowed work to be conducted in ambient light conditions. The only constraint resulting from the use of a lock-in under these conditions is that the time constants required for accurate readings result in periods on the order of minutes for each data point.

SAMPLE DATA

A number of materials have been tested using this reflectometer. As described in the introduction, BDRF data are necessarily voluminous in nature. Therefore, only partial results for a common flat-white paint are included in this paper. These results have been selected to demonstrate the importance of considering full BDRF data when modeling common types of materials.

All of the BDRF data shown is for Krylon Flat-White paint (No. 1502). Two coats of the paint were applied to a smooth aluminum substrate. The sample was then allowed to age in the laboratory for two weeks prior to the start of BDRF measurements. The incident beam is from a He-Ne laser operating at 632.8 nM with random polarization.

The example BDRF data is shown in Figure 4. It is particularly clear in the bar plot that this paint is mostly diffuse for angles of incidence less than about 60 degrees, but that reflection becomes increasingly specular as angles increase above that value. The conclusion to be drawn is that if these circumstances of coated surface and incident beam are to be used in a situation where multiple reflections are likely, the model used for analysis should not ignore the change in specularity of reflection as a function of incident angle.

CONCLUSIONS

An apparatus for the measurement of BDRF has been described in detail. The key features that set it apart from previous work are: (1) direct reading of all angles involved, (2) nearly complete hemispheric coverage, (3) the ability to measure incident flux directly with the same sensor as used for reflected flux, (4) a goniometer that moves the sample and sensor about all four axis therefore providing great flexibility in the source used for the incident beam, (5) linear response over five orders of magnitude in intensity, and (6) a minimum of custom machining (only one axis required a custom rotation machined stage). The opportunities for improvement fall into the categories of operational improvements and accuracy improvements.

Improvements in accuracy can be achieved by improving the quality of the source beam both in terms of uniformity and stability, by using a more precise method of measuring the area of the sensor and its distance from the sample, and by increasing the resolution of the scales used on the goniometer. All of the operational improvements relate to further automation of the data collection process. Specifically, each of the axis of rotation could be motorized and the existing computer program for data acquisition could be extended to include control of the goniometer motion.

This reflectometer has been used to evaluate the BDRF of several types of common engineering materials. It is clear that for some materials the traditional practice of assuming azimuthal symmetry, and perhaps even the practice of modeling reflectance as a linear combination of specular and diffuse components, needs to be re-evaluated in light of the common availability of computational resources with the power to complete numerical analysis without those simplifications.

ACKNOWLEDGMENT

BIBLIOGRAPHY

1. M.K. DROST and J.R. WELTY, "Monte-Carlo Simulation of Radiation Heat Transfer in Arrays of Fixed Discrete Surfaces Using Cell-to-Cell Photon Transport, in *Proc. of the 28th National Heat Transfer Conference*, A.S.M.E., San Diego, CA (1991).

2. M.K. DROST and B. PALMER, "Aspects of Radiative Heat Transfer in Arrays of Fixed Discrete Surfaces," *Eleventh Symposium on Energy Engineering Sciences*, Argonne, IL (May 1993).

3. J.C. RICHMOND and J.J. HSIA, "Bidirectional Reflectometry, Part II, Bibliography on Scattering by Reflection from Surfaces," *Journal of Research of the NBS (Physics and Chemistry)* 80A(2), 207-220 (March-April 1976).

4. Y.S. TOULOUKIAN, D.P. DeWITT, and R.S. HERNICZ (eds.), "Thermal Radiative Properties: Coatings," vol. 9 of *Thermophysical Properties of Matter*, Plenum Press, New York (1970)

5. M.Q. BREWSTER, *Thermal Radiative Transfer & Properties*, John Wiley & Sons, New York (1992).

6. C.F. BOHREN and D.R. HUFFMAN, *Absorption and Scattering of Light by Small Particles*, John Wiley & Sons, New York (1983).

7. R. SIEGEL and J.R. HOWELL, *Thermal Radiation Heat Transfer*, McGraw-Hill Inc., New York (1972).

8. A.A. De SILVA and B.W. JONES, "Bidirectional Spectral Reflectance and Directional-Hemispherical Spectral Reflectance of Six Materials Used as Absorbers of Solar Energy," *Solar Energy Materials* 15(5), 391-401 (1987).

9. E.R. MILLER and R.S. Vun KANNON, "Development and Use of a Bidirectional Spectroreflectometer," *Progr. Aeron. Astron.* 20, 219-233 (1967).

10. J.J. HSIA and J.C. RICHMOND, "Bidirectional Reflectometry, Part I, A High Resolution Laser Bidirectional Reflectometer with Results on Several Optical Coatings," *Journal of Research of the NBS (Physics and Chemistry)* 80A(2), 189-205 (March-April 1976).

11. G.M. KEATING and J.A. MULLINS, "Vectorial Reflectance of the Explorer IX Satellite Material," NASA TN-D-2388 (August 1964).

12. F.E. NICODEMUS, J.C. RICHMOND, and J.J. HSIA, "Geometrical Considerations and Nomenclature for Reflectance," *NBS Monograph*, 1-52 (October 1977).

ASPECTS OF RADIATION HEAT TRANSFER IN ARRAYS OF FIXED DISCRETE SURFACES

M. Kevin Drost and Bruce J. Palmer
Pacific Northwest Laboratory[a]
Richland, Washington

James R. Welty
Oregon State University
Corvallis, Oregon

ABSTRACT

Arrays of fixed discrete surfaces are encountered in a number of important applications. Evaluating radiant heat transfer in an array of fixed discrete surfaces is challenging because array optical properties are often nonhomogeneous and anisotropic. This article presents the results of a Monte Carlo simulation of radiation heat transfer in several array geometries. The results show that for the array geometries included in the study, the extinction coefficient is strongly anisotropic and that optical properties are dependent on both the geometric arrangement of the elements and the scattering characteristics of individual elements.

INTRODUCTION

Arrays of fixed discrete surfaces can be encountered in a range of applications. Examples include volumetric air heating solar central receivers [1], ceramic fabrics [2], and fibrous insulation [3]. In most applications involving radiative heat transfer in participating media, optical properties such as extinction coefficient and anisotropic scattering are treated as being independent of incident angle. When the orientation of an absorbing array element is fixed, the scattering phase function depends on the angle of incidence, as well as the angle of reflection [4].

The objective of this research was to evaluate radiation heat transfer in a range of array geometries. A typical array is shown in Figure 1. Monochromatic collimated radiation impinges on an array of isothermal fixed discrete surfaces at a variable incident angle. The array is enclosed in either specular or black boundaries. Radiation between isothermal array elements and from the array to the surroundings was not included in the analysis.

The research documented in this paper developed and applied an innovative Monte Carlo model to evaluate radiation heat transfer in arrays of fixed discrete surfaces [5]. The Monte Carlo model was used to simulate radiation heat transfer in a range of array geometries with varying surface properties. The results give an indication of the challenges associated with modeling radiation heat transfer in arrays of fixed discrete surfaces.
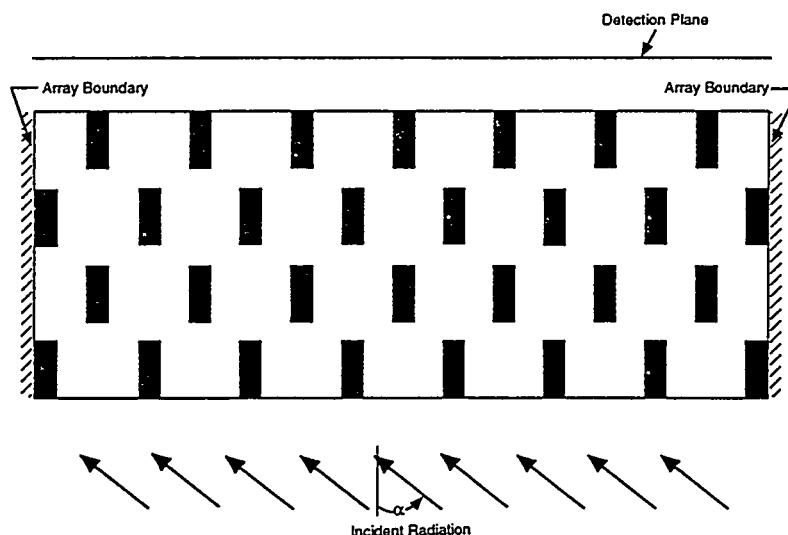

Figure 1. Typical Array of High Aspect Ratio Elements

MONTE CARLO MODEL

Monte Carlo modeling has been widely applied to radiation heat transfer problems and the method is well documented [6,7,8]. The Monte Carlo simulation used in this study divides the array into computational cells where each cell contains one array element. The cell-to-cell transport algorithm of Drost et al. [1] was implemented in the MCLITE computer code for simulating two-dimensional arrays. A photon is initially emitted into an exterior cell and interacts with the element in that cell, resulting in the photon being absorbed, reflected out of the array, or transmitted to an adjacent cell. The procedure is repeated, tracking the photon as it moves from cell to cell, until the photon is either absorbed or exits the array.

The cell-to-cell transport scheme divides the array into a set of parallel zones, each of which has the same width as the array, L_w, and then divides the zone into cells. Each cell has the same height as the zone but the cell width is arbitrary. The only constraint is that the sum of all cell widths within a zone is equal to the zone width. The array is assumed to be enclosed in a rectangular boundary in the xy plane. The faces of the array through which photons enter and exit are oriented parallel to the x axis. The y axis points into the array. The face of the array through which photons enter is located at $y=0$ and the left hand boundary of the array is fixed along the line $x=0$. The right hand boundary is located at $x=L_w$. The sum of the zone heights is equal to the height of the array, L_h, and photons exit the array by crossing the line at $y=L_h$. The geometry of the cells and zones is illustrated schematically in Figure 2.

The boundaries of the array at $x=0$ and $x=L_w$ can be treated as either regular surfaces or periodic boundaries. If the boundaries are treated as regular surfaces, photons encountering them can be absorbed, specularly reflected, or diffusely reflected. If the boundaries are periodic, a photon that exits one side of the array enters the array from the other side traveling in the same direction and with the same (y,z) coordinate.

Cell-to-cell photon transport requires two sets of calculations. The first set determines the movement of the photon from one cell to the next; the second determines the outcome of a photon/cell interaction. The cell-to-cell tracking calculations identify which cell in the array the photon currently occupies. The photon is initially emitted into an external cell in the array. At the beginning of the photon/cell calculation, the photon is located at the edge of the cell with a known
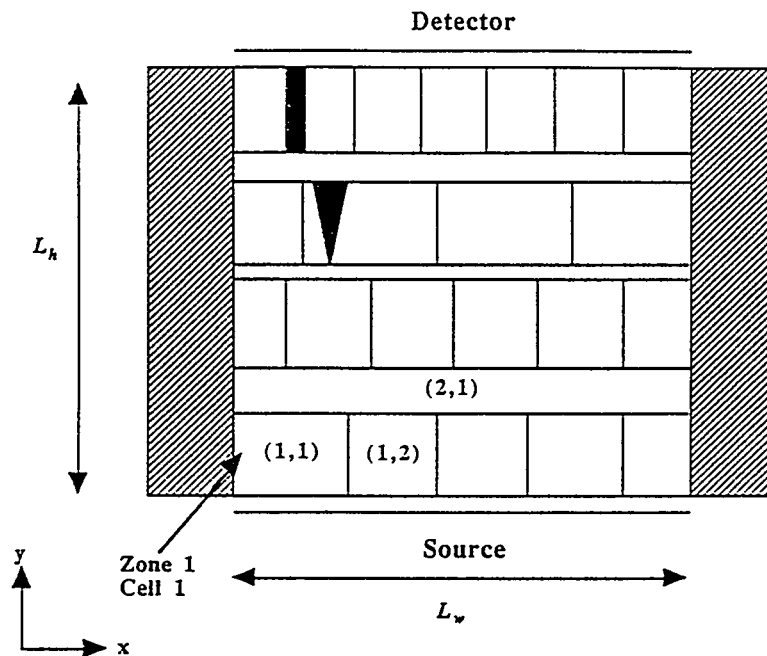
181

Figure 2. Cell Model

location and direction. The photon is directed towards the interior of the cell. When the photon/cell interaction is complete, the photon is again located on the boundary of the cell with a known location and direction. The photon trajectory is now directed towards the exterior of the cell. The cell-to-cell computation then identifies the cell that the photon enters next, the data is reorganized so that the photon is poised on the boundary of the cell that it enters next, with a known location and direction, and the next photon/cell interaction calculation is performed. This process is repeated until the photon is absorbed or exits the array. The cell-to-cell tracking scheme is independent of the photon/cell calculations, which gives the MCLITE code a convenient, modular structure. Additional array element types can be added to the code by writing the corresponding photon/cell interaction routines, without seriously modifying any other portions of the program.

A photon's trajectory within a cell is determined by a series of cell models where each cell contains a single element. MCLITE currently supports routines for calculating photon/cell interactions in cells containing elements with circular, rectangular, and triangular cross sections. It also has a routine for calculating the trajectory of a photon through an empty cell. As part of the calculations, the location and results of interactions between photons and solid surfaces in the cell are determined.

The use of computational cells simplifies the calculation of photon trajectories by reducing the number of surfaces that need to be considered as candidates for the next photon/surface interaction. For each photon/cell interaction, the program only needs to consider the surfaces of the array element contained within the cell and the surfaces representing the cell boundary. At the expense of additional program complexity, the number of surfaces that must be considered can often be reduced even further, depending on where the photon enters the cell in relation to the array element contained within the cell.

Most of the calculations required to evaluate the trajectory of a photon inside a cell consist of finding the intersections of various straight lines. The photon trajectory, as well as most of the elements within the cell and the cell boundary itself, are composed of straight line segments. The only exception is for cells

182

containing circular elements. The most convenient method for performing these calculations is to express the straight lines as parameterized vector equations of the form

$$\vec{X}(\tau) = \vec{r} + \tau\vec{s} \qquad (1)$$

where s is the direction that the photon is traveling. The intersection of two line segments in two dimensions can be computed by solving the two simultaneous equations for each line segment. This is a straightforward algebraic calculation that avoids any trigimetric functions, so it is performed quickly on most computers.

For cells containing circular elements, the intersection of the photon trajectory with a circle is also a relatively simple calculation. The circle is defined by the equation

$$2|\vec{X} - \vec{r}_0| = a^2 \qquad (2)$$

where the a is the radius of the circle. The intersection of the photon with the circle can be found by solving Equation (2) for τ

$$|\vec{r} + \tau\vec{s} - \vec{r}_0|^2 = a^2 \qquad (3)$$

If the photon trajectory intersects one of the solid surfaces in the array, the program accesses a subroutine that computes the outcome of the photon/surface interaction. The input for this routine is the direction of the incident photon, the normal vector to the surface at the point of intersection (h), a parameter representing the photon's energy, and the relevant surface properties. The subroutine calculates the direction and energy of the outgoing photon. For specularly reflected photons, the direction of the outgoing photon is given by the formula

$$\vec{s}_f = \vec{s}_i - 2(\vec{s}_i \cdot \hat{n})\hat{n} \qquad (4)$$

where s_i and s_f are the pre- and post-collision directions of the photon. For diffuse reflections, the calculation is more complicated because a local coordinate system needs to be constructed at the location of the surface/photon interaction. The output from the calculation is the same as for specular reflections. The choice of diffuse or specular reflection is random, with the relative probabilities determined by the diffuse and specular reflectivities.

In addition to calculating trajectories through the array, MCLITE has options that allow the user to specify different source configurations for illuminating the array. The program also collects a broad range of data on the simulation including total reflectivities, absorptivities, transmissivities, and zone absorbtivities. The intensity of transmitted photons as functions of position and direction are also calculated.

RESULTS

Sample results from the Monte Carlo simulation are presented to illustrate the complexities associated with modeling radiation heat transfer in arrays of fixed discrete surfaces. Three array geometries were considered. The first array is shown in Figure 1 and includes fin-shaped elements with an element aspect ratio of 3. The second array is shown in Figure 3 and consists of widely dispersed elements with square cross-sections. The third array is similar to the array shown in Figure 3, except that

183

Detection Plane

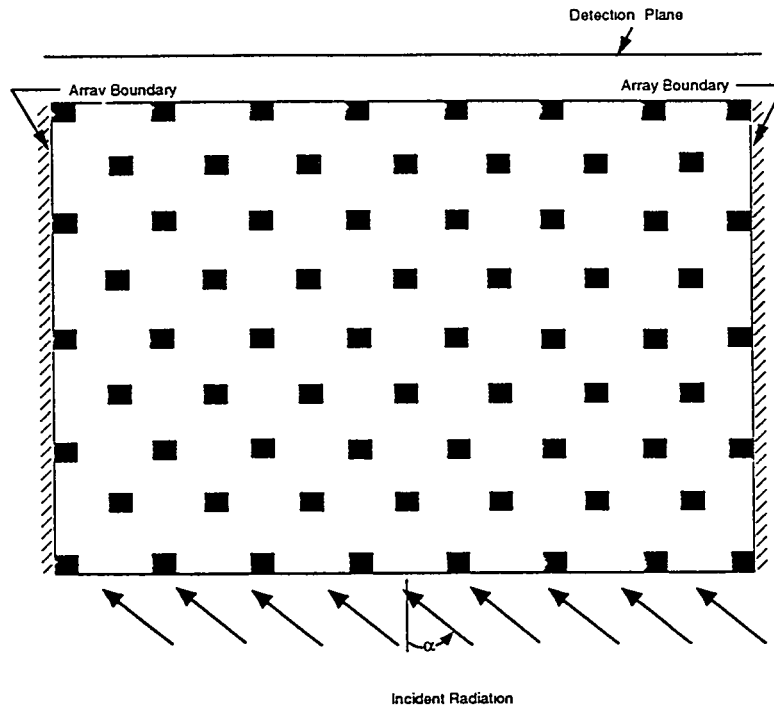Array Boundary

Array Boundary

α

Incident Radiation

Figure 3. Array of Square Elements

the square elements are replaced with cylindrical elements. The cylindrical elements are assumed to have a diameter equal to the width of the square elements used in the second array. It was initially assumed that widely spaced cylindrical elements would be most likely to exhibit homogeneous array optical properties.

The array geometries were simulated using the Monte Carlo code for three sets of surface properties: a specularly reflecting case, a diffusely reflecting case, and a case that included absorption by array elements. The cases are summarized in Table 1. Each case involved calculating the transmission of radiation through the array for six incident angles ($\alpha = 0$, $\pi/16$, $\pi/8$, $3\pi/16$, $\pi/4$, $3\pi/8$).

TABLE 1. Characteristics of Cases

	Case 1	Case 2	Case 3	Case 4	Case 5	Case 6	Case 7	Case 8	Case 9	Case 10	Case 11	Case 12
Element Width	1	1	1	1	1	1	1[a]	1[a]	1[a]	1	1	1
Element Length	3	3	3	1	1	1	1[a]	1[a]	1[a]	3	3	3
Element Spacing	4	4	4	4	4	4	4	4	4	4	4	4
Row Spacing	1	1	1	2	2	2	2	2	2	1	1	1
Specularity	0.0	1.0	0.5	0.0	1.0	0.5	0.0	1.0	0.5	0.0	1.0	0.5
Emissivity	0.0	0.0	0.5	0.0	0.0	0.5	0.0	0.0	0.5	0.0	0.0	0.5

184

Transmission of Radiation Through the Arrays

Transmission of radiation through the array is presented in two forms: the array transmission and array extinction coefficient. Array transmission is the fraction of incident radiation that passes through the array. Array extinction coefficient is defined as

$$K_e = \frac{\ln(i/i_o)}{s} \tag{5}$$

where K_e equals array extinction coefficient, i equals radiation flux transmitted through the array, i_o equals radiation flux incident in the array, and s equals apparent array width.

The array extinction coefficient includes the effect of apparent array depth on the transmission of radiation. Apparent array depth is defined as

$$s = 1/\cos\alpha \tag{6}$$

where α is the incident angle of the beam radiation impinging on the array. Results for the nine cases are summarized in Table 2 and are discussed below.

Array Transmission

In cases involving diffuse reflection, array transmission generally decreases with incident angle but the decrease is not monotonic. The specular cases show large variations in array transmission as incident angle is increased, without any clear trends.

If the arrays were being modeled as a participating medium, one would generally expect the transmission to decrease with incident angle because the apparent depth of the array increases as incident angle increases. The nonmonotonic behavior of array transmission as a function of incident angle is caused by the fixed geometric arrangement of elements in the array. When the array incident angle is 0, any radiation not impinging on an element passes through the array. As the incident angle increases, generally less radiation will pass through the array without encountering an element. However, occasionally an increasing incident angle will produce an arrangement of elements that results in a photon path that will pass through without encountering any elements. The existence and magnitude of these unobstructed optical paths through the array is the most important determining factor for array transmission. In cases 1 and 3, an incident angle of $3\pi/16$ results in an increase in the number of unobstructed optical paths through the array.

The specular cases (cases 2, 5, and 8) show more complex behavior. When specular reflection is considered, unobstructed optical paths may result from photon trajectories through the array that include specular reflections from array elements. As incident angle varies, the geometric arrangement of elements forms a number of photon paths that, while involving multiple specular reflections, result in the photon being transmitted through the array.

Case 5 illustrates the impact of specular reflection on array transmission. The diffuse case (case 4) shows a small increase in transmission when the array incident angle is increased from $3\pi/16$ to $\pi/4$, but the specular case shows a much larger increase. The increased transmission for the specular case is caused by the formation of specular reflecting photon paths through the array.

Array Extinction Coefficient

The array extinction coefficient includes the impact of apparent array depth. Ignoring scattering from array elements, the length of a photon path through the array will increase with incident angle. If the array were being modeled as an absorbing

medium, transmission should decrease with increasing photon path length, but the extinction coefficient should be constant for a homogenous medium.

Table 2 shows a significant variation in extinction coefficient as a function of array incident angle. When specular reflection is not considered and ignoring the cases with normal incident radiation (α = 0.0), variations in the extinction coefficients are as low as 48% (case 1) and as high as 75% (case 9) for the range of incident angles examined. Variations with incident array angle are also large for the specular cases where the array extinction coefficient can vary by as much as 70%. Clearly, the two array geometries cannot be assumed to be isotropic.

Results included in Table 2 show that the sparse array of square elements and cylindrical elements had the same nonmonotonic relationship between array transmission and array incident angle that was observed in the array of fin-shaped elements. Extinction coefficient values show the same magnitude of variation with incident angle for both array geometries. Contrary to expectations, the array of sparsely distributed square and cylindrical elements appears to be as strongly anisotropic as the array of fin-shaped elements.

As Howell [4] observed, when the orientation of an array is fixed, the scattering phase function for an element depends on the angle of incidence, as well as the angle of reflection. However, the results of this study suggest that the problem may be even more complicated because it appears that optical properties of an array will depend on the geometric arrangements of the elements, in addition to the scattering phase function of individual elements. The nonmonotonic relationship between array transmission and incident angle and the anisotropic extinction coefficients shows that the relative location of array elements can have a strong impact on array optical properties.

TABLE 2. Array Transmission and Extinction Coefficient

Array Incident Angle (α)	Case 1		Case 2		Case 3	
	Array Transmission (%)	Array Extinction Coefficient	Array Transmission (%)	Array Extinction Coefficient	Array Transmission (%)	Array Extinction Coefficient
0.0	62.6	-0.4687	60.0	-0.5100	60.0	-0.5100
$\pi/16$	25.9	-1.326	31.6	-1.130	9.3	-2.326
$\pi/8$	24.5	-1.298	20.0	-1.487	5.6	-2.671
$3\pi/16$	43.7	-0.688	47.3	-0.6229	23.0	-0.923
$\pi/4$	19.6	-1.151	20.0	-1.138	1.4	-3.025
$3\pi/8$	13.8	-0.7580	78.2	-0.0939	0.9	-1.763

	Case 4		Case 5		Case 6	
0.0	61.4	-0.4863	60.0	-0.5100	60.0	-0.5100
$\pi/16$	14.8	-1.874	0.6	-4.987	0.5	-5.238
$\pi/8$	14.2	-1.805	19.5	-1.511	0.6	-4.701
$3\pi/16$	23.1	-1.217	52.6	-0.5349	1.7	-3.370
$\pi/4$	29.6	-0.8609	80.0	-.1578	2.3	-2.655
$3\pi/8$	15.5	-0.7137	9.5	-0.9007	0.8	-1.848

	Case 7		Case 8		Case 9	
0.0	62.8	-0.465	66.4	-0.409	60.5	-0.503
$\pi/16$	19.6	-1.598	36.8	-0.980	2.4	-3.658
$\pi/8$	25.6	-1.259	26.4	-1.230	13.0	-1.885
$3\pi/16$	27.2	-1.082	35.2	-0.868	3.3	-2.836
$\pi/4$	37.8	-0.688	58.1	-0.384	9.3	-1.680
$3\pi/8$	26.4	-0.510	38.3	-0.367	9.4	-0.905

CONCLUSIONS

Radiation heat transfer in arrays of fixed discrete surfaces is a poorly understood phenomenon encountered in several important engineering applications. As part of a larger study to investigate radiation heat transfer in arrays of discrete surfaces, a Monte Carlo model using cell-to-cell photon transport was used to conduct parametric studies on three arrays. The results of the parametric evaluations showed that array transmission generally decreases with incident angle but the decrease is not monotonic and significant variation in extinction coefficient will occur as a function of array incidence angle. Optical properties of arrays will depend on the geometric arrangements of the elements in addition to the scattering phase function of an individual element. Assuming the arrays are isotropic will likely result in significant error.

REFERENCES

1. DROST, M. K., R. G. CAVOLA, D. R. BROWN, D. E. DEBELLIS and B. M. JOHNSON, "Analysis and Design of the Volumetric Air Heating Receiver," SAND 84-8190, Prepared for Sandia National Laboratories, Albuquerque, New Mexico, by Pacific Northwest Laboratory, Richland, Washington (1985).

2. LEE, S. C., "Radiation Heat Transfer Model for Fibers Oriented Parallel to Diffuse Boundaries," *J. of Thermophysics* 2(4), 161-174 (1988).

3. TONG, T. W. and C. L. TIEN, "Radiative Heat Transfer in Fibrous Insulation - Part 1: Analytical Study," *J. of Heat Transfer* 105, 70-75 (1983).

4. HOWELL, J. R. "Thermal Radiation in Participating Media: The Past, The Present, and Some Future Possibilities," *J. of Heat Transfer* 110, 1220-1230 (1988).

5. DROST, M. K. and J. R. WELTY, "Monte Carlo Simulation of Radiation Heat Transfer in Arrays of Fixed Discrete Surfaces using Cell-to-Cell Photon Transport," *Developments in Radiative Heat Transfer*, HTD-Vol. 203, American Society of Mechanical Engineers, New York (1992).

6. HOWELL, J. R. "Monte Carlo Applications in Heat Transfer," *Advances in Heat Transfer* 5, 2-54 (1968).

7. HAJI-SHEIKH, A., "Monte Carlo Methods," *Handbook of Numerical Heat Transfer*, Wiley Interscience, New York (1988).

8. MALTBY, J. D. and P. J. BURNS, "Performance, Accuracy, and Convergence in a Three-Dimensional Monte Carlo Radiative Heat Transfer Simulation," *Numerical Heat Transfer* 19, 191-209 (1991).

Nonimaging Reflectors as Functionals of the Desired Irradiance

Roland Winston and Harald Ries[1]

The University of Chicago, The Enrico Fermi Institute & Department of Physics
Chicago, Illinois 60637

Abstract

For many tasks in illumination and collection the acceptance angle is required to vary along the reflector. If the acceptance angle function is known, then the reflector profile can be calculated as a functional of it. The total flux seen by an observer from a source of uniform brightness (radiance) is proportional to the sum of the view factor of the source and its reflection. This allows one to calculate the acceptance angle function necessary to produce a certain flux distribution and thereby construct the reflector profile. We demonstrate the method for several examples, including finite size sources with reflectors directly joining the source.

1   Introduction

Nonimaging optics was developed to solve a well posed but narrow set of problems [1]. A prototypical example is the concentration of a light beam with divergence half-angle θ and cross-sectional area A_1 into the minimum possible area A_2 without loss of throughput or conversely, the design of illumination systems that convert a lambertian source into a beam with divergence half-angle θ and no stray light without loss of throughput. Two classes of algorithms have been found which solve these problems exactly or nearly so. These are summarized here; the details can be found in Ref. [2]. The first is the "string" or "edge-ray" method. The "Hottel string" is a useful concept for calculating radiative transfer between lambertian surfaces [3]. It may be succinctly characterized as: $\int n\,dl = constant$ along a string, where n denotes the index of refraction and dl the path length. Notice that replacing "string" by "ray" gives all of imaging optics. The second class of algorithms places reflectors along the lines of flow of a radiation field set up by a radiating source. In cases of high symmetry such as a sphere or disc, one obtains ideal solutions in both two and three dimensions. In either case, reflecting and sometimes refracting elements are shaped in specific ways in combination to solve the problem.

A wider class of problems can not be solved by the known methods. Here are a few examples:

---

[1]Permanent address: Paul Scherrer Institute, CH-5232 Villigen, Switzerland

It is well-known that the irradiance on a distant plane at an angle θ from a long, cylindrical lambertian source of uniform brightness falls off with $\cos^2(\theta)$. Strip radiators and spherical sources produce a $\cos^3(\theta)$ irradiance on a distant plane, while circular disc radiators produce an irradiance proportional to $\cos^4(\theta)$. The angular power density of the flat sources (disc and strip) falls off as $\cos(\theta)$ while the power density of cylindrical and spherical sources is constant. But suppose one desires a predetermined far-field power or irradiance pattern e.g. uniform irradiance? The classical designs will not suffice; they simply transform a lambertian source radiating over 2π into a lambertian source radiating over a restricted angular range.

The limitation of the old designs is that they are too static and depend only on a few parameters, such as the area of the beam A_1 and the divergence angle θ. One needs to introduce additional degrees of freedom into the nonimaging designs to solve a wider class of problems. The purpose of this communication is to indicate the lines along which this additional freedom can be introduced.

2   Determining the reflector profile for small sources

In the usual design methods the profile of the reflector is determined by the given constant acceptance angle θ and the geometry of the entrance and exit surfaces. Thus we can regard the reflector profile R as a function of θ, $R(\theta)$. However, in certain situations a "constant acceptance angle" design is unduly restrictive. But suppose θ is itself made a function of some other parameter of the problem say, ϕ. Then R is determined only after the functional relationship of θ and ϕ is known i.e., R is now a *functional* of θ, $R = R\{\theta\}$.

For illustrative and pedagogical reasons, we will consider first the simple case when the size of the source is much less than the closest distance of approach R_0 to any reflective or refractive component. Thus the angle subtended by the source at any reflective or refractive component may be regarded as small. Our approximation of small source dimension d and large observer distance D amounts to

$$d << R_0 << D. \tag{1}$$

In this limit the illumination problem has been solved earlier [4] We briefly review the classical solution before we introduce a novel approach capable of deriving in closed form the reflector for large sources.

Polar coordinates are used to represent the reflector profile by $R = R(\phi)$, with the source at the origin. The angle of the reflected ray with the optical axis is denoted by θ, and the incidence angle at the reflector with respect to its normal is denoted by α as depicted in Fig.1. The geometry shows that the following relation between the reflector profile and incidence angle holds:

$$\frac{d\log(R)}{d\phi} = \tan(\alpha). \tag{2}$$

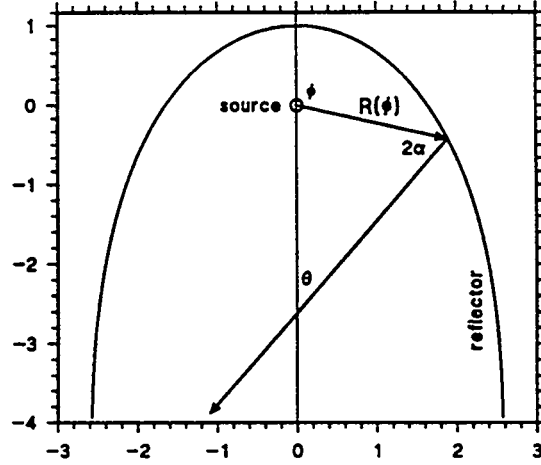Note, that the underlying assumption for this equation is, that the edge rays incident onto

Figure 1: The reflector profile is represented in polar coordinates $R(\phi)$ with the source at the origin. The reflected radiation has an angle θ with the optical axis y and α with the normal to the reflector.

the reflector travel along the vector R. Clearly,

$$\alpha = \frac{\phi - \theta}{2}. \tag{3}$$

Equation 2 is readily integrated,

$$\log\left(\frac{R(\phi)}{R_0}\right) = \int_0^{\alpha(\phi)} \tan(\alpha(\phi))d\phi \tag{4}$$

so that,

$$R(\phi) = R_0 \exp\left(\int_0^{\alpha(\phi)} \tan(\alpha(\phi))d\phi\right). \tag{5}$$

This determines the reflector profile $R(\phi)$ for any desired acceptance angle function $\theta(\phi)$.

Suppose we wish to radiate power with a particular angular distribution $P^o(\theta)$ from a source which itself radiates with a power distribution $P^s(\phi)$. The angular characteristic of the source is the combined result of its shape, surface brightness, and surface angular emissivity at each point. A distant observer viewing the source fitted with the reflector under an angle θ will see a reflected image of the source in addition to the source itself. This image will be magnified by some factor $|M|$ if the reflector is curved. Ideally both the source and its reflected image have the same brightness, so the power each produces is proportional to the apparent size. The intensity perceived by the observer, $P^o(\theta)$ will be the sum of the two

$$P^o(\theta) = P^s(\theta) + |M|P^s(\phi). \tag{6}$$

The absolute value of the magnification has to be taken because, if the reflected image and the source are on different sides of the reflector and we therefore perceive the image as reversed or upside down, then the magnification is negative. Actually, at small angles, the

source and its reflection image may be aligned so that the observer perceives only the larger of the two. But if $|M|$ is large one can neglect the direct radiation from the source.

Thus one is concerned with the magnification of the reflector. A distant observer will see a thin source placed in the axis of a trough reflector magnified in width by a factor

$$M_m = \frac{d\phi}{d\theta}. \tag{7}$$

This can be proved from energy conservation. The power emitted by the source must be conserved upon reflection: $P^s d\phi = M P^s d\theta$.

For a rotationally symmetric reflector the magnification M_m as given in Eq.(7) refers to the meridional direction. In the sagittal direction the magnification is

$$M_s = \frac{d\mu_1}{d\mu_2} = \frac{\sin(\phi)}{\sin(\theta)}, \tag{8}$$

where now μ_1 and μ_2 are small angles in the sagittal plane, perpendicular to the cross section shown in Fig 1. Equation (8) can be easily verified by noting that the sagittal image of an object on the optical axis must also lie on the optical axis. The reason is, that because of symmetry, all reflected rays must be coplanar with the optical axis.

The total magnification M_t is the product of the sagittal and the meridional magnification

$$M_t = M_s M_m = \frac{d\cos(\phi)}{d\cos(\theta)}. \tag{9}$$

Actually Eq.(9) could also have been derived directly from energy conservation by noting that the differential solid angle is proportional to $d\cos(\theta)$ and $d\cos(\phi)$ respectively.

Thus inserting the magnification given in Eq.(9) or Eq.(7), as the case may be, into Eq.(6) yields the relationship between θ and ϕ which produces a desired power distribution $P^o(\theta)$ for a given angular power distribution of the source P^s. This relationship then can be integrated as outlined in Eq.5 to construct the shape of the reflector which solves that particular problem.

There are two qualitatively different solutions depending on whether we assume the magnification to be positive or negative. If $M_m > 0$ this leads to CEC-type devices, whereas $M_m < 0$ leads to CHC-type devices. The term CEC refers to Compound Elliptical Concentrator and CHC to the so called Compound Hyperbolic Concentrator [5, 6, 7, 8].

Now the question arises of how long we can extend the reflector or over what angular range we can specify the power distribution. From Eq.(5) one can see that if $\phi - \theta = \pi$ then R diverges. In the case of negative magnification this happens when the total power seen by the observer between $\theta = 0$ and $\theta = \theta^{max}$ approaches the total power radiated by the source between $\phi = 0$ and $\phi = \pi$. A similar limit applies to the opposite side and specifies θ^{min}. The reflector asymptotically approaches an infinite cone or V-trough. There is no power radiated or reflected outside the range $\theta^{min} < \theta < \theta^{max}$.

For positive magnification the reflected image is on the opposite side of the symmetry axis (plane) to the observer. In this case the limit of the reflector is reached as the reflector on the side of the observer starts to block the source and its reflection image. For symmetric devices this happens when $\phi + \theta = \pi$. In this case too one can show that the limit is actually imposed by the first law. However, the reflector remains finite in this limit. It always ends with a vertical tangent. For symmetric devices where $\theta^{max} = -\theta^{min}$ and $\phi^{max} = -\phi^{min}$ the extreme directions for both the CEC-type and the CHC-type solution are related by

$$\phi^{max} + \theta^{max} = \pi. \tag{10}$$

In general CEC-type devices tend to be more compact. The mirror area needed to reflect a certain beam of light is proportional to $1/\cos(\alpha)$. The functional dependence of θ and ϕ for symmetrical problems is similar except that they have opposite signs for CHC-type devices and equal signs for CEC-type solutions. Therefore α increases much more rapidly for the CHC-type solution which therefore requires a larger reflector, assuming the same initial value R_0.

3 Reflector adjacent to a finite planar source

We have now developed the analytical tools to solve the real problems which involve reflectors close to the source. We do this by combining the above technique with the edge ray method which has proved so effective in nonimaging designs [2]. That is, we apply the above methods to edge rays. As a first example, we design a reflector for a planar, lambertian strip source so as to achieve a predetermined far-field irradiance. We design the reflector so that the reflected image is immediately adjacent to the source. This is only possible in a negative magnification arrangement. Then the combination of source and its mirror image is bounded by two edge rays as indicated in Fig.2. The combined angular power density for a source of unit brightness radiated into a certain direction is given by the edge ray separation

$$R\sin(2\alpha) = P^o(\theta). \tag{11}$$

By taking the logarithmic derivative of Eq.(11) and substituting Eq.(2) we obtain

$$\frac{d\alpha}{d\theta} = \frac{\sin(2\alpha)}{2} \frac{d\log(P^o(\theta))}{d\theta} - \sin^2(\alpha). \tag{12}$$

This describes the right hand side, where $\theta < 0$. The other side is the mirror image.

3.1 Deriving the reflector shape directly for a finite source

For $2\alpha = \pi$, R diverges just as in the case of the CHC-type solutions for small sources. Thus in general the full reflector extends to infinity. For practical reasons it will have to
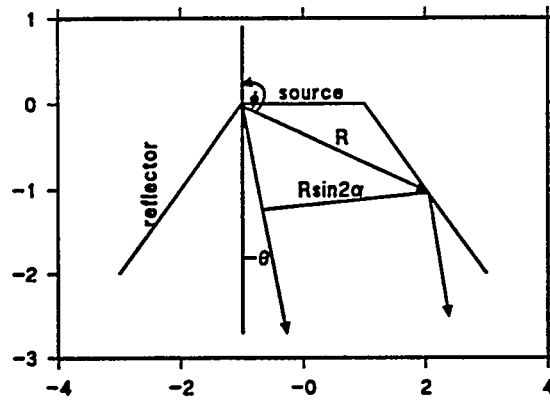
Figure 2: The reflector is designed to produce a reflected image adjacent to the source. The combined intensity radiated in the direction $-\theta$ is determined by the separation of the two edge rays: $R\sin 2\alpha$.

be truncated. Let's assume that the reflector is truncated at a point T from which the edge ray is reflected into the direction θ_T. For angles θ in between $\pm\theta_T$ the truncation has no effect because the outer parts of the reflector do not contribute radiation in that range. Therefore within this range the truncated reflector also produces strictly the desired illumination. Outside this range the combination of source plus reflector behaves like a flat source bounded by the point T and the opposite edge of the source. Its angular power density is given by Eq.(11) with $R = R_T = constant$. The total power P_T radiated beyond θ_T is thus

$$P_T = R(\theta_T)\int_{2\alpha_T}^{\pi} \sin\gamma d\gamma = R(\theta_T)(1 + \cos(2\alpha_T)). \tag{13}$$

In order to produce an intensity $P^o(\theta_T)$ at θ_T, $R(\theta_T)$ must be

$$R(\theta_T) = \frac{P^o(\theta_T)}{\sin(2\alpha_T)}. \tag{14}$$

The conservation of total energy implies that the truncated reflector radiates the same total power beyond θ_T as does the untruncated reflector.

$$\frac{1 + \cos(2\alpha_T)}{\sin(2\alpha_T)} = \frac{1}{P^o(\theta_T)}\int_{\theta_{max}}^{\theta_T} P^o(\psi)d\psi = B(\theta_T) \tag{15}$$

This equation must hold true for any truncation $\theta = \theta_T$. It allows us to explicitly calculate α, and with it ϕ and R, in closed form as functions of θ, if $B(\theta)$, that is the integral of $P^o(\theta)$ is given in closed form. The conservation of total energy also implies that the untruncated reflector radiates the same total power as the bare source. This leads to the normalizing condition

$$B(0) = \frac{1}{P^o(0)}\int_{\theta_{max}}^{0} P^o(\psi)d\psi = 1. \tag{16}$$

This condition may be used to find θ^{max}; it is equivalent to setting $\theta^T = 0$, $2\alpha_T = \pi/2$ in Eq.(15). Solving Eq.(15) for α yields

$$2\alpha = \arccos\left(\frac{B^2 - 1}{B^2 + 1}\right).$$ (17)

Substituting Eq.(3) yields the acceptance angle function

$$\phi(\theta) = \theta + 2\alpha.$$ (18)

From Eq.(11) the radius is given by

$$R(\theta) = P^o(\theta)\frac{B^2 + 1}{2B}.$$ (19)

These equations specify the shape of the reflector in a parametric polar representation for any desired angular power distribution $P^o(\theta)$. A straight forward calculation shows that Eq.(17) is indeed the solution of the differential equation (12). In fact Eq.(12) was not needed for this derivation of the reflector shape. We have presented it only to show the consistency of the approach.

3.2 Example - constant irradiance

For example to produce a constant irradiance on a plane parallel to the source we must have $P^o(\theta) = 1/\cos^2(\theta)$ and thus $B(\theta) = \cos^2(\theta)(\tan(\theta) - \tan(\theta_{max}))$. Using Eq.(16), we find $\theta_{max} = -\pi/4$, so that $B(\theta) = \cos^2(\theta)(\tan(\theta) + 1)$ with no undetermined constants. The resulting acceptance angle function and the reflector profile are shown in Fig.3 and Fig.4 respectively. The reflector shape is close to a V-trough. Though, the acceptance angle function is only poorly approximated by a straight line, which characterizes the V-trough. In Fig.5 we show the deviation of the reflector shape depicted in Fig.4. from a true V-trough. Note, that a true V-trough produces a markedly non-constant irradiance distribution proportional to $\cos(\theta + \pi/4)\cos(\theta)$ for $0 < -\theta < \pi/4$.

4 Conclusions

The classical nonimaging reflector shapes can be viewed as functions of an acceptance angle which is constant along the reflector profile. A variety of problems, however, require variable acceptance angles. In these cases the reflector profile is a functional of the acceptance angle function or the function describing the desired power density distribution. For the calculation of the reflector based on the variable magnification there are in general two different types of solution, depending on whether the meridional magnification is positive or negative: a CEC-type, characterized by positive magnification in which the reflection of the source appears
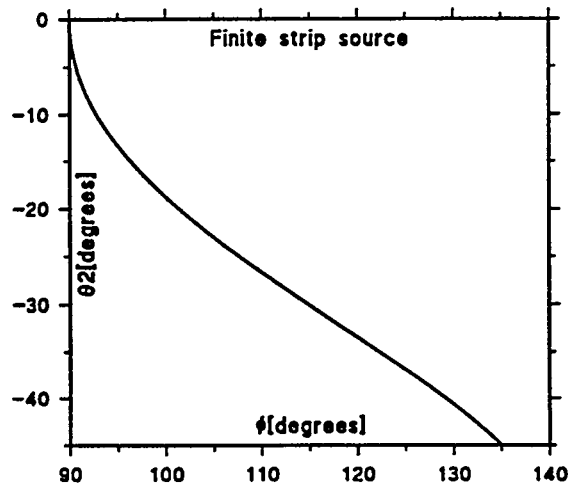
Figure 3: Acceptance angle function which produces a constant irradiance on a distant plane from a finite one-sided lambertian strip source. There is only a CHC-type solution.
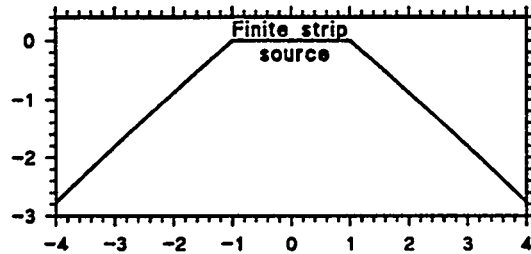

Figure 4: The reflector profile which produces a constant irradiance on a distant plane from a finite one-sided lambertian strip source of width two units. Note that there is only a CHC-type solution and it is truncated.
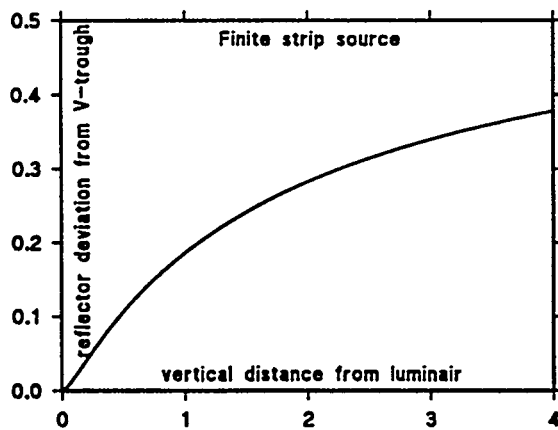

Figure 5: Deviation of the reflector depicted in Fig.4 from a true V-trough.

on the side opposite to the observer, and a CHC-type, of negative magnification, where the reflection is on the same side. The CEC-type reflector is finite and always ends with a vertical tangent, while the CHC-type solution is infinite and approaches a constant slope. The end point of the CEC-type solution and the asymptotic slope of the CHC-type reflect the conservation of total radiant power.

For a finite size source, we have shown how to calculate a CHC-type reflector profile touching the source. For a flat source the solution can be given in closed form. The method presented here does not entail in any way an optimization procedure. It yields the reflector profile which produces a desired irradiance distribution from a given source by straightforward calculation based on first principles.

References

[1] R. Winston. "Nonimaging optics," Scientific American, 264(3):76–81,(March 1991).

[2] W. T. Welford and R. Winston. High Collection Non-Imaging Optics, (Academic Press, New York, 1989), Chap. 3.

[3] Hoyt C. Hottel, chapter 4 in Heat Transmission, W. H. McAdams. Heat Transmission, (McGraw-Hill, New York, 1954), Chap. 3.

[4] William B. Elmer. The Optical Design of Reflectors, 2nd ed. (John Wiley & Sons, New York, 1980), Chap. 4.4.

[5] R. Winston. "Cone collectors for finite sources," Appl. Opt., 17:688–1689, (1978).

[6] M. Collares-Pereira, A. Rabl, and R. Winston. "Lens-mirror combinations with maximal concentration," Applied Optics, 16(10):2677–2683 (1977).

[7] Ari Rabl and Roland Winston. "Ideal concentrators for finite sources and restricted exit angles," Applied Optics, 15(11):2880–2883 (1976).

[8] J. M. Gordon and A. Rabl. Nonimaging CPC-type reflectors with variable extreme directions. *to be published in Appl. Optics*, 1993.

[9] J. M. Gordon and H. Ries. "Tailored edge-ray concentrators (TERC's) as ideal second stages for Fresnel reflectors," to be published in Appl. Optics.

[10] R. Winston. "Nonimaging optics: optical design at the thermodynamic limit," in Proceedings of SPIE, Roland Winston and Robert L. Holman, ed. (SPIE, Bellingham, Washington, 1991) 1528, pp. 2–6.

MICROSCOPIC IMAGE PROCESSING SYSTEM FOR MEASURING NONUNIFORM FILM THICKNESS PROFILES: IMAGE SCANNING ELLIPSOMETRY

An-Hong Liu, Joel L. Plawsky, and Peter C. Wayner, Jr.

The Isermann Department of Chemical Engineering
Rensselaer Polytechnic Institute
Troy, New York 12180-3590

ABSTRACT

The long-term objective of this research program is to determine the stability and heat transfer characteristics of evaporating thin films. The current objective is to develop and use a microscopic image-processing system (IPS) which has two parts: an image analyzing interferometer (IAI) and an image scanning ellipsometer (ISE). The primary purpose of this paper is to present the basic concept of ISE, which is a novel technique to measure the two dimensional thickness profile of a non-uniform, thin film, from several nm up to several μm, in a steady state as well as in a transient state. It is a full-field imaging technique which can study every point on the surface simultaneously with high spatial resolution and thickness sensitivity, i.e., it can measure and map the 2-D film thickness profile. The ISE was tested by measuring the thickness profile and the refractive index of a nonuniform solid film.

I. INTRODUCTION

The effects of interfacial stress (which is a function of **film shape** and interfacial intermolecular forces) and temperature on the stability and dynamics of nonisothermal thin liquid films have been extensively studied because of their generic importance to multiphase flow technology. See, for example, the extensive review of the literature on the effects of interfacial forces on the dynamics and stability of thin evaporating liquid films on heated surfaces by Bankoff [1]. In these small thin film systems, the complex microscopic details of fluid flow and film shape are of paramount importance to the change-of-phase heat transfer process [2]. Needless to say, many experimental studies have been reported in the literature. For example, in a companion paper to the theoretical paper on thermocapillary flow by Tan et al. [3], Burelbach et al. [4] experimentally studied thermocapillary flow in a thin liquid layer. The electrical impedance measurement of the film thickness was accurate to 1 μm. In small nonisothermal systems, the interfacial

intermolecular force field controls fluid flow and change of phase heat transfer. This was discussed by Wayner et al. [2,5] who used classical change-of-phase kinetics and interfacial concepts like the Kelvin, Young-Dupré, and augmented Young-Laplace equations to evaluate and compare stress (shape) and thermal effects. These results demonstrate the central importance of the augmented Young-Laplace equation to the understanding of the dynamics of both completely wetting and partially wetting thin liquid films. Experimental confirmation of the central importance of the augmented Young-Laplace to describing the stress field in thin liquid films was obtained using the image analyzing interferometer, IAI [e.g., 5]. However, these and other recent results demonstrate that more powerful and convenient microscopic experimental techniques are needed to decrease the lag in the development of evaluative experimental techniques. Thinner and smaller dynamic systems need to be studied at higher magnification. For this purpose, a new experimental technique, ISE, which uniquely combines ellipsometry, image processing, and a specific algorithm, has been developed and is described herein.

If the physical properties of the evaporating liquid films are known, the film thickness profile, measured experimentally, can be used to calculate the heat transfer characteristics of thin liquid films. Therefore, one of the major experimental objectives of thin film heat transfer research is to determine the film thickness profiles as a function of the experimentally varied evaporation rate. In order to experimentally measure the film thickness profile of an evaporating, non-uniform thin film, the following equipment characteristics are required: (1) The instrument should be able to measure non-uniform films as well as uniform films from several nm up to several μm in thickness; (2) The instrument should be able to measure the thickness profile in the transient state as well as in the steady state; (3) The instrument should be able to measure every point on the liquid surface simultaneously instead of an average value over the measured surface. Many different optical and non-optical techniques have been developed to measure film thickness profiles. However, none of these techniques had all the required characteristics mentioned above. One disadvantage of non-optical methods is that they can disturb the films during measurement. The optical methods based on interferometry, in general, can measure non-uniform films but cannot accurately measure film thicknesses under 1000 Å nor are they appropriate for uniform films. Image Analyzing Interferometry (IAI) [5] is a new technique based on interferometry which was developed to measure non-uniform film thickness profiles. IAI not only has very good thickness sensitivity and lateral resolution but can also be used to study every point on a surface simultaneously by using image processing technology and a low-light-level CCD camera. However, IAI is not well suited for transient state studies because it uses a standard, time consuming, null ellipsometer, to extrapolate the film thickness beyond the first dark fringe. The optical methods based on standard ellipsometry, in general, can measure uniform film thicknesses from 1 Å up to several μm but not spatially varying film thicknesses. They are also not suitable for transient state studies. Dynamic Imaging Microellipsometry (DIM) [6] is the only new technique based on ellipsometry developed to measure a film thickness profile in a transient state. However, with DIM, the optimal settings of the ellipsometric components change with the film thickness and so accurate measurements over wide thickness ranges are difficult. Due to this complication, DIM is basically restricted to the measurement of more uniform films with thickness variations within certain, narrow ranges, but not for thickness profiles ranging from several nm up to several μm.

II. THEORY AND DESIGN OF ISE

ISE is a new optical technique based on null ellipsometry for studying non-uniform film thickness profiles in the transient state as well as in the steady state. It is a full-field imaging technique which can simultaneously study every point on the surface with high spatial resolution and great thickness sensitivity. Moreover, ISE uniquely results in a 2-D mapping of the film thickness profile. The theoretical development of this approach is based on the null ellipsometer. The measurements of null ellipsometry are quite routine, involving the rotation of a polarizer and an analyzer to cause extinction of a beam of polarized light reflected from the surface of the sample. The extinction point is called the null point. At the null point the values of the measured azimuths of the polarizer (P), the analyzer (A), and the compensator (C), measured from the plane of incidence, are recorded. All these angles are measured positive counter-clockwise from the plane of incidence when looking into the light beam.

The relative phase, Δ, and relative amplitude, Ψ, of the two orthogonal electric field components of the polarized light can be determined from the measured angles of P, A, and C using the standard equation for ellipsometry:

$$\rho = Tan\ (\Psi) \times Exp\ (i\ \Delta) \tag{1}$$

where i is $(-1)^{0.5}$, ρ is the ellipticity, the ratio of reflection coefficients of parallel components over perpendicular components, Tan (Ψ) is the ratio of the amplitude of reflection coefficients of parallel components over perpendicular components, and   is the phase shift between the parallel and perpendicular components. The values of Ψ and Δ can then be used to calculate the refractive index of the substrate or the film thickness and film refractive index. Due to multiple reflections of light across the film-vapor and the substrate-film interfaces, the measured values of Ψ and Δ exhibit an interference effect. In other words, Ψ and Δ are cyclic functions of the film thickness. The cyclic behavior is governed by

$$\delta = \lambda/2\ [n_F^2 - n_m^2\ Sin^2\ (\Phi_1)]^{0.5} \tag{2}$$

where λ is the wavelength of the light source, n_F is the refractive index of the film, where n_m is the refractive index of medium and Φ_1 is the angle of incidence. When the measured thin film is non-uniform, rotating the polarizer and analyzer can only partly extinguish the beam of polarized light reflected from the surface. The image appears as a set of destructive fringes representing various film thicknesses. In Fig. (1), the locations of the destructive fringes are presented as a function of film thickness and polarizer setting for A=0.00 and C=45.00. Combining this null ellipsometer with an image processing system, a long-working-distance microscope, and a low-light-level CCD camera with manual gain control, forms a system capable of easily measuring the thickness profile of a non-uniform film. By fixing the analyzer and compensator settings and rotating the polarizer, the ellipsometric null points, which have a minimum reflectivity, can be observed to sweep across the whole measuring area. Based on a knowledge of the pixel intensity and magnification of the system, the exact position of the null points can be determined. Using a series of ellipsometric images the film thickness profile from several nm up to several μm can be calculated. This thickness profile includes the thin film region, under 1000 Å, that the IAI cannot measure. The measurement process varies the polarizer setting, recording an ellipsometric image for each point. The more settings we use on the
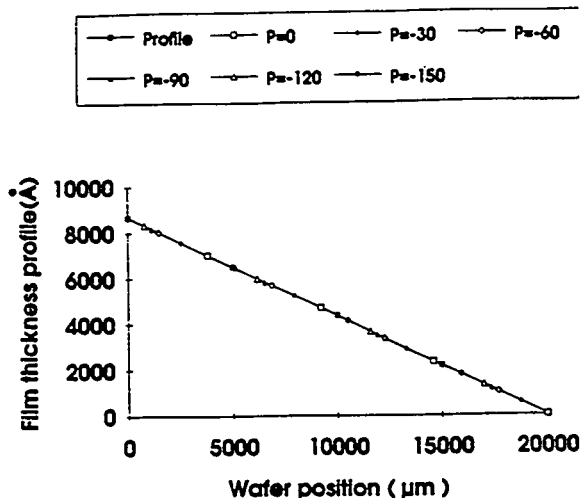
Figure 1. Calculated film thickness at the null point versus position for various polarizer settings. System was a particular ThF_4 solid wedge deposited on a Si wafer.
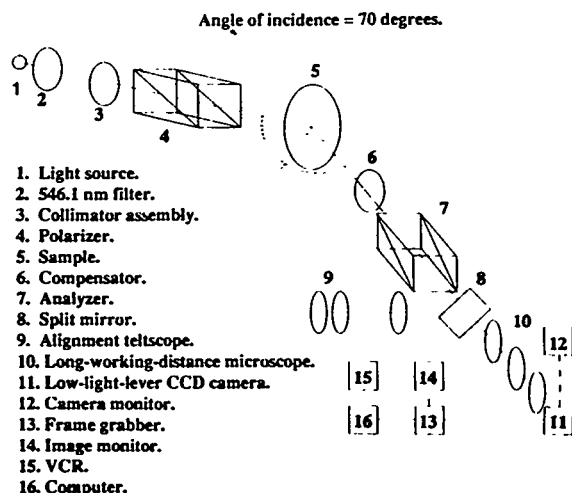

Angle of incidence = 70 degrees.

1. Light source.
2. 546.1 nm filter.
3. Collimator assembly.
4. Polarizer.
5. Sample.
6. Compensator.
7. Analyzer.
8. Split mirror.
9. Alignment teltscope.
10. Long-working-distance microscope.
11. Low-light-lever CCD camera.
12. Camera monitor.
13. Frame grabber.
14. Image monitor.
15. VCR.
16. Computer.

Figure 2. A schematic sketch of the Image Scanning Ellipsometer.

polarizer, the more points we have in the film thickness profile, i.e., the more detailed our measurements will be. The image processing system enables us to study the transient state phenomena and to find all the null points in the measured area. We can then construct 2-D contour maps to describe the non-uniform film thickness profiles.

The ISE measures the profile only using the null points instead of the intensity itself. By considering only reflectivity minima, there will be little or no interference from imperfections in the optical components, instability of the light source, sensitivity variations of the camera, or the presence of dust particles, finger prints, and other contaminants in the optical path. The accuracy and spatial resolution of ISE depends on the resolution of the imaging microscope and the slope of the thin film profile.

III. EXPERIMENTAL DESIGN

ISE includes the following major components which are organized schematically in Fig. (2): a null ellipsometer, step motor driver and step motor, long-working-distance (LWD) microscope, low-light-level(LLL) CCD camera with manual gain control, PC compatible computer, Frame grabber with 4 MB onboard memory, and Frame coprocessor for accelerating image processing.

Our ISE was constructed using a standard, manually-operated, null ellipsometer, with vertical sample holder, manufactured by Rudolph and Sons, Inc. in 1970's. In order to monitor transient liquid films in situ from the TV screen, magnification of the light spot

after the analyzer is needed. The minimum distance between the analyzer and surfaces of the samples is 22" in this system and so an ordinary microscope could not be used. A K2-single port LWD microscope from Infinity Photo-Optical Company was used because the working distance of this instrument is 12" to 96". The actual magnification also depends on the distance between the eyepiece and the camera. Ideally the longer this distance, the higher the magnification. Unfortunately, the resolution decreases dramatically as the distance increases due to an overall decrease in the intensity of the images projected onto the camera. The best spatial resolution in our system was found to be 2 μm (vertical) x 7.5 μm (horizontal). The actual film thickness resolution depends on the nature of the film measured.

The intensity and contrast of the ellipsometric image decreases sharply as the film thickness increases. This problem is especially acute for film thicknesses beyond 1 μm. To achieve the highest spatial and film thickness resolution, a high resolution, low-light-level, CCD camera was used in our system. This camera had wide dynamic range, 52 dB, and manual gain control. Adjustable gain is important to control image intensity and contrast as the liquid films drain. The dark current of the camera must also be adjustable to insure accurate detection of the null point. If the dark current is set too low, the intensity minima may be buried below the resolution of the frame grabber/digitizer and accurate null point locations cannot be found.

A computer controlled step motor was used to rotate the polarizer. The rotation was synchronized with the frame grabber so that images were captured at known polarizer settings. Using only the frame grabber's storage capability, a complete film thickness profile, composed of 15 separate images could be obtained in 3 sec. Using a VCR to store the images decreased our capture time to 1.5 sec and increased the number of images to 45. The current speed of our system is limited by the frame processing speed of the frame grabber and camera system and the sheer mass of the ellipsometer components we are using. Significant improvements are possible in those two areas.

To test the ISE, a special custom wedge, ThF_4 on Si wafer substrate, was obtained. The film thickness changed linearly from 0 nm up to 870 nm within a distance of 20 mm. The thickness profile of this wafer was measured by fixing the compensator at 45.00, the analyzer at 0.00, and then varying the polarizer angles. The destructive fringes (minimum pixel value) were thereby moved across the surface. The images of the reflection patterns and therefore the location of the null points were captured and digitized into 480 (vertical) x 512 (horizontal) space pixels and assigned to 256 possible gray values representing an intensity from 0 (black) to 255 (white). In order to reduce the data processing time and the memory needed, non-uniform interval settings on the polarizer were used, 360, 350, 340, 330, 320, 310, 285, 260, 235, 210, and 185. These choices were selected because the relationship between polarizer angle and film thickness is non-linear (See Fig. 3). The choice of the best angles depends on the optical properties of substrate, the film, and the characteristics of the thin film profile. Although the choice of the polarizer angle does not make too much difference for a profile with a constant or nearly constant gradient such as a wedge profile, the choice of the polarizer angles will affect the sensitivity and accuracy of the measurements for a large, variable, gradient such as a draining liquid film. The rule of thumb is to use as many null points as possible and make the null points as equally spaced as possible within the first thickness cycle. This means that polarizer angles should be concentrated in regions I and III of Fig. 3. Beyond the first cycle, the null points are spaced closer to one another because of the increase of the film thickness gradient.
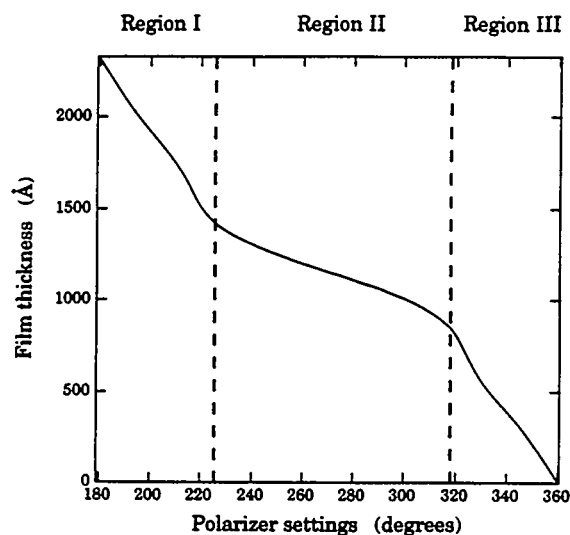
201

Figure 3. Calculated film thickness at the null point versus polarizer settings.
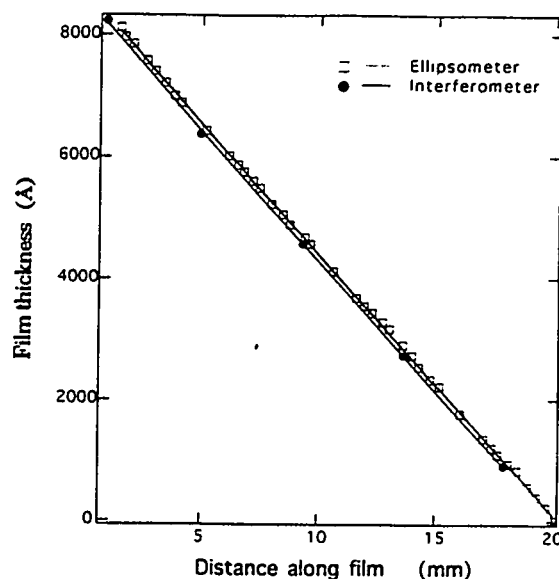

Figure 4. Experimentally measured film thickness profiles.

IV. RESULTS

To demonstrate the capability and accuracy of the ISE, the 2-D thickness profile of a non-uniform solid film of ThF_4 on a Si substrate was measured and compared with the profiles obtained by us using interferometry and measured by the manufacturer of the films (Reynard Company). The measured wedge profiles obtained from each method discussed above were analyzed using a regression program and the results are listed below:

From the Reynard company:

Standard wafer #1: TH (Å) = -0.432 ($\text{Å}/\mu m$) * X(μm) + 8661.1(Å)

From the interferometer:

Standard wafer #1: TH (Å) = -0.426($\text{Å}/\mu m$) * X(μm) + 8532.0(Å)

The measured results obtained using our interferometer are almost the same as those reported by the manufacturer. Therefore, it is certain that the measured film thickness profiles on the standard wafers are correct. By the layout of the colored bands on the standard wafers the film thickness profiles can also be estimated by eye and used to verify our other measurements. A correction of the raw ISE data is required in the horizontal direction, because the imaging system is not oriented perpendicular to the substrate. This results in a non-uniform magnification in the horizontal direction. The vertical direction requires no corrections and the magnification there is uniform across the substrate. The 1-D film thickness profile measured by ISE and our interferometer is
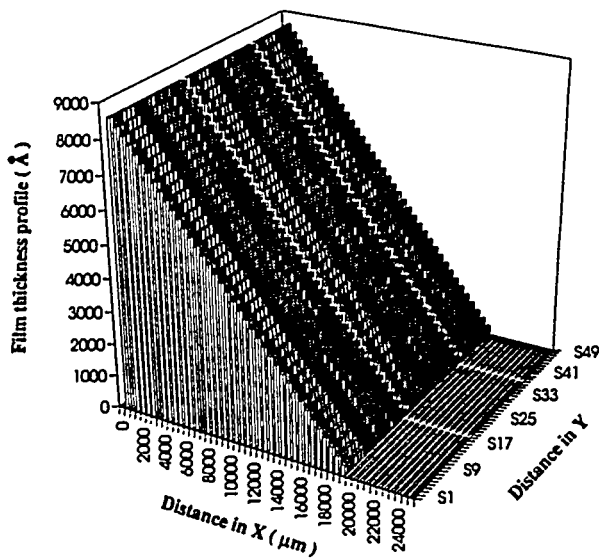
Figure 5. The 2-D film thickness profile of the standard wedge wafer # 1 measured by Image Scanning Ellipsometer.
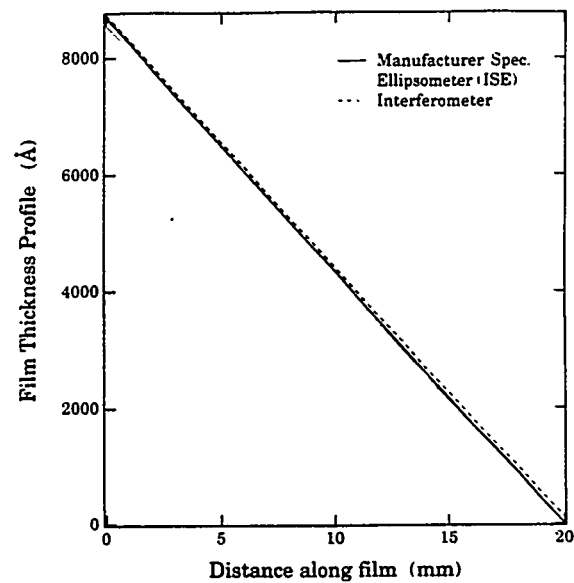
Figure 6. The comparison among different methods for standard wafer # 1, where the measured results from Reynard and the interferometer are overlaid.

presented in Fig. 4. The 2-D film thickness profile measured by ISE after correction is shown in Fig. 5. The regression results from ISE after correction are listed below:

From ISE :

Standard wafer #1:   TH (Å) = -0.429(Å/μm) * X(μm) + 8708.7(Å)

Comparison among the three methods, for the standard wafer, is presented in Figs. 6. The percentage differences, assuming that the measurement from the manufacturer is the accurate base, are also listed below:

Standard wafer #1:

Interferometer: Differences in slope = 0.72 %
                 Differences in intercept = 3.09 %
                 Accumulated differences in film thickness within 20,000 μm distance = 82 Å

ISE: Differences in slope = 0.69 %
                 Differences in intercept = 0.55 %
                 Accumulated differences in film thickness within 20,000 μm distance = 47 Å

Based on the above differences calculated from the regression program, the measured results from the ISE after correction (calibration) due to non-uniform magnification are well within the accuracy of any other techniques used. Two identical standard wafers were purchased and analyzed. The results from the ISE for wafer #2 were nearly identical to the results presented above for wafer #1.

203

V. CONCLUSIONS

A new experimental technique for measuring film thickness profiles, Image Scanning Ellipsometry, was developed and tested. The technique is based on conventional null Ellipsometry. The experimental results, presented in this paper, established and confirmed the accuracy of full-field imaging for measuring the film thickness profile of a non-uniform film by sweeping the null points across the sample surface. The ISE system has been shown to require an additional correction (calibration) in the measured horizontal distance, which might be due to four factors: (1) the imaging system is not oriented perpendicular to the substrate and so the horizontal magnification varies in this direction, (2) the allocation of the exact position of the dark fringes is limited by the ability to accurately digitize and analyze the images, (3) the sensitivity of the polarizer settings with respect to the film thickness limits the number of null points possible, and (4) the limited magnification of the ISE hinders the exact location of a null point. Factors (2) and (4) limit the location of the null points to $\pm$ 1 pixel width. In this study that is $\pm$ 7.5 μ

V.   REFERENCES

1.   Bankoff, S.G., "Dynamics and Stability of Thin Heated Liquid Films," *ASME J. of Heat Transfer*, **112**, 538-546 (1990).

2.   Wayner, Jr., P.C., "The Effect of Interfacial Mass Transport on Flow in Thin Liquid Films", *Colloids and Surfaces*, **52**, 71-84 (1991).

3.   Tan, M.J., Bankoff, S.G., and Davis, S.H., "Steady Thermocapillary Flows of Thin Liquid Layers, I" *Physics of Fluids A, Fluid Dynamics*, **2**, 313-321, (1990).

4.   Burelbach,J.P., Bankoff,S.G., and Davis,S.H., "Steady Thermocapillary   Flows of Thin Liquid Layers, II" *Physics of Fluids A, Fluid   Dynamics*, **2**, 322-333, (1990).

5.   S. DasGupta, J. Schonberg, and P. C. Wayner, Jr., "Investigation of an Evaporating Extended Meniscus Based on the Augmented Young-Laplace Equation", J. of Heat Transfer, Vol. 115, 201-208(1993).

6.   R. F. Cohn, J. W. Wagner, and J. Kruger, "Dynamic Imaging Microellipsometry: Theory, System, Design, and Feasibility Demonstration", Applied Optics, Vol. 27, **22**, 4644-4671 (15 November, 1988).

CHARACTERIZATION OF THERMAL PLASMAS BY LASER LIGHT SCATTERING

S. C. Snyder, G. D. Lassahn, L. D. Reynolds, and J. R. Fincke

Idaho National Engineering Laboratory
EG&G Idaho, Inc., P. O. Box 1625, Idaho Falls, ID 83415

ABSTRACT

Characterization of an atmospheric pressure free-burning arc discharge and a plasma jet by lineshape analysis of scattered laser light is described. Unlike emission spectroscopy, this technique provides direct measurement of plasma gas temperature, electron temperature and electron density without the assumption of local thermodynamic equilibrium (LTE). Plasma gas velocity can also be determined from the Doppler shift of the scattered laser light. Radial gas temperature, electron temperature and electron density profiles are presented for an atmospheric pressure argon free-burning arc discharge. These results show a significant departure from LTE in the arc column, contradicting results obtained from emission spectroscopy. Radial gas temperature and gas velocity profiles in the exit plane of a subsonic atmospheric pressure argon plasma jet are also presented. In this case, the results show the plasma jet is close to LTE in the center, but not in the fringes. The velocity profile is parabolic.

INTRODUCTION

It is not possible to determine thermal plasma gas temperature from emission spectroscopy unless the plasma is in local thermodynamic equilibrium (LTE). Because electron densities are high (> 10^{23} m^{-3}), kinetic processes of atmospheric pressure free-burning arc discharges and thermal plasma jets are dominated by electron collisions. It has therefore been generally assumed that LTE exists in these plasmas [1-3], and emission spectroscopy could be used to accurately measure the gas or kinetic temperature of the plasma. A more realistic description of the plasma is probably that of partial local thermodynamic equilibrium (PLTE), which assumes that the free electrons are in equilibrium with the populations of the upper excited states, but not necessarily with the ground state [4,5]. If the plasma is in PLTE, emission spectroscopy can determine the electron temperature, but not the gas temperature.

Analysis of the lineshape of laser light scattered by the plasma is probably the only direct and unintrusive method of determining gas temperature, electron temperature, electron density, and gas velocity without the assumption of LTE and with a high degree of spatial resolution. We describe in this paper the characterization of thermal plasmas by lineshape analysis of scattered laser light. Radial gas temperature, electron temperature and electron density profiles determined by this technique are presented and discussed for an atmospheric pressure argon free-burning arc discharge. Radial gas temperature and gas velocity profiles in the exit plane

of a subsonic atmospheric pressure argon plasma jet are also presented and discussed.

THEORY

Scattering of electromagnetic radiation by a medium is due to density fluctuations within the medium [6]. In the case of ionized gases, density fluctuations of the atoms and ions give rise to Rayleigh scattering, while density fluctuations of the free electrons give rise to Thomson scattering. The total scattered light signal from a thermal plasma is therefore a combination of Rayleigh scattering from atoms and ions, and Thomson scattering from free electrons. The lineshape of Thomson scattered light has two components. One component, called the electron feature, is due to the density fluctuations of the free electrons themselves. The other component is known as the ion feature and is due to the electrostatic influence of the density fluctuations of the ions on the free electrons. The lineshape of Rayleigh scattered light is Gaussian for our experimental conditions [7]. The spatial radiation pattern of both Rayleigh and Thomson scattered light is that of the oscillating electric dipole.

The Thomson lineshape can be written as [6]

$$S(\vec{k},\omega) = \frac{2\pi}{k} \left|1 - \frac{G_e}{\epsilon}\right|^2 f_{oe}\left(\frac{\omega}{k}\right) + \frac{2\pi Z}{k} \left|\frac{G_e}{\epsilon}\right|^2 f_{oi}\left(\frac{\omega}{k}\right),\qquad(1)$$

where k is the magnitude of the difference between the scattered wavevector and the incident wavevector $(\vec{k} = \vec{k_s} - \vec{k_o})$, ω is the difference between the angular frequency of the scattered light and the incident laser $(\omega = \omega_s - \omega_o)$, and $\epsilon = 1 + G_e + G_i$ is the longitudinal dielectric constant of the plasma. The functions G_e and G_i are screening integrals defined by

$$G_e(\vec{k},\omega) = \lim_{\gamma \to 0} \int_{-\infty}^{\infty} \frac{4\pi e^2 n_e}{m_e k^2} \frac{\vec{k} \cdot \frac{\partial f_{oe}}{\partial \vec{v}}}{\omega - \vec{k} \cdot \vec{v} - i\gamma} \, d\vec{v},\qquad(2)$$

and

$$G_i(\vec{k},\omega) = \lim_{\gamma \to 0} \int_{-\infty}^{\infty} \frac{4\pi Z e^2 n_i}{m_i k^2} \frac{\vec{k} \cdot \frac{\partial f_{oi}}{\partial \vec{v}}}{\omega - \vec{k} \cdot \vec{v} - i\gamma} \, d\vec{v},\qquad(3)$$

where the f's are the generalized one dimensional velocity distribution functions for electrons and ions, denoted by the subscripts e and i respectively, the m's are the electron and ion masses, the n's are the electron and ion number densities, e is the electron charge, and Z is the ion charge, equal to one for this experiment. It is assumed that the electrons and ions have Maxwellian velocity distributions characterized by electron and ion temperatures T_e and T_i. We have in one dimension for electrons

$$f_{oe}(v) = \left(\frac{m_e}{2\pi k_B T_e}\right)^{1/2} \exp\left(-\frac{m_e v^2}{2k_B T_e}\right),\qquad(4)$$

and for ions

$$f_{oi}(v) = \left(\frac{m_i}{2\pi k_B T_i}\right)^{1/2} \exp\left(-\frac{m_i v^2}{2k_B T_i}\right),\qquad(5)$$

206

where k_B is Boltzmann's constant. It is also assumed that the ion temperature equals the gas temperature. The first term in Eq. (1) is the electron feature and second term is the ion feature. The electron feature is considerably broader than the ion feature, scaling roughly as $(m_i/m_e)^{1/2}$. Plots of the electron feature and ion feature where the scattering angle is 90° and the incident laser wavelength is 532 nm for a hypothetical argon plasma with T_e = 15000 K, T_i = 13000 K, and n_e = 6.40 x 10^{22} m^{-3} are presented in Figs. 1 and 2, respectively. The two peaks in the electron feature are due to scattering from electron waves in the plasma. The effect of scattering from ion-acoustic waves is seen in the two humps of the ion feature.

The plasma gas velocity $\vec{v}$ can be determined directly from the Doppler shift of the ion feature relative to the frequency of the incident laser by

$$\Delta\omega_D = \vec{k}\cdot\vec{v} . \tag{6}$$

EXPERIMENTAL

Lineshape measurements were made in a vertical free-burning arc and in the jet of a commercial subsonic plasma spay torch, both operated with argon at atmospheric pressure (640 mm Hg). The arc was generated by a standard gas-tungsten arc (GTA) welding torch using a 2.4 mm diameter thoriated-tungsten cathode ground to a 60° included tip angle, and was operated over a water-cooled copper anode. The cathode-to-anode gap was 9 mm and the arc current was 100 A. The plasma spay torch was operated 900 A with a gas flow rate of 35.4 l min^{-1}. The torch nozzle diameter was 8 mm.

Because of the intense plasma background radiation and relatively weak signal strengths, the use of a high-powered pulse laser and gated detection is necessary to measure the scattered light signal.

Resolving the electron feature does not require high resolution spectroscopy. For these measurements, a frequency-doubled pulsed Nd:YAG laser generating 10 ns pulses at a wavelength of 532 nm and a scanning 1.3 m monochromator with a 1200 groove mm^{-1} grating were used. The laser pulse rate was 10 Hz. The scattered laser light pulses were detected with a photomultiplier tube (PMT) and boxcar averager synchronized to the firing of the laser. The output of the boxcar averager, averaged over 10 laser shots, was digitized by an analog-to-digital (A-D) converter and stored on a computer. A spectral range of ~ 16 nm centered about 532 nm was scanned for a typical electron feature. The laser beam was normally incident to the flow axis of the arc discharge and the scattering angle was 90° to the flow axis and incident laser beam. The GTA torch was mounted on a translation stage, and radial positions were determined by translating the torch relative to the incident laser beam. The spatial resolution of the measurements was ~ 3 x 10^{-3} mm^3. A half-wave plate was used to rotate the polarization of the incident laser beam to maximize the scattering signal and to verify that the dependence of the signal intensity on the polarization angle was characteristic of oscillating electric dipoles and not stray light. A schematic of the setup to measure the electron feature is given in Fig. 3.

Measurement of the ion feature does require high resolution spectroscopy. The use of a high-powered pulse laser and gated detection is still necessary, but in this case, the incident laser bandwidth must be less than the bandwidth of the ion feature. The fairly recent availability of injection-seeded Nd:YAG lasers fulfills these requirements. Accordingly, the
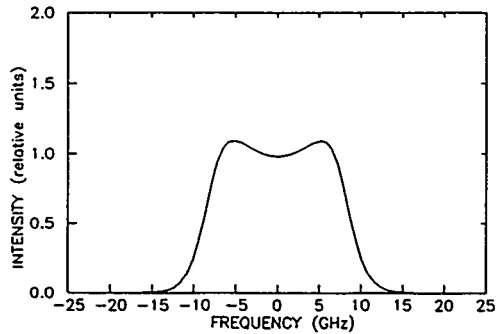
Figure 1. Ion feature for a hypothetical plasma with T_e = 15000 K, T_i = 13000 K, and n_e = 6.4 x 10^{22} m^{-3}.

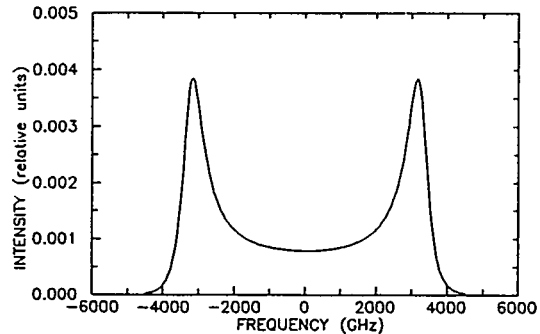**Figure 2.** Electron feature for a hypothetical plasma with T_e = 15000 K, T_i = 13000 K, and n_e = 6.4 x 10^{22} m^{-3}.

experimental setup for resolving the ion feature was similar to the electron feature experiment, except that a pulsed frequency-doubled injection-seeded Nd:YAG laser operating at a wavelength of 532 nm with a pulse duration of 10 ns and pulse rate of 20 Hz was used as the laser source. The bandwidth of the laser is < 100 MHz. Furthermore, a scanning tandem Fabry-Pérot interferometer (F-PI) was used for spectral analysis of the scattered light. The scattering angle for ion feature measurements made in the free-burning arc was also 90° and normal to the flow axis and incident laser beam. The plasma jet was operated vertically with the scattered light collected at an angle of 10° from the flow axis in the plane formed by the flow axis and the incident laser wave vector which was normal to the flow axis. This gave a scattering angle of 80°. More details about the measurement of the ion feature can be found elsewhere [7]. The schematic for the ion feature experiment is presented in Fig. 4.

RESULTS AND DISCUSSION

Both electron and ion features were recorded in the free-burning arc, but only the ion feature was recorded in the plasma jet. An experimentally resolved electron feature taken in the free-burning arc is shown in Fig. 5. The electron temperature and electron density were determined from a nonlinear least squares fit of Eq. (1) to this data. This fit is represented by the solid curve. The value of T_e stated in Fig. 5 is strongly influenced by laser heating, and the data must be corrected for this, as described elsewhere [8]. Ion temperatures and electron densities are not effected by laser heating. A typical experimental ion feature from the plasma jet is shown in Fig. 6. In general, these lineshapes are treated as a superposition of Thomson and Rayleigh scattering. The solid curve now represents a nonlinear least squares fit of Eq. (1) superposed with a Rayleigh component described by a Gaussian function to the raw lineshape data. In this case, the contribution from Rayleigh scattering to the total lineshape is < 1%. The ion or gas temperature was determined from this fit. The peak in the center, which was fitted by a Gaussian superposed with the total lineshape function, was the response of the F-PI to the incident laser light. This provides a reference frequency from which Doppler shifts are measured and a measurement of the F-PI instrument response function for deconvolution purposes. The lineshape shows a definite Doppler shift due to the flow velocity of the jet relative to the reference frequency. The gas velocity was determined from this shift using Eq. (6).
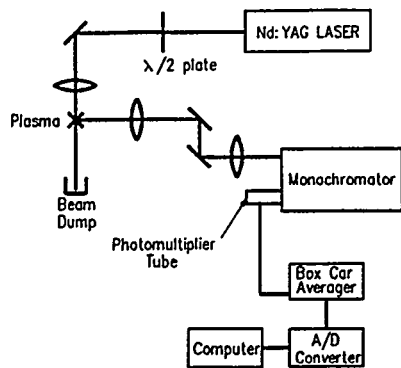
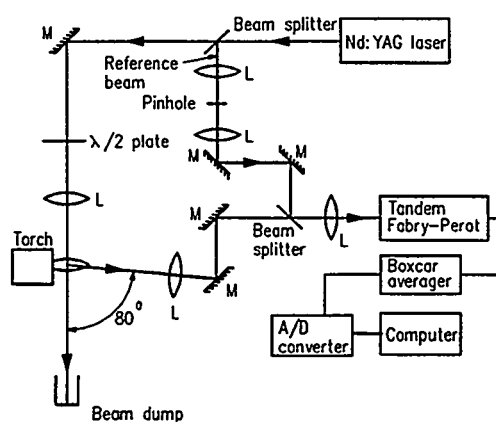**Figure 3.** Experimental setup to measure the electron feature.

Figure 4. Experimental setup to measure the ion feature.

Radial profiles of gas temperature and electron temperature, corrected for laser heating, of the free-burning arc at 2 mm below the cathode determined from analysis of scattered laser light are presented in Fig. 6. A significant departure from LTE is evident throughout the arc, especially at the center. These results clearly contradict the generally accepted assumption that LTE exists in the column of atmospheric pressure arcs [1-3].

The radial profile of electron density at 2 mm below the cathode tip determined from analysis of the electron feature of the scattered laser light is presented in Fig. 7. These results agree reasonably well with electron density profiles of similar arcs determined from Stark broadening, which is independent of LTE [3].

The radial gas temperature profiles of the plasma jet with an operating current of 900 A determined from lineshape analysis is compared with the radial temperature profile determined from standard emission spectroscopy [7] in Fig. 9. It is evident from this data that the plasma jet is close to LTE in the center, but not in the outer regions. This is probably due to radiation trapping by ground state argon atoms and electron diffusion [4].

Until now, reliable exit plane velocity profile data of plasma jets has not been available. By analogy with incompressible laminar flow in a cylindrically symmetric channel, computational modelers [9] postulate that the velocity profiles are nearly parabolic. To examine this, the radial velocity profile at 2 mm downstream from the torch exit from r = 0 to r = 3 mm was fit to a parabola after being reflected about the flow axis, and is plotted in Fig. 10. As can be seen, the fit is quite good and justifies the assumption of parabolic velocity profiles.

CONCLUSIONS

Lineshape analysis of laser light scattered by a plasma allows the direct measurement of plasma gas temperature, electron temperature and electron density, and plasma gas velocity. This method is unintrusive, has a high degree of spatial resolution, does not require an Abel inversion, and, most importantly, does not rely on an assumption of LTE to interpret the data. Using this technique, we have for the first time, to our knowledge, directly investigated the existence of LTE in atmospheric pressure free-burning argon arcs and atmospheric pressure, subsonic argon plasma jets. We have found strong evidence that LTE does not exist in the arc column of the free-burning

argon arc, contrary to expectations. We have also found that the core region of an plasma jet is close to LTE, but there is a severe departure from LTE in the fringes. The radial velocity profile in the exit plane of the plasma jet is very nearly parabolic, as postulated.
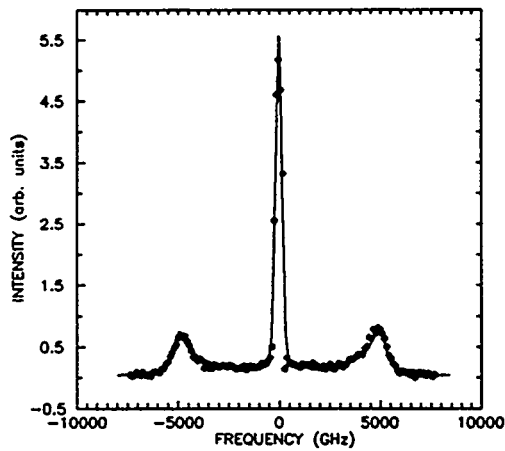

Figure 5. Electron feature in a free-burning arc at 2 mm below the cathode at the radial position r = 0 mm. T_e = 28240 K ± 3% and n_e = 1.62 x 10^{23} m^{-3} ± 3%.
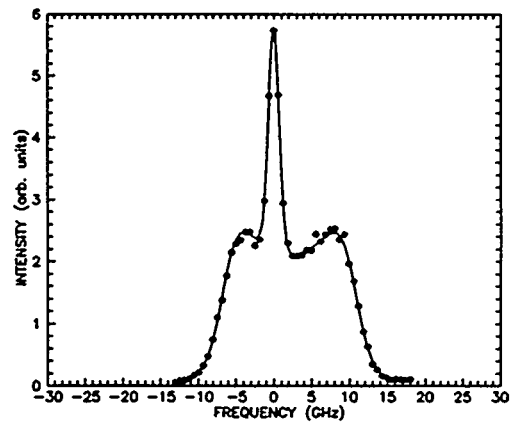

Figure 6. Experimental ion feature from the plasma jet at 2 mm downstream from the exit and at r = 0 mm. T_i = 12630 K ± 7% and the gas velocity v = 1095 m s^{-1} ± 3%.
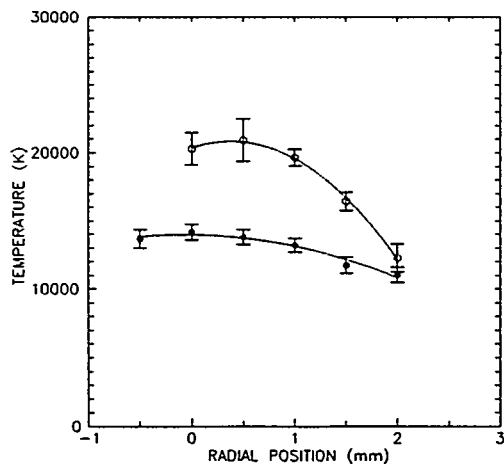

Figure 7. Radial temperature profiles of a free-burning arc at 2 mm below the cathode. The solid dots are the gas temperature. The open circles are the electron temperature.
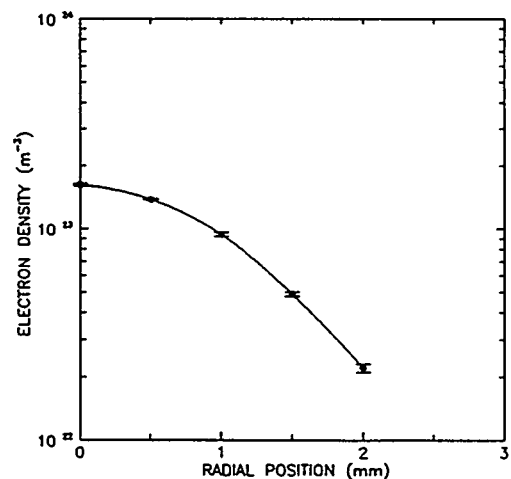

Figure 8. Radial profile of electron density in a free-burning arc at 2 mm below the cathode.
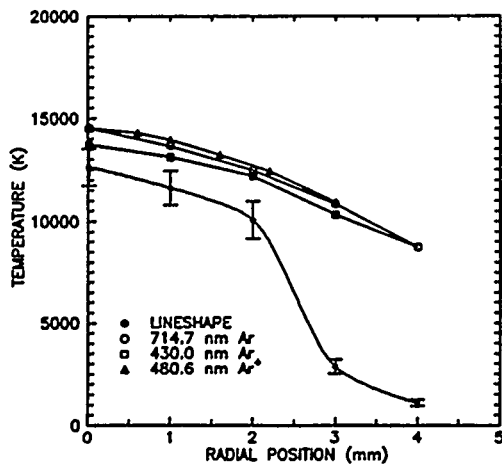
210

Figure 9. Radial temperature profiles of a plasma jet at 2 mm downstream from the torch exit determined from lineshape analysis and emission spectroscopy. Torch operating current was 900 A.
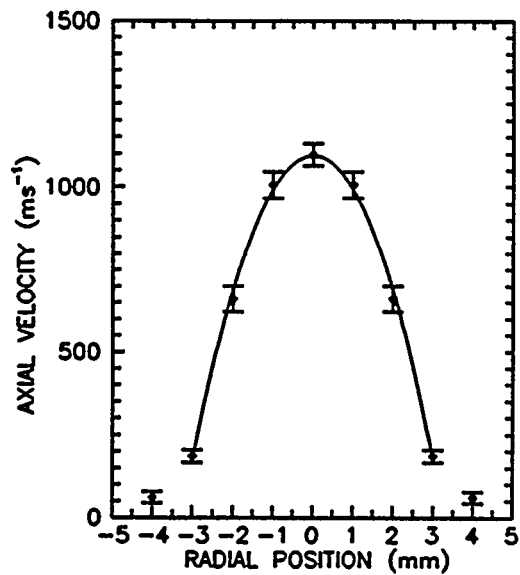

Figure 10. Radial velocity profile of a plasma jet at 2 mm downstream from the torch exit. The solid curve is a parabolic fit of the data. Torch operating current was 900 A.

ACKNOWLEDGMENTS

REFERENCES

1. H. N. Olsen, "The Electric Arc as a Light Source for Quantitative Spectroscopy," *J. Quant. Spectrosc. Radiat. Transfer* 3, 305 (1963).

2. J. B. Shumaker and C. H. Popenoe, "A Study of Equilibrium in Argon Arcs," *J. Res. N. Bur. Stand. Sect. A* 76, 71 (1972).

3. P. Vervisch, B. Cheron, and J. F. Lhuissier, "Spectroscopic Analysis of a TIG Arc Plasma," *J. Phys. D: Appl. Phys.* 23, 1058 (1990).

4. J. Heberlein, "Investigation of the Anode Boundary Layer of an Atmospheric Pressure Argon Arc," Ph.D. Dissertation, University of Minnesota, Minneapolis, MN (1975).

5. C. H. Kruger, T. Owano, and M. Gordon, "Measurement of Nonequilibrium Effects in Thermal Plasmas," *Pure and Appl. Chem.* 62, 1833 (1990).

6. J. Sheffield, *Plasma Scattering of Electromagnetic Radiation*, (Academic Press, New York, 1975).

7. S. C. Snyder, L. D. Reynolds, G. D. Lassahn, J. R. Fincke, C. B. Shaw, Jr., and R. J. Kearney, "Determination of Gas Temperature and Velocity Profiles in an Argon Thermal Plasma Jet by Laser Light Scattering," *Phys. Rev. E* 47, 1996 (1993).

8. S. C. Snyder, L. D. Reynolds, G. D. Lassahn, "Direct Evidence of Departure from Local Thermodynamic Equilibrium in a Free-burning Arc Discharge Plasma," submitted to *Phys. Rev. Lett.*

9. A. H. Dilawari and J. Szekely, "Some Perspectives on the Modeling of Plasma Jets," *Plasma Chem. and Plasma Processing* 7, 317 (1987).

APPLICATION OF HYSTERESIS MODELING TO MAGNETIC TECHNIQUES FOR MONITORING BIAXIAL STRESS

M. J. Sablik, G.L. Burkhardt, and H. Kwun
Southwest Research Institute
P.O. Drawer 28510
San Antonio, TX 78228-0510

ABSTRACT

A probe, consisting of two excitation coils and a detection coil wrapped around a core with a Hall probe between the pole pieces, has been used to measure indirectly the influence of biaxial stress on the magnetic properties of a ferromagnetic specimen, in this case annealed SAE-4130 steel. Properties measured indirectly included remanence, coercivity, and first, third and fifth harmonic amplitudes. The properties were extracted from the voltage measured across the detection coil and incorporate the magnetic influence of the soft iron core, but with the effect of air gap variation between pole piece and sample kept to a controlled range. Results were compared to a micromagnetic model for the effect of biaxial stress on hysteresis and on magnetic properties. The micromagnetic model is a modified version of a model previously employed by Schneider et al. The experimental remanence variation due to biaxial stress compared very well to the predictions of the model. Furthermore, the model predicts, and experiment bears out, that the remanence with the field along one stress axis minus the remanence with the field along the other stress axis falls in a straight-line band of values when plotted against the difference of the two stresses. This suggests a possible NDE technique for detecting differences in biaxial stresses at a given location in a steel specimen.

INTRODUCTION

The effects of biaxial stress on magnetic properties is important to understand if one is to use magnetic NDE techniques for detecting stress in pipeline. Stress in pipeline consists of perpendicularly acting biaxial stresses, namely circumferential stress about the pipe and longitudinal stress along the length of the pipe. The magnetic properties of a steel pipeline at a given location will be affected by both stresses, longitudinal and circumferential. Thus, if one is to use in pipeline a magnetic nondestructive evaluation (NDE) stress detection technique, one needs to first understand the precise way in which biaxial stresses affect magnetic properties.

Stress in pipeline is caused by internal pressure in combination with stress from external pipeline conditions. In very cold climates, such as in Alaska, the ground freezes and thaws and in the process, the resulting ground movement exerts great stress on pipeline. In regions such as in California, where there is often sudden crustal plate motion along faults, ground movement can again produce great stresses on pipeline. Ground settling in swamplands such as Louisiana and desert sand motion such as in Saudi Arabia can often expose pipeline and cause stresses on the pipeline owing to its own weight. Silt motion at bay bottoms can also expose pipeline and even set up a situation where a pipeline might snag a passing ship. All of these situations could lead to pipeline rupture and need to be detected before the danger becomes reality.

Thus, it is important from an energy engineering point of view, to protect against high stress conditions in pipeline and to monitor biaxial stresses in pipeline. The purpose of the present study is to develop

an understanding of the way in which biaxial stresses affect magnetic properties so that magnetic NDE techniques can be utilized in monitoring stress in pipeline.

This paper represents a progress report for an ongoing study of the effect of biaxial stresses on various magnetic properties in steels. It is basically divided into two sections - (1) experimental work and (2) theoretical work confirming experimental observations.

Experimental results in mild steel on the effect of biaxial stress on hysteresis loop parameters were studied recently by Langman.[1] However, discussion was restricted to equal biaxial stresses. Other researchers have studied biaxial stress effects on various magnetic properties[2-5], but to date, there has not been a systematic study presented on variation of d.c. hysteresis parameters under general, unequal biaxial stress conditions. This paper in part addresses that.

Theoretical models for the effects of biaxial stress on magnetic properties have been published by Schneider et al[6] and by Kashiwaya[7]. In this paper, we modify Schneider's micromagnetic model for biaxial stress effects by borrowing some ideas from Kashiwaya, but modifying those ideas so that a better description of biaxial tensile effects on magnetic properties is possible.

EXPERIMENTAL MEASUREMENTS

The biaxial loading apparatus is shown in Fig. 1. It is designed so as to exert stresses independently along two perpendicular axes. The stresses are exerted on a cruciform (cross-shaped) specimen. The central region of the specimen experiences the effect of biaxial stresses.

The specimen used was made of SAE-4340 steel and was 0.2" thick in the central region. At the end of each arm, the specimen was 0.4" thick. Also, in the 0.4" thick portion, a 0.75" diameter hole was drilled for attachment to a pin in the biaxial stress fixture. Each arm was 1.5" wide and 2.25" long and the central region of the specimen would have been 1.5" square, except that, to smooth out the corners, a 90° circular arc of 0.5" radius of curvature was cut tangent to the arm edges joined by the arc. The specimen was chamfered where it changed from 0.2" to 0.4" thick at a place 1.5" away from the arm end.

A finite element study showed that under 1:1 load conditions, the ratio of perpendicular stresses $\sigma_2:\sigma_1$ varied from 1.08 to 0.92 in a center region that was 0.75" square. Thus, under a 1:1 load condition, the stresses in the center were uniform to ±8%. Our probe was designed to fit across that region with a distance of 0.6" between pole centers. Thus, we could expect a maximum error of the order of less than ±8% owing to the slight nonuniformity of the stress distribution.

A diagram of the sensor probe is seen in Fig. 2. The sensor consisted of excitation coils wound about both arms of a C-core, and a detection coil wound tightly at the end of one of the arms. The coils were held in place by a plastic fixture, which also held a Hall probe centered between the pole pieces and close to the sample surface. Pole piece ends and plastic fixture were all carefully machined so as to be flush against the specimen surface. A weight was then placed on top of the probe so as to press the probe against the specimen surface, and thereby minimize variations in liftoff from the specimen surface.

A second plastic fixture was designed to allow the probe to be rotated into one of three fixed positions: 0°, 45°, and 90°. Thus, a magnetic field would be generated by the probe excitation coils in one of three directions - parallel to the σ_2-axis, parallel to the σ_1-axis, or at 45° with respect to either of the two stress axes.

The experiment performed was to hold the magnetic field fixed in each of the three positions (0°,45°,90°) while varying the biaxial stresses in 16 combinations per position ($\sigma_1 = 0, 70, 140, 210$ MPa; $\sigma_2 = 0, 70, 140, 210$ MPa) [Note: 6.9 MPa = 1 ksi, and, further, positive stress is tensile stress].

For each field alignment and each stress combination, a hysteresis loop was taken using a quasi d.c. signal of 5 Hz. From the loop were extracted values for B_r (remanence), H_c (coercivity), and harmonic amplitudes A_1, A_3 and A_5, using appropriate instrumentation.

214

Figure 1. Photograph of biaxial stress fixture.
Cruciform specimen (not visible) is in the fixture
held by clamps. The sensor probe on the surface
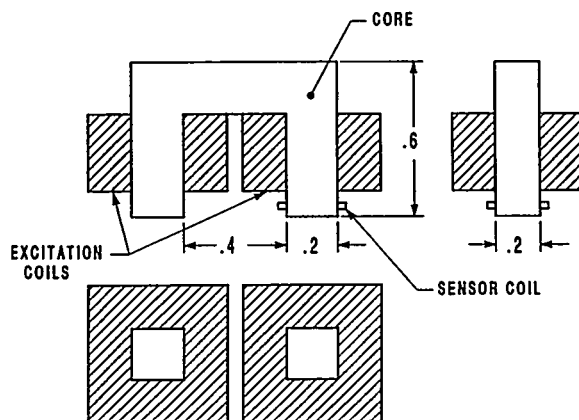of the specimen is obscured by a plastic fixture.

Figure 2. Diagram of the basic components of
sensor probe. (Dimensions in inches).

Repeat measurements indicated a possible range of uncertainty in the measurements of ±6%, in the worst case. Most of this seemed to be due to liftoff variations despite efforts to minimize liftoff variation.

Experimental results will be discussed after presentation of the theoretical model.

THEORETICAL MODEL

A discussion of the basic micromagnetic model used by Schneider et al may be found in Ref. 8. In that model, the change in magnetization ΔM at the end of a process in which magnetic field H or stress σ varies is

$$\Delta M = \sum_i \int f_i \chi (H_i) dH_i , \qquad [1]$$

where the sum i is over domains with magnetization oriented in different directions. There are a finite number of different domains to consider in single crystals and a very large number to consider in polycrystals. The weight factor f_i is an appropriate weight factor for each domain, which for polycrystals is equivalent to different $\cos \theta_i$ for equally spaced θ_i. The $\chi (H_i)$ is the magnetic susceptibility dM/dH_i associated with change dH_i in internal field H_i, which is computed from

215

$$H_i = H - (3\lambda_s \sigma \cos \theta_i / B_s) - D_\sigma M,$$ [2]

where the middle term is the stress contribution H_σ to the internal field and $-D_\sigma M$ is the stress demagnetization contribution. D_σ is a function of stress which behaves as in Fig. 1 of Ref. 8. In eq. (2), λ_s is the saturation magnetostriction, B_s is the saturation flux density, and D_σ is the stress demagnetization factor.

In eq. (1), the susceptibility χ $(H_i) = dM/dH_i$ can be obtained from the equation

$$\chi^{-1}(H_i) = \chi^{-1}(H) - D_\sigma$$ [3]

and the change dH_i can be obtained from

$$dH_i = dH / (1 + \chi(H_i) D_\sigma)$$ [4]

for processes in which H varies while σ is held constant, or from

$$dH_i = \frac{d\sigma [3 (\lambda_s / B_s) \cos \theta_i]}{(1 + \chi(H_i) D_\sigma)}$$ [5]

for processes in which σ varies while H is held constant. The reader is referred to Ref. 8 for details.

Schneider and Richardson[6], in treating biaxial stress effects, asserted that the above model may be still used, but with σ replaced by $\sigma_{eff} = \sigma_1 - \sigma_2$ and $d\sigma$ by $d\sigma_{eff} = d\sigma_1 - d\sigma_2$ in the case where H is parallel to the σ_1-axis, and by $\sigma_2 - \sigma_1$ and $d\sigma_2 - d\sigma_1$ respectively when H is parallel to the σ_2-axis. This, however, does not prove to be satisfactory.

Kashiwaya[7] proposed a formalism which in effect would require that σ be replaced by either $\sigma_{eff} = \sigma_1 - \sigma_{max}$ or $\sigma_{eff} = \sigma_2 - \sigma_{max}$, depending on the field direction, where σ_{max} is the larger of the two stresses. This would require that $\sigma_{eff} \leq 0$ and that if $\sigma_{max} = \sigma_2$, then with H pointed along the σ_2-axis, σ_2 has no magnetic effect regardless of its value. This is a bit extreme. For a polycrystal, it is found from the Schneider formalism that the contribution from $H_\sigma = -3\lambda_s \sigma_{eff} \cos \theta_i / B_s$ tends to average out over all domains i as H is varied with σ_{eff} constant and that the dominant contribution to ΔM is from the demagnetization term $-D_\sigma(\sigma_{eff}) M$ in the internal field. For positive values of σ_{eff}, $D_\sigma(\sigma_{eff})$ is very small but finite, staying approximately constant between 0 and 100 MPa, and then becoming larger but at a slower rate than is found at negative stresses.[8]

Thus, for positive σ_{eff}, it is found at effective stress values $\sigma_{eff} \leq 100$ MPa, there is little change in the magnetic properties, in agreement with Kashiwaya's general predictions, but that for $\sigma_{eff} > 100$ MPa, there begins to be found a noticeable change in magnetic properties. The key therefore is to find an appropriate expression for σ_{eff}.

In evaluating σ_{eff}, it is important to consider the relative stress with respect to the third axis, along which there is no stress. Thus, the magnetic properties are affected by relative stresses with respect to all the axes. Since compression tends to push moments away from the stress axis and tension tends to pull moments toward the stress axis, one should also expect that the magnetic properties would be affected differently depending on whether the field is parallel to an axis of tension or compression. Thus, if the field is parallel to the σ_1-axis, and σ_1 is compressive (i.e. negative), then $\sigma_{eff} = (1/2) [(\sigma_1 - \sigma_2) + \sigma_1]$. In other words, with field parallel to the σ_1-axis and with σ_1 compressive, the effective stress contributing to magnetic properties is the average of the relative stresses with respect to the other two orthogonal directions (viz. $\sigma_1 - \sigma_2$ and $\sigma_1 - 0$). On the other hand, if σ_1 is tensile (i.e. positive), then from relative stress $\sigma_1 - \sigma_2$, one subtracts off the relative stress between the σ_2-axis and the perpendicular zero stress axis. Thus, for tensile σ_1, $\sigma_{eff} = (1/2) [(\sigma_1 - \sigma_2) - \sigma_2]$. With $\sigma_2 = 0$, then $\sigma_{eff} = \sigma_1$ and with $\sigma_1 = 0$, then $\sigma_{eff} = -\sigma_2$, in accordance with what is

known about uniaxial stress[8]. Making the above substitutions for σ_{eff} into the Schneider model constitutes the new micromagnetic model for biaxial stress.

RESULTS

In this section, experimental results are compared to theoretical results. Just as experimental magnetic parameters were extracted from experimental hysteresis loops, modeling results for magnetic parameters were obtained from hysteresis loops generated by the model.

We present here only results for remanence B_r. Since the experimental changes in B_r due to stress are scaled by the additional contribution to B_r due to the probe core, it was found necessary to compare normalized results for experiment and theory. Fig. 3 shows results for $B_r/B_r(0,0)$ vs. σ_1, where $B_r(0,0)$ is B_r for σ_1 = 0 and $\sigma_2 = 0$, and where H is parallel to the σ_1-axis. Four plots are shown, each for a different σ_2. The fit between experimental points (x) and modeling results (o) can be tuned by scaling the variation of D_σ with σ_{eff} (from Fig. 1 of Ref. 8) by a constant factor. It is seen that a very good fit is indeed attainable. Using the same scaling for D_σ with σ_{eff}, Fig. 4 displays $B_r/B_r(0,0)$ vs. σ_1 for H parallel to the σ_2-axis for both model and experiment. Since the new experimental results have some liftoff error built in, the fit between experiment and model is still good, but not quite as good as in Fig. 3.
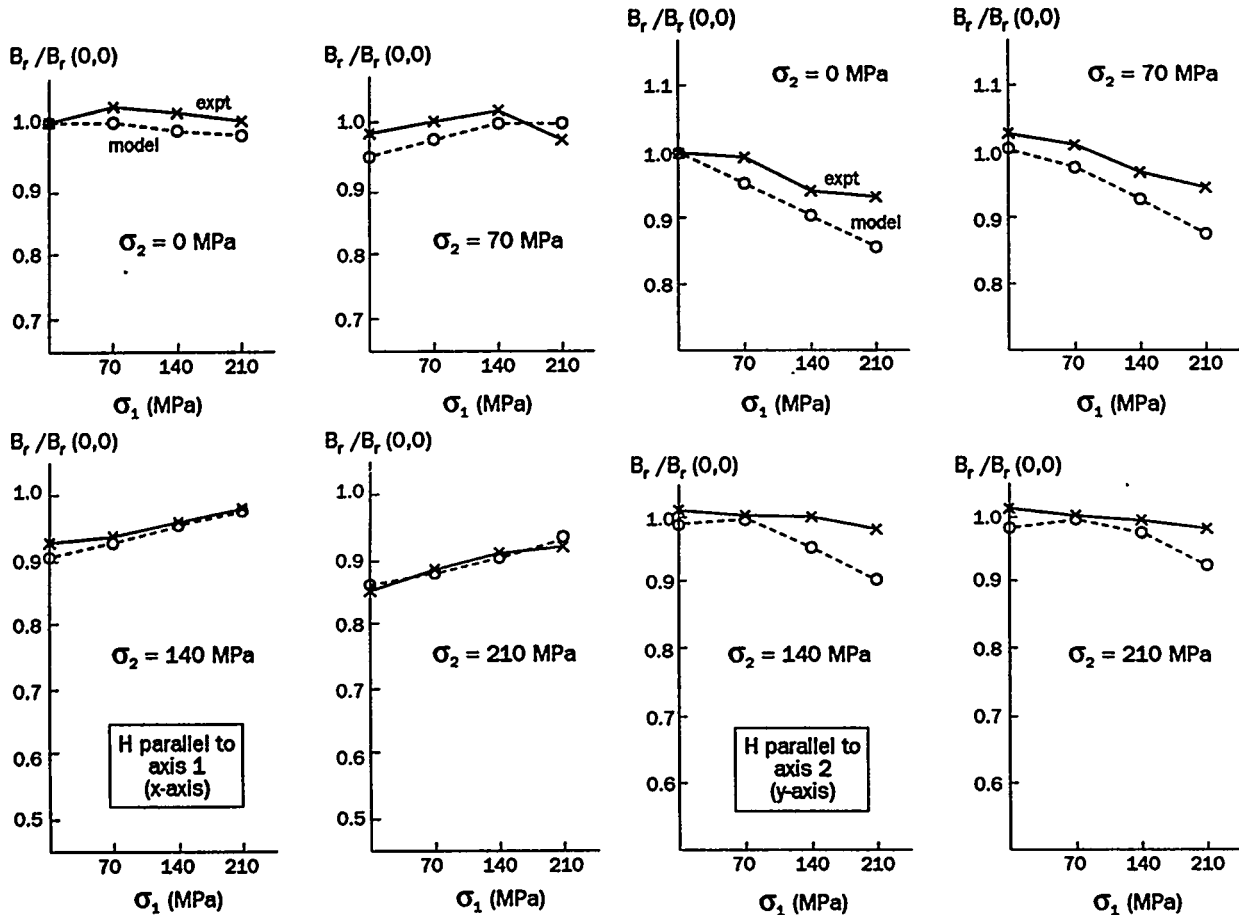

Figure 3. Comparison between model and experiment of normalized remanence values when the field is parallel to the σ_1-axis.

Figure 4. Comparison between model and experiment of normalized remanence values when the field is parallel to the σ_2-axis.

217

Fig. 5 displays $B_r/B_r(0,0)$ vs. $\sigma_1-\sigma_2$ for both theory and experiment, for the two cases where H || σ_1-axis and H|| σ_2-axis. It is noted for each case that the points all fit within a band. In the case of H || σ_1-axis, both model and experiment exhibit an increasing band of essentially constant positive slope at negative $\sigma_1-\sigma_2$, rising to a peak at positive $\sigma_1-\sigma_2$. The bands for model and experiment are approximately the same width. In the case of H || σ_2 axis, the bands for model and experiment are again of approximately the same width, but this time the peak occurs at negative $\sigma_1-\sigma_2$, and the bands decrease in value at essentially constant negative slope at positive σ_1 - σ_2.

Fig. 6 exhibits a more interesting result. When the difference in values $(B_r/B_r(0,0))$ between when the field is parallel to the σ_1 -axis and when the field is parallel to the σ_2 -axis are plotted against the stress difference $\sigma_1-\sigma_2$, a straight line band is found, both for theory and experiment. However, band widths and slopes differ slightly, possibly due to the slight experimental liftoff variation appearing in Fig. 4, which would affect the fits slightly.

Figure 5. Plots of B_r/B_r (0,0) vs. stress difference σ_1 - σ_2 for the various values taken by σ_1 and σ_2 (viz., 0, 70, 140, 210 MPa each). Both model and experiment are shown. Also, cases for H || σ_1 -axis and H || σ_2 -axis are shown.
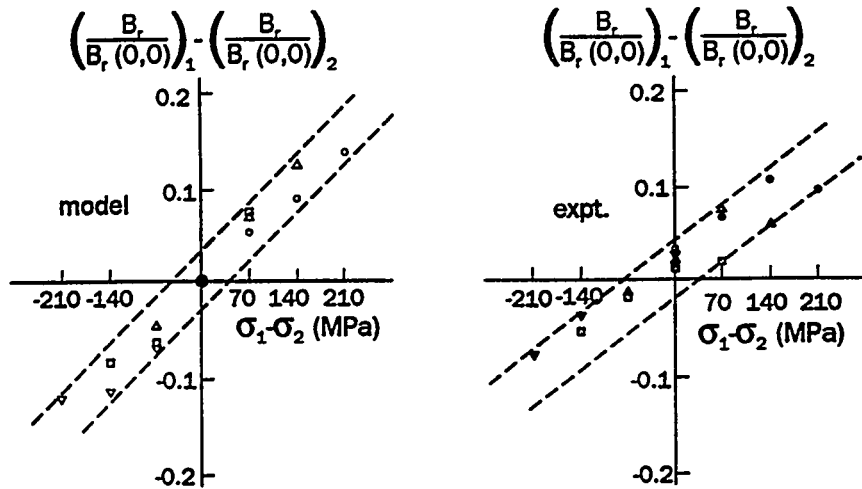

218
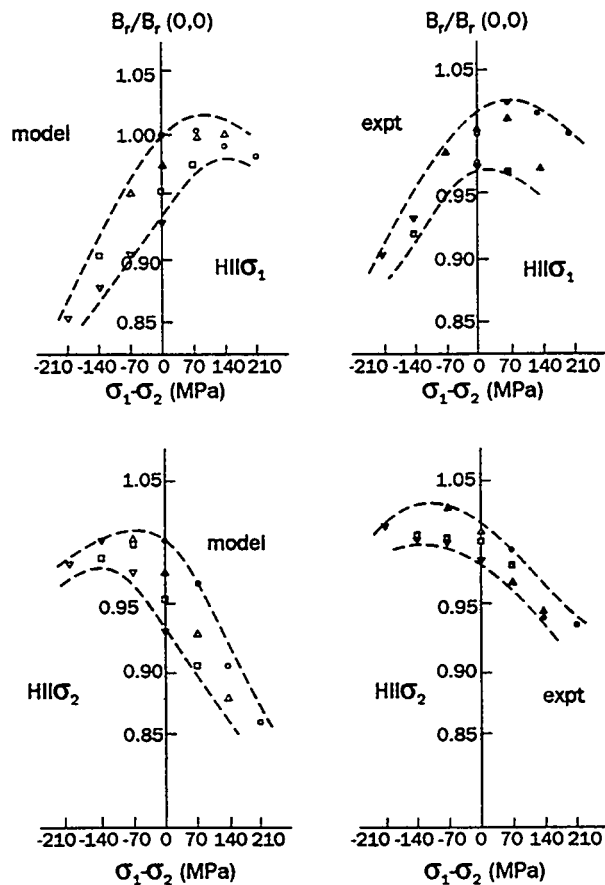
Figure 6. Differences between normalized remanence values for H $\parallel$ σ_1-axis and H $\parallel$ σ_2-axis plotted against σ_1 - σ_2. Results for both model and experiment are shown.

CONCLUSIONS

That a straight-line correlation can be found between σ_1-σ_2 and algebraically manipulated values for magnetic properties is quite useful. It means that an NDE magnetic technique can be constructed for obtaining the biaxial stress difference σ_1-σ_2 to within a certain band of error.

In this case, the difference between normalized values for remanence when field is parallel to one axis and then the other can be used to determine σ_1-σ_2 to within a certain error range (in this case, 15 ksi (105 MPa) based on experiment and 10 ksi (70 MPa) based on the model). It remains to be seen whether these error ranges can be reduced both experimentally and theoretically, or whether other magnetic properties might exhibit smaller error ranges when the same procedure is used for them.

It is anticipated that the results presented here will be expanded to other magnetic properties and to compressive stress as well as tensile stress.

ACKNOWLEDGEMENTS

REFERENCES

1. R. LANGMAN, "Magnetic Properties of Mild Steel Under Conditions of Biaxial Stress," *IEEE Trans. on Magnetics*, **26**, 1246 (1990).

2. R. LANGMAN, "Measurement of the Mechanical Stress in Mild Steel by Means of Rotation of the Magnetic Field Strength — Part 2: Biaxial Stress," *NDT International*, **15**, 91 (1982).

3. K. KASHIWAYA, H. SAKAMOTO, and Y. INOUE, "Nondestructive Measurement of Residual Stress Using Magnetic Sensors," in *Proc. VI Intl. Congress on Experimental Mechanics*, Society for Experimental Mechanics, Bethel, Conn, 1988, Vol 1, p. 30.

4. D.J. BUTTLE, W. DALZELL, C.B. SCRUBY and R.A. LANGMAN, "Comparison of Three Magnetic Techniques for Biaxial Stress Measurement," in *Rev. Progress Quant. Nondestr. Eval.*, ed. D.O. Thompson and D.E. Chimenti (Plenum, NY, NY, 1990), p. 1879.

5. G.L. BURKHARDT, H. KWUN, A.E. CROUCH, and D.A. DESNOYER, "Review of Stress Measurement Techniques for Pipelines," in *Damage Assessment, Reliability and Life Prediction of Power Plant Components*, PVP–vol. **193**, NDE–vol.8, *Proc. 1990 Pressure Vessels and Piping Conference*, Nashville, TN, 1990 (ASME, NY, NY, 1990), p.95.

6. C.S. SCHNEIDER and J.M. RICHARDSON, "Biaxial Magnetoelasticity in Steels," *J. Appl. Phys.* **53**, 8136 (1982).

7. K. KASHIWAYA, "Fundamentals of Nondestructive Measurement of Biaxial Stress in Steel Utilizing Magnetoelastic Effect Under Low Magnetic Field," *Jpn. J. Appl. Phys.* **30**, 2932 (1991).

8. C.S. SCHNEIDER, P.Y. CANNELL, and K.T. WATTS, "Magnetoelasticity for Large Stresses," *IEEE Trans. Magn.* **28**, 2626 (1992).

MIXING AND SETTLING IN CONTINUOUS METAL PRODUCTION

H. J. Richter, J. T. Laaspere, and J. M. Fitzpatrick

Thayer School of Engineering
Dartmouth College
Hanover, NH 03755

ABSTRACT

Modern metallurgical processes produce metal from ore in a single converter operated in horizontal mode to permit staging of bath and oxygen potential by utilizing bottom-blowing of oxygen and fuel. The submerged injectors must create sufficient turbulence to provide excellent gas-liquid contact in order to maximize heat and mass transfer in the bath, but this turbulence must be selectively localized so as to provide adequate phase separation zones of metal and slag between the active turbulent zones.
It is important to know the behavior of gas and liquids in the bubble plume, the nature and paths of liquids and entrainment into the plume, and separation phenomena including travel and behavior in the settling zones. Such knowledge is of fundamental value in designing reactors for continuous direct metal making.
In this work the mixing caused by submerged injection of gas into a bath simulating a converter and subsequent phase separation of two immiscible liquids representing slag and metal respectively, are being studied experimentally and analytically. First results of experiments and of the numerical analysis are presented.

INTRODUCTION

Tonnage oxygen is now employed to increase process efficiency in a great variety of both ferrous and nonferrous smelting and refining operations [1,2]. Metal is produced directly from ore concentrates in single elongated reactors using submerged gas injection. These reactors promise substantial fuel savings in metal production and much better control of pollutants than common practice, such as the blast furnace for steel production or the reverberatory furnace for copper production. Bottom blowing of oxygen made possible by Savard-Lee submerged injectors [3] was first employed in the OBM/QBOP steel converters and then in combined top- and bottom-blown steel converters [4, 5]. Bottom-blown oxygen converters are now employed for lead production in the QSL reactor [6, 7], see Figure 1. This reactor is also suitable for copper production and can be modified for continuous steel making [8]. The horizontal mode of the operation permits the staging of bath oxygen potential for continuous iron and then steel making in a single reactor and enhances scrap recycling. It has the capability for lower carbon and lower iron in the metal and slag products respectively than reactors in the vertical mode [9].

Oxygen and fuel are bottom injected into the molten bath of these essentially horizontal reactors in large volumes and at high velocities but in controlled rates required for heating, physical mixing and chemical reaction purposes. Sufficient turbulence is generated to maximize heat and mass transfer rates. However, such bath turbulence is opposite to the process requirement for continuous countercurrent flow of liquids at specific temperature, compositional and oxygen potential gradients [10]. The powerful stirring effect by submerged gas injection has to be judiciously localized so as to provide adequately calm settling zones in a staged mixer-settler configuration [11]. The behavior of gas in the liquids is of great significance in reactor design, i.e. the jetting, formation and travel of the bubble plumes in liquids, the bubble sizes within the plume, the liquid entrainment into the bubble plume and its transport upward into the lighter liquid, and the separation of the heavier liquid and subsequent settling.

However gas injection and related phenomena are of generic interest to other processes, e.g. the current major DOE-AISI direct steelmaking process [12] and e.g. severe accident analysis of nuclear reactors.
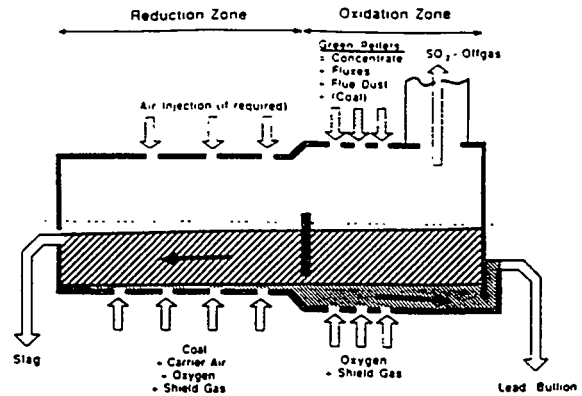
Figure 1: QSL -Reactor

Thus, the ongoing work is concerned with gas injection into a liquid bath consisting of two immiscible layers of liquid having roughly the same viscosities as slag and metal or matte and with roughly comparable density ratios. Little previous work has been done on high velocity gas injection into two immiscible liquid layers [13].

BACKGROUND

The mixing and separation of two immiscible liquid layers due to submerged gas injection or generation has been of significant interest for many years. In potential severe accident analysis of nuclear reactors it is anticipated that the liquid core melt will interact with the concrete floor of the containment building, creating a pool of oxidic and metallic phases which might undergo chemical reactions and form gases. These gases rise through the liquids and might create homogeneous mixing of the two liquid phases or, if the bubbling is weak, might allow liquid phase stratification. The mixing is a strong function of the gas generation rate [14]. This complicated three phase behavior is difficult to analyze, but assuming a rather uniform bubble generation rate across the bottom of the bath, simple bubble rise velocity and wake models were used as a first order analysis of the mixing phenomena of both liquid phases [15 to 17].

A more complicated picture arises in modern metallurgical reactors. The requirement for these reactors is the injection of tonnage oxygen plus a fuel or reducing agent through submerged injectors into the bath consisting of liquid layers of high density, low viscosity metal and lower density but higher viscosity slag. Not only is submerged injection suggested for modern copper reactors [7], it is already practice in lead production [18] and e.g. in the Q-BOP reactor for steel making. The gas injection has to be fast enough to prevent liquid metal from clogging the injectors and should enable chemical reactions to occur within the bath. Thus jetting of the gas through the bath is detrimental to the process.

The chemical reactions are oxidation of the metal sulfide in the oxidation zone and reduction to metal in the reduction zone of the reactor. Since the reduction to metal cannot be established in one gas injection, a staging process along the reactor has to occur, where the metal oxides and sulfides in the slag are gradually reduced. Thus, a multitude of submerged injectors is needed with varying reduction potential. There must be sufficient space in the reactor between injectors to permit settling of the heavier metal after intensive mixing. To assure such behavior the reactor has to have sufficient horizontal elongation. Therefore those reactors are often called mixer-settler. The mixing zones can be further constrained by installing baffles [8].

It is extremely important to develop analytical models capable of predicting jetting, bubble formation, the development of bubble plume, the mixing of liquids, i.e. metal and slags, and gas, and heat and mass transfer between the phases. Such information is necessary in the design of modern metallurgical processes from basic principles.

In fundamental research bubble formation at the submerged injector has been studied in detail by many researchers e.g.[19,20]. At higher gas velocities a jet will be produced which breaks up into a bubble plume when sufficient jet momentum is dissipated. Jetting might be necessary to avoid creation of solidifying material at the mouth of the nozzle [21], but extensive jetting particularly in shallow baths can lead to splashing and wave agitation.

222

Several researchers attempt to predict the amount of liquid entrained by the gas jet or bubble plume e.g.[22,23]. A bubble plume with a Gaussian velocity profile is conceptualized in which liquid is entrained in the lower part of the plume and shed close to the surface [24,25]. Numerical analysis of stirring of a single liquid due to gas injection was performed already very early [26-28].

Submerged gas injection into layers of two immiscible liquids has apparently been studied by only a few investigators and all of them assume such low concentration of bubbles that individual bubbles can be considered. A simple model to describe the transport of the heavier liquid with gas bubbles into the lighter liquid was developed by [29]; it was concluded that when the density of the heavier liquid is more than three times the lighter liquid no heavy liquid transport takes place across the interface. In contrast, it was observed by [30] that even in a mercury-water bath a thin film of mercury is dragged up into the water layer. If the upper liquid has a higher viscosity it was noted that the film was drained smoothly but large globules of mercury were drawn up in the wake of the bubble. More detailed studies of the bubble wake behavior are discussed in [31]. The transport of heavier liquid into the lighter liquid and subsequent shedding and settling in a turbulent bubble plume is not well understood.

EXPERIMENTS

The goal of the experiments is to try to make observations and take sufficient data to aid in the development of a numerical analysis.

The test facility constructed for this work is a 1.2 m high, 2.4 m long, variable depth Plexiglas test section to simulate a channel reactor, see Figure 2. A removable plate was installed in the middle of the bottom section, in which different injectors could be installed. The compressed air supply allows flow velocities at the nozzle exit up to sound velocity. The liquids chosen to represent the two immiscible liquids are salt water and soybean oil. Their density ratio and viscosity ratio is in the correct order of magnitude for some metallurgical applications; other liquids were considered but discarded because of environmental or toxic reasons.
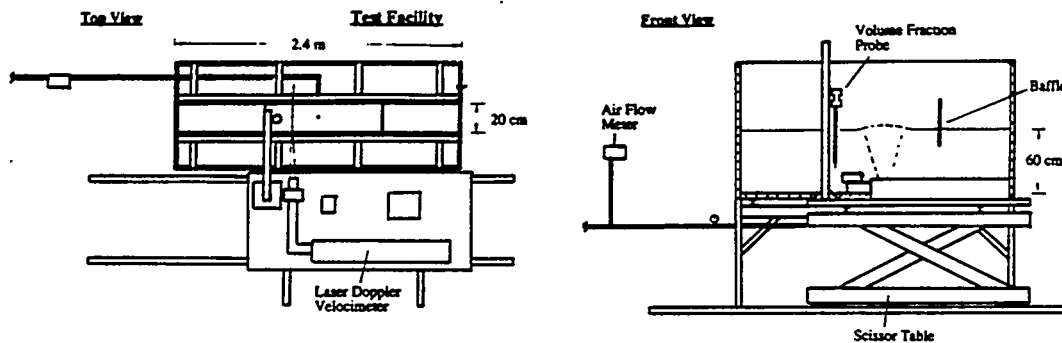

Figure 2: Test Facility

A powerful 2 Watt Laser-Doppler Velocimeter (LDV) is being used to measure liquid velocities throughout the test section with particular emphasis on measuring the liquid velocities in the vicinity of the bubble plume to evaluate bubble plume liquid entrainment and deentrainment. The optics of the LDV can be rotated to allow measurements of both components of the velocity vectors in the central axis of the channel reactor. Experiments were first performed with a single liquid measuring velocities and the effect of baffles on bath circulation. It was found that the total liquid entrainment and the speed of circulation decreased due to the presence of baffles.

First experiments were performed with a channel width of only 2.5 cm. Ideally this could be considered as a thin axial slice through the reactor. But it was quite obvious that wall effects were dominant in this case. Entrainment and plume development could only be considered qualitatively, since the bubbles in the plume were flattened. Nevertheless, the narrow channel permitted an excellent opportunity for visual observation, in particular with two immiscible liquids, which tend to get opaque in the vicinity of the bubble plume. Thus, good three-phase flow behavior observations were possible as well as first quantitative measurements of fluid velocities with the LDV. Figure 3 shows the

223

velocity vectors in the vicinity of the bubble plume and the approximate boundary between the two continuous liquid phases.The circulation can be clearly detected. Figures 3a and 3b differ only in the density ratio of the two liquids. It is clear from these first measurements that the mixing zone gets narrower with an increase in density ratio as one would expect.

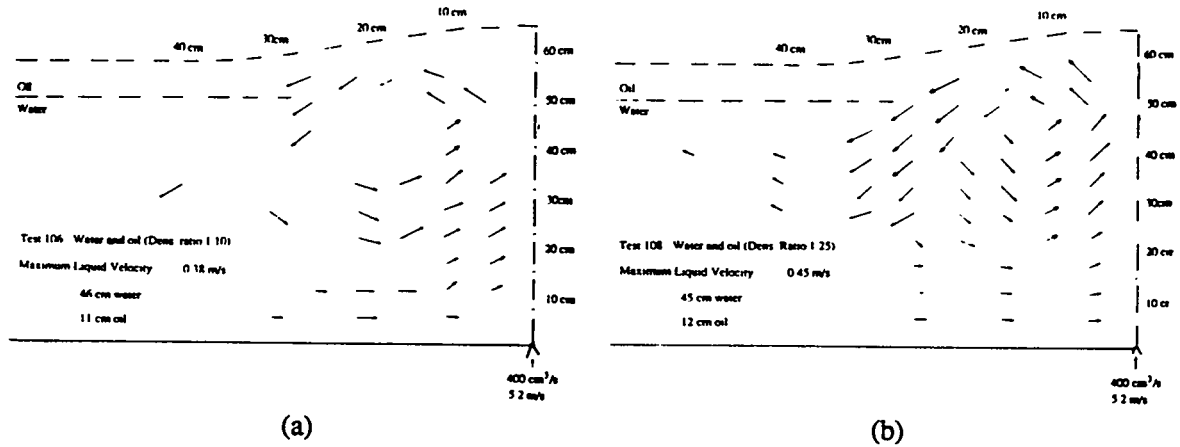(a)   (b)

Figure 3: Liquid Circulation in the Vicinity of the Bubble Plume

In the second round of tests, ongoing now, the channel width was increased to 20 cm, still narrow, but this channel width represents a balance between more realistic three dimensional behavior and the observation difficulties expected in an even wider channel. Already in this channel the mixture becomes partially opaque requiring a specially transparent cone to guide the laser beams to the center plane, where measurements are performed, and to guide the reflected light back to the optics and the receiving photomultiplier.

An electric conductivity probe was developed, similar to the one described by [32] and employed to measure the void fraction in the bubble plume, but an attempt to make the oil sufficiently conductive with an additive failed, since the noise level was too high to discern oil from air.

Finally, an isokinetic sampling probe was developed, which is now in operation. It takes samples in the bubble plume and measures the void fraction of all three phases, gas, heavy and light liquid.

In Figure 4 the void fraction profiles of water and air are shown in and around the bubble plume. The two different graphs are for different gas injection velocities.
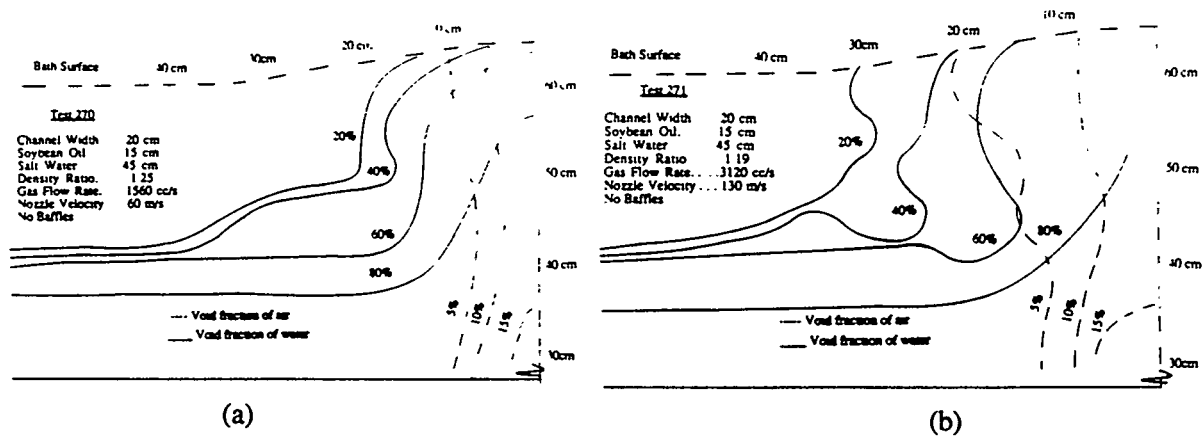

(a)   (b)

Figure 4: Void Fraction of Water and Air in and around the Bubble Plume as a Function of Injection Rates

224

NUMERICAL ANALYSIS AND RESULTS

The goal of the numerical analysis is to predict mixing and settling in elongated reactors with two immiscible liquids stirred by submerged injection.

The computer code FLUENT [33] with some modifications was used to perform the calculations. In the program the bubbles in the plume are tracked as they move through the computational domain. Initial axisymmetric calculations and comparison with predictions and experimental results of others [34,35] showed good agreement.

Since the channel reactor in our experiments is not axisymmetric, three-dimensional (3D) computations were necessary and the result were compared with velocity measurements in the test section. Figure 5 shows this comparison of calculated and measured axial and radial velocity distributions as a function of distance from the plume axis for a specific gas injection rate.
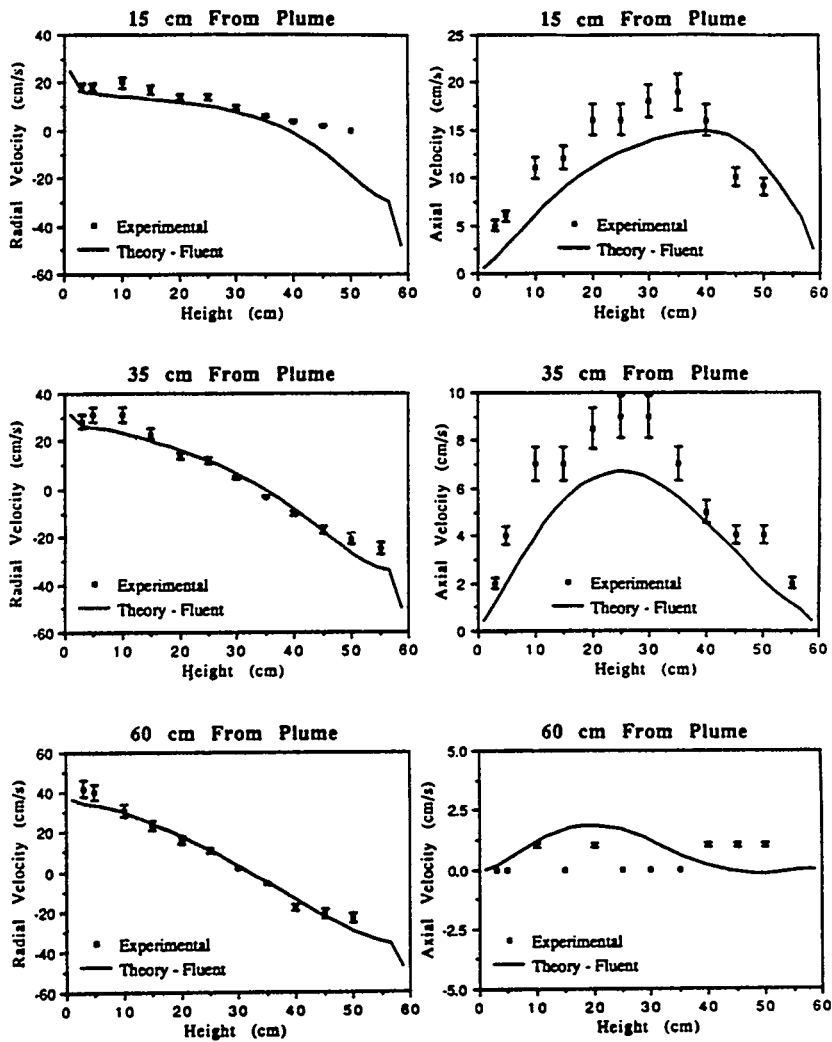

Figure 5: Comparison of Measured and Computed Axial and Radial Velocities in the Test Channel as a Function of Distance from the Plume Axis and Plume Gas Flow Rate

The agreement is good considering the highly turbulent nature of the bubble plume at the high experimental gas flow rates. The flow rates used in the experiments are several times higher than the flow rates previously studied by others [34]. The effect of baffles was also studied and the results

225

were compared to the experimental data. The model was able to predict the velocities and the turbulent energy near the baffles.

Figure 6 shows calculations of the velocity vectors in the channel reactor with baffles in place.

Difficulties arise when there is a highly turbulent bubble plume penetrating two liquid layers of different density and viscosity. Previous models dealt either with only one liquid and a bubble plume or with individual bubbles penetrating the interface between two immiscible liquids.

At the present we are pursuing two different approaches:

Using FLUENT, we are splitting the computational domain into regions of heavy and light liquid. The bubbles in the plume and the dispersed heavy phase are tracked as they were in the single liquid calculations. The bubbles entrain predominantly the heavy liquid and transport it upward into the upper light liquid. As the bubbles rise, the heavy liquid is shed from the bubble's wake and settles back to the heavy phase. Coupling between the two regions is accomplished through the shear stresses and velocities at the interface. Initial results for prediction of behavior in the light phase are shown in Figure 7.

We are also modifying the two phase two-fluid code, K-Fix[36] to include appropriate interphase interaction terms and allow Lagrangian coupling of the air phase in the same way that is currently employed for single liquid calculations.

These two numerical methods haven't been used before for this application mainly because little has been done with three phase liquid-liquid-gas mixtures. The two methods approach the problem from different sides and hopefully much will be learned not only about the behavior of the three phases but also about the applicability of the numerical methods themselves.
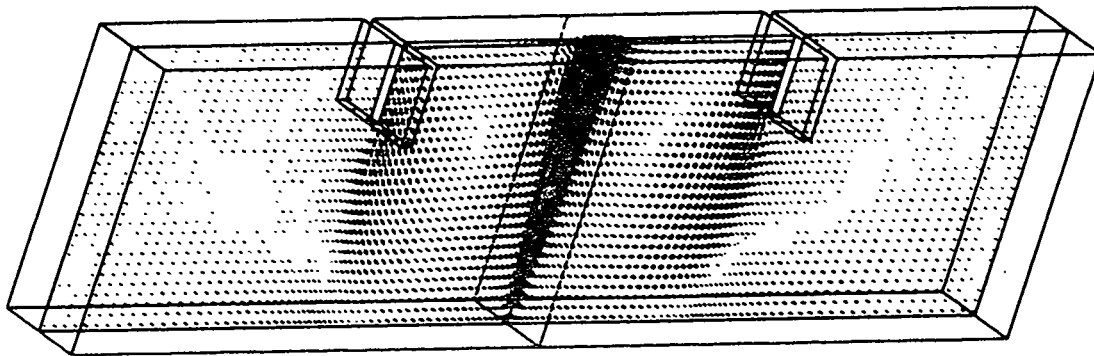

Figure 6: Calculation of the Liquid Velocity in the Test Channel in the Presence of a Baffle
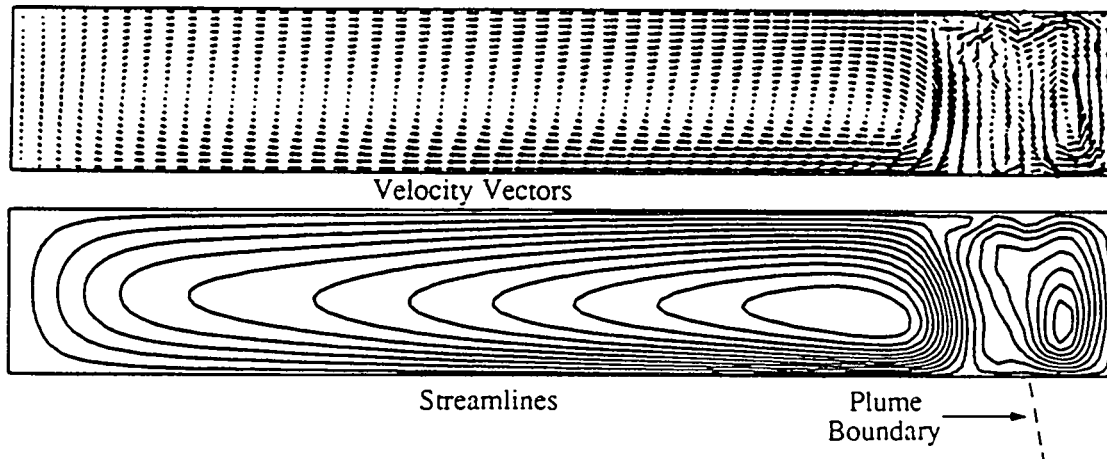

Velocity Vectors

Streamlines   Plume Boundary

Figure 7: Flow Behavior with Two Liquids in Flow Channel

CONCLUSIONS

In the experiments the dependency of entrainment on gas flow rates confirmed previous work [24]. The baffles affect the rate of entrainment in the single liquid plume and effectively decrease the width of the bath recirculation zone. The numerical model has been found to predict the flow behavior in the test channel both with and without baffles. Void fraction distributions for oil-water experiments have been taken for several gas flow rates and illustrate entrainment characteristics of a bubble plume penetrating two immiscible liquid layers. The size of the mixing zone is reduced with increasing density ratio of the two liquids. Research and initial work has been done on models which will allow calculation of behavior in the oil-water bubble plumes. Validation of the final model will be done with comparison to experimental data. Comparisons with actual reactor process can then be accomplished.

REFERENCES

1. R.R. Saddington, W. Curlook and P.E. Queneau, "Use of Tonnage Oxygen" in *Pyrometallurgical Processes in Nonferrous Metallurgy*, J.N. Anderson and P.E. Queneau, eds., pp. V-VI, 261-281, AIME, Gordon & Breach Science Publishers, NY (1967), 261-289.
2. P.E. Queneau, "Oxygen Technology and Conservation," *Metallurgical Transaction*, 3 (1977) 357-369.
3. A. Savard and R. Lee, French Patent, 1,450,718 (July, 1966).
4. W.T. Larkford, Jr., et. al. (ed.) "Oxygen Steelmaking Processes," in *The Making, Shaping and Treatment of Steel*, United States Steel, 10th ed., Iron and Steel Engineering, Pittsburgh, PA (1985) 599-620.
5. K. Brotzmann, "The Bottom-Blown Oxygen Converter - A New Method of Steelmaking," *Technik, Forschung,* 21, (1968) 718-720.
6. P.E. Queneau and R. Schuhmann, Jr., "The Q-S Oxygen Process," *JOM* (August, 1974) Cover and 14 -16.
7. P.E. Queneau and R. Schuhmann, Jr., "Environmentally Clean Lead Bullion Production," *J. of Metals*, 39(2) (1987) 59.
8. P.E. Queneau, "The Coppermaking of Continuous Oxygen Converter Technology, Design and Offspring," The Paul E. Queneau International Symposium, Extractive Metallurgy of Copper, Nickel and Cobalt, Vol. I Fundamental Aspects, Minerals, Metals and Materials Society, 447-471, Denver (1993).
9. H.K. Worner, "Continuous Ferrous and Nonferrous Bath Smelting," Proceedings of the Savard/Lee Int. Symposium on Bath Smelting, 83-101, Montreal (1992).
10. R. Schuhmann, Jr., "Measurements, Interpretation, and Control of Oxygen Activity in Pyrometallurgical Processes," Proceedings of the Reinhardt Schuhmann International Symposium, Colorado Springs, (1986); Publication of the Metallurgical Society, Inc. (1987) 567-581.
11. P.E. Queneau, "The QSL Reactor for Lead and Its Prospects for Cu, Ni and Fe," *JOM*, 41(12) (1989) 30-35.
12. American Metal Market, New York, NY, July 28 (1989) 14.
13. C.R. Schneidesch, H.J. Richter and P.E. Queneau, "Mixing and Settling in QSOP Oxygen Reactor," Proceedings of the Reinhardt Schuhmann International Symposium, Colorado Springs, November (1986); Publication of the Metallurgical Society, Inc., 43-63, (1987).
14. A. Suter and G. Yadigaroglu, "Mixing of the Oxidic and Metallic Phases due to Gas Bubble Transport," Proceedings Committee on the Safety of Nuclear Installation, EPRI, February (1987)

15. G. Gonzalez and M.L. Corradini, "Experimental Study of Pool Entrainment and Mixing Between Two Immiscible Liquids with Gas Injection," Proceedings Committee on the Safety of Nuclear Installation, EPRI, February, (1987).

16. M. Epstein et. al., "Incipient Stratification and Mixing in Aerated Liquid-Liquid or Liquid-Solid Mixtures," *Chem. Eng. Science.*, **36**(4), 784-787, (1981).

17. A.J. Suo-Antilla, "The Mixing of Immiscible Liquid Layers by Gas Bubbling," NUREG/CR-52119, November, (1988).

18. Arthur et. al., "Operating Experience with QSL Submerged Bath Smelting for Production of Lead," Proceedings of the Savard/Lee Int. Symposium on Bath Smelting, Minerals, Metals and Materials Society, 127-145, Montreal, (1992).

19. J.F. Davidson and B.O.A. Schüler, "Bubble Formation at an Orifice in an Inviscid Liquid," *Trans. Inst. Chem. Engrs.*, **38**, 335-342, (1960).

20. J.F. Davidson and B.O.A. Schüler, "Bubble Formation at an Orifice in a Viscous Liquid," *Trans. Inst. Chem. Engrs.*, **38**, 145-154, (1960).

21. G. Savard and R. Lee, "Submerged Oxygen Injection for Pyrometallurgy," Proceedings of the Savard/Lee International Symposium on Bath Smelting, Minerals, Metals and Materials Society, 645-660, Montreal, (1992).

22. T. Abel Engh and M. Nilmani, "Bubbling at High Flow Rates in Inviscid and Viscous Liquids (Slags)," *Metallurgical Trans.*, **19B**, 83-94, (1988).

23. W. Freedman and J.G. Davidson, "Hold-Up and Liquid Circulation in Bubble Columns," *Trans. Inst. Chem. Engrs.*, **47**, T251-T262, (1969).

24. Y. Sahai and R.I.L. Guthrie, "Hydrodynamics of Gas Stirred Melts; Part I: Gas/Liquid Coupling; Part II: Axisymmetric Flows," *MetallurgicalTrans.*, **13B**, 203-211, (1982).

25. J. Szekely and N. El-Naddah, "Turbulence and Agitation in Ladle Metallurgical Operation," I&SM, 22-29, 1984.

26. R.M. Figueira and J. Szekely, "Turbulent Fluid Flow in a Water Model of an AOD System," *Metallurgical Trans.*, **16B**, 67-75, (1985).

27. A. Murthy and J. Szekely, "Some Fundamental Aspects of Mixing in Metallurgical Reaction Systems," *Metallurgical Trans.*, **17B**, 487-490, (1986).

28. D. Mazumdar and R.I.L. Guthrie, "Hydrodynamic Modeling of Some Gas Injection Procedures in Ladle Metallurgy Operations," *Metallurgical Trans.*, **16B**, 83-90, (1985).

29. G.A. Greene, J.C. Chen and M.T. Conlin, "Onset of Entrainment Between Immiscible Liquid Layers Due to Rising Gas Bubbles," *Int. J. Heat Mass Transfer*, **31**, 6, 1309-1317, (1988).

30. D. Poggi, R. Minto and W.A. Davenport, "Mechanisms of Metal Entrapment in Slags," *J. of Metals*, 40-45, November, (1969).

31. L.S. Fan and K. Tsuchiya, "Bubble Wake Dynamics in Liquids and Liquid-Solid Suspensions," Butterworth-Heinemann, Boston, (1990).

32. A.H. Castillejos and J.K. Brimacombe, "Measurement of Physical Characteristics of Bubbles in Gas-Liquid Plumes; Part I: An Improved Electroresistivity Probe Technique; Part II: Local Properties of Turbulent Air-Water Plumes in Vertically Injected Jets," *Metallurgical Trans.*, **18B**, 649-658, 659-671, (1987).

33. FLUENT, 4.11, Computer program to model fluid flow. Distributed and developed by Fluent Inc., Hanover, NH, (1992).

34. M.R. Davidson, "Numerical Calculations of Two-Phase Flow in a Liquid Bath with Bottom Gas Injection: The Central Plume," *Applied Mathematical Modeling*, **14**, 67-76, (1990).

35. S.T. Johansen and F. Boysan, "Fluid Dynamics in Bubble Stirred Ladles: Part II Mathematical Modeling," *Metallurgical Transactions B*, **19B**, 755-764, (1988).

36. W.C. Rivard and M.D. Torrey, "K-FIX: A Computer Program for Transient, Two-Dimensional, Two-Fluid Flow," LA-NUREG Rept. No. 6623, Los Alamos Scientific Lab. (1978).